Deciphering the Molecular Mechanisms Underlying Cochlea Development in Mice using Next-Generation Sequencing Technologies and Comprehensive Computational Approaches

by

Shuze Wang

A dissertation submitted in partial fulfillment
of the requirements for the degree of
Doctor of Philosophy
(Bioinformatics)
in the University of Michigan
2023

Doctoral Committee:

Assistant Professor Jie Liu, Co-Chair
Assistant Professor Joerg Waldhaus, Co-Chair
Associate Professor R. Keith Duncan
Assistant Professor Jeffrey Regier
Assistant Professor Joshua Welch

Shuze Wang

shuzwang@umich.edu

ORCID iD: 0000-0003-1157-1311

Dedication

To my husband and my parents

Acknowledgements

I have been incredibly fortunate to spend the last five years surrounded by knowledgeable, enthusiastic, and caring individuals. First and foremost, I would like to express my sincere gratitude and appreciation to my advisors, Dr. Joerg Waldhaus and Dr. Jie Liu, who have supported me throughout my dissertation journey. Their guidance, expertise, and unwavering commitment to my success have been invaluable. I am grateful for the time and effort they have dedicated to me, and for their patience and understanding during the challenging moments. Their mentorship has not only enhanced my research skills, but also has inspired me to become a better scholar. I am also greatly appreciative of the support and guidance of my dissertation committee members, Dr. Joshua Welch, Dr. R. Keith Duncan, and Dr. Jeffrey Regier. Their guidance and feedback have been crucial in shaping my research.

I am deeply grateful to my collaborators, Dr. Donna Martin, Dr. Jianping Fu, Dr. Yiwen Zhai, Dr. Xufeng Xue, and Dr. Christopher M. Welch, who have been an integral part of my scientific research. I collaborated on numerous experiments with Dr. Saikat Chakraborty, Dr. Mary Lee, Jack Ruhala, and Scott Jones, who took great pains to produce excellent work. Though I did not do much work with them directly, Linghua Jiang, Fan Feng, Yuanhao Huang, Zhenhao Zhang, Zheyu Zhang, and Sean Moran were supportive lab mates as well.

I would also like to thank the DCMB staff, most notably Julia Eussen and Kati Ellis, who contribute substantially to daily student life in the Ph.D. program. Prof. Margit Burmeister and Prof. Maureen Sartor, the co-directors of the Bioinformatics Ph.D. program, have both been a

great help to me. Throughout the program, they have gone out of their way to make students feel supported in the department.

I would like to express my heartfelt gratitude to my beloved friends who have supported me throughout my dissertation journey. Their encouragement and moral support have been a constant source of inspiration and motivation. I am grateful for the unforgettable memories we have shared during this journey. Their presence has made this challenging journey much easier, and I could not have done it without them.

Finally, and perhaps most importantly, I am extremely grateful to my amazingly supportive family. I thank my parents, Yuefen Wang and Yangang Wang, for their boundless love and unconditional support. Both of my parents show a strong interest in my single-cell work, although they are conducting research in traditional Chinese medicine. I owe special thanks to my beloved husband, Yaohui Guo, for good and tough times we have been through together. It is impossible for me to fulfill this journey without his encouragement and accompany. I am looking forward to continuing the next phase of our journey together.

Table of Contents

List of Tables

List of Figures

Abstract

Hearing is mediated by the specialized sensory epithelium known as the organ of Corti, which is located in the cochlea of the inner ear. One hallmark of the cochlea is the ability to discriminate between different sound frequencies. This characteristic is based on the tonotopic organization of the organ of Corti, where different frequencies are detected by the sensory cells depending on their position along the longitudinal axis.

In this thesis, we first applied single-cell RNA-sequencing (scRNA-seq) from two distinct time points to investigate the molecular mechanisms of tonotopic patterning during embryonic development using a computational framework. We proposed two biological hypotheses regarding the tonotopic patterning during cochlear duct extension and tested the hypotheses by leveraging the scRNA-seq datasets. Our findings suggested that spatial identity in the developing cochlea was conferred by morphogens rather than a cell division-associated mechanism. Subsequently, the 3D anatomical structure of the developing cochlea was reconstructed from scRNA-seq data to identify morphogens mediating longitudinal patterning. Opposing gradients of the retinoic acid (RA) and sonic hedgehog (SHH) were found along the tonotopic axis during development. Functional interrogation using mouse cochlear explants supported the notion that both RA and SHH jointly function to specify the tonotopic axis.

Next, we provided a comprehensive computational pipeline to identify the regulatory landscape controlling the differentiation of the organ of Corti. By utilizing single-cell assay for transposase accessible chromatin using sequencing (scATAC-seq) and scRNA-seq techniques

from genetically labeled mouse hair cells and supporting cells after birth, we predicted cell type-specific functions of developmental transcription factors and reconstruct gene regulatory networks. Comparative analysis determined 20 hair cell-specific activators and repressors, along with their downstream target genes. Clustering of target genes revealed related transcription factors and inferred their developmental functions. Furthermore, spatial reconstruction of transcriptional and chromatin accessibility trajectories suggested that the formation of the cell type specific chromatin accessibility landscape is lagging behind their transcriptional identity.

Lastly, we employed our computational pipeline in conjunction with laboratory experiments to identify RA regulated genes in organ of Corti development. RA signaling in the cochlea is mediated via binding of the ligand to the RARA receptor that functions as transcription factor. Using computational approaches, we explored the role of RARA in cochlear hair cell differentiation. Among the genes that are regulated by RARA, we found *Lfng*, a known supporting cell marker. Analyzing scRNA-seq and scATAC-seq data, we found that in absence of RA the function of RARA is to repress the expression of supporting cell specific genes in postnatal hair cells. Interestingly, ectopic RA was found to induce the expression of *Lfng*, suggesting that binding of RA renders RARA into a transcriptional activator, which likely is the case during embryonic development of the cochlea.

Chapter 1 Introduction

1.1 Hearing and hearing loss

Hearing loss is a significant public health concern that affects individuals across the lifespan (World Health Organization 2021, Organization 2021, Chadha, Kamenov and Cieza 2021). According to the World Health Organization (WHO), it is estimated that over 430 million individuals worldwide had disabling hearing loss in 2020, with a projected increase to over 700 million by 2050 (World Health Organization 2021, Chadha et al. 2021). The prevalence of hearing loss increases with age, with an estimated 1 in 4 individuals aged 65-74 experiencing hearing loss, rising to 1 in 2 individuals aged 75 and older. Additionally, exposure to loud noise is a leading cause of hearing loss in younger individuals, with approximately 1.1 billion individuals aged 12-35 years at risk (Chadha, Cieza and Reyes 2018, World Health Organization 2021). The negative impact of hearing loss extends beyond communication difficulties, as it can also lead to social isolation, reduced job opportunities, and increased healthcare costs. The WHO highlights the importance of prevention, early identification, and timely interventions to address this growing burden (World Health Organization 2021).

Hearing is a complex process that involves the detection, transmission, and interpretation of sound waves by the auditory system (Moore 2012, Plack 2018). The process begins with the outer ear, which collects sound waves and directs them into the ear canal towards the eardrum (Moore 2012). The eardrum vibrates in response to the sound waves, which causes three tiny bones in the middle ear (the malleus, incus, and stapes) to vibrate and transmit the sound to the

inner ear (Plack 2018). In the inner ear, the sound waves are transformed into electrical signals by hair cells in the cochlea, which are specialized sensory cells that detect sound. These electrical signals are then transmitted to the brain via the auditory nerve, where they are interpreted as sound (Plack 2018, Moore 2012).

The auditory system is a complex sensory pathway that enables the detection and interpretation of sound stimuli (Basch et al. 2016a). Central to this process is the sensory epithelium, known as the organ of Corti, located within the cochlea of the inner ear (Wilkerson et al. 2019b). The organ of Corti is a highly specialized structure that comprises a precise arrangement of hair cells and supporting cells. During inner ear development, the formation of this precise cellular pattern is crucial for proper hearing function (Basch et al. 2016a). Specifically, the number and placement of hair cells and supporting cells are meticulously determined through accurate proliferation and differentiation of sensory progenitors. Within the cochlea duct, three rows of outer hair cells and one row of inner hair cells are arranged in a unique pattern that enables the detection and amplification of sound waves (Basch et al. 2016a). Each hair cell is surrounded by specific types of supporting cells that play critical roles in maintaining the function and survival of hair cells (Basch et al. 2016a). Understanding the intricate cellular organization and developmental processes of the organ of Corti provides insight into the complex mechanisms underlying the auditory system with the potential for hearing regeneration.

Hearing loss can be caused by a variety of factors, including genetic predisposition, environmental factors, and certain medical conditions or injuries (Cunningham and Tucci 2017, Ferguson et al. 2017). Some individuals may be born with hearing loss due to a genetic mutation that affects the development of the inner ear (Kwan, White and Segil 2009). Exposure to loud

noises over an extended period of time can also cause hearing loss, as can sudden exposure to extremely loud noises, such as explosions or gunshots. Certain medical conditions, such as infections, tumors, and autoimmune disorders, can also affect hearing, as can head injuries or damage to the ear itself (Rossini et al. 2017). Aging is another common cause of hearing loss, as the inner ear can deteriorate over time (Liu and Yan 2007). Finally, certain medications, such as some antibiotics and chemotherapy drugs, can also cause hearing loss as a side effect (Schacht, Talaska and Rybak 2012, Mukherjea et al. 2011, Yorgason, Fayad and Kalinec 2006).

Hearing regeneration is a natural phenomenon observed in some vertebrate species (Groves 2010, Stone and Rubel 2000). In organisms such as fish and birds, auditory hair cells, which are responsible for converting sound vibrations into electrical signals, are regenerated to replace damaged or lost cells (Stone and Rubel 2000). In contrast, the auditory epithelium of mammals in general or humans specifically do not have the same regenerative capacity (Groves 2010). Once damaged or destroyed, hair cells cannot be replaced, leading to permanent hearing loss. While research is ongoing to understand the factors that prevent hair cell regeneration in humans, including possible genetic and environmental factors, the current understanding suggests that the lack of regeneration is due to a combination of intrinsic limitations of the human inner ear and extrinsic factors in the environment (Menendez et al. 2020a). Understanding the intricate cellular organization and developmental processes of the organ of Corti provides insight into the complex mechanisms underlying the auditory system with the potential to inform future strategies of hearing regeneration.

1.2 Molecular basis of tonotopic patterning

Tonotopy in the organ of Corti (OC) refers to the spatial arrangement of hair cells in the cochlea (Talavage et al. 2004). The organ of Corti is tonotopically organized along its

longitudinal axis, such that different hair cells are sensitive to specific frequencies of sound. This arrangement allows for the perception of pitch, with low-frequency sounds detected by hair cells at the apex of the cochlea and high-frequency sounds detected by hair cells at the base (Son et al. 2015c). The tonotopic patterning is established during development through a complex interplay of signaling pathways and gene expression programs. Understanding the molecular mechanisms underlying tonotopic patterning is essential for the development of therapies for hearing loss and other auditory disorders.

To form such a precise tonotopic pattern, accurate proliferation and differentiation of sensory progenitors is necessary. A prosensory domain of proliferating $Sox2^{+}$ progenitor cells starts to form at the ventral side of the otocyst around embryonic day 11.5 (E11.5) (Basch et al. 2016a). In the next 2-2.5 days, the progenitor cells divide and give rise to the future organ of Corti (Basch et al. 2016a). Molecularly, cyclin-dependent kinase inhibitor 1B (*p27Kip1*), a cell cycle inhibitor indicates cell cycle exit and it is expressed in a gradient extending from apex towards the base (Lee, Liu and Segil 2006a). At E13.5, progenitor cells in the mid-basal part of the cochlear duct start to differentiate into hair cells. In the next 3-4 days, the expression gradient of the transcription factor, *Atoh1*, extends in an opposite gradient from the base to the apex (Son et al. 2012, Driver et al. 2013). Thus, development is mirrored in gene expression gradients that dynamically change along the longitudinal axis of the cochlea. In comparison tonotopic function of the organ of Corti requires formation of stable gene expression gradients over time. These gradients encode ion channels, Ca^{2+} buffering proteins and functional relevant genes in the adult animal and are prerequisite to perceive specific sounds frequencies at specific regions of the cochlea (Mann and Kelley 2011a).

Previous research identified the patterning of the basilar papilla (BP) in birds is conferred by multiple signaling pathways (Thiede et al. 2014, Son et al. 2015c). Changes in frequency-specific characteristics have been observed after modulation of retinoic acid (RA) and Bmp7 signaling (Mann et al. 2014), thus suggesting that both pathways mediate apical identity. Furthermore, sonic hedgehog (SHH) is a morphogen regulating tonotopic gradients in birds and mammals during development of the prosensory domain (Basch et al. 2016a, Son et al. 2015a). SHH, secreted by the developing notochord, floor plate and spiral ganglion neurons, is required for cochlea formation during development (Son et al. 2015b). Since SHH is present during the outgrowth of the cochlea duct (Mann and Kelley 2011c), there is the potential that SHH gradient may prefigure the tonotopic organization of the mature cochlea. Experiments in mice expressing constitutively activated smoothened, a hedgehog (HH) signaling mediator, have suggested that HH signaling plays an important role in conferring apical identity in the mammalian cochlea (Son et al. 2015c). Additionally, RA signaling was identified as a potential candidate pathway governing tonotopic identity in birds. RA is a morphogen generally known to be involved in patterning other embryonic organs such as the hindbrain; tissues such as the limb bud (Cunningham and Duester 2015); and the sensory epithelia of the vestibular end organs (Ono et al. 2020a, Ono et al. 2020b). A role for endogenous RA in the organ of Corti development has been reported based on the ability to respond to exogenously applied RA and phenotypes observed upon blocking RA receptor alpha (Kelley et al. 1993, Raz and Kelley 1999).

1.3 Gene regulation mechanisms of differentiation and maturation of the organ of Corti

Hearing is mediated by a specialized sensory epithelium, the OC, within the cochlea of the inner ear (Wilkerson et al. 2019b). The OC consists of only two major cell types, sensory hair cells (HCs) and supporting cells (SCs), that originate from a shared progenitor (Xu et al. 2017).

The two major cell types can be subdivided phenotypically (Corti 1851) as well as transcriptionally (Burns et al. 2015, Kolla et al. 2020) into inner HCs (IHCs), outer HCs (OHCs), and a number of different SC types including Pillar cells (PCs) and Deiters' cells (DCs).

To establish the delicate function of the OC during development and differentiation, spatiotemporal gene expression is strictly controlled by chromatin accessibility and cell type specific transcription factors, jointly representing the regulatory landscape. Transcription factors (TFs) are proteins that regulate the transcription of genes by binding to a specific DNA sequence (Latchman 1997). These proteins play a crucial role in various biological processes, including cell differentiation and maturation. TFs can either activate or repress gene expression, depending on the specific DNA sequence they bind to and the cellular context (Roeder 1996, Lee and Young 2000). Previous research identified that HCs develop in three overlapping phases after undergoing terminal mitosis. Initially, the regulatory landscape is represented by TFs, like ATOH1, LHX3, and GFI1 (Wallis et al. 2003, Woods, Montcouquiol and Kelley 2004, Hertzano et al. 2007), establishing an early HC fate by delineating HCs from SCs. Later around birth, the developmental bifurcation into IHCs and OHCs is controlled by TFs like INSM1 and IKZF2 (Chessum et al. 2018, Wiwatpanit et al. 2018). In parallel, genes contributing to functions including mechanotransduction and synaptic transmission are up-regulated to complete the developmental progression (Fettiplace 2017).

1.4 Single-cell assays of molecular traits

Single-cell assays of molecular traits have emerged as powerful tools to study cellular heterogeneity and diversity (Saliba et al. 2014, Nawy 2014). These assays enable the simultaneous profiling of thousands of individual cells at single-cell resolution, providing insights into cellular states and functions that are masked by traditional population-based

approaches (Saliba et al. 2014). Single-cell assays of molecular traits can be performed using various techniques, including single-cell RNA sequencing (scRNA-seq) and single-cell epigenomics.

1.4.1 scRNA-seq: profiling the transcriptome on single-cell resolution

RNA sequencing (RNA-seq) is a widely used method to investigate transcriptomes and gene expression levels. Briefly, RNA-seq captures the polyA tails of the mRNA molecules and converts into complementary DNA (cDNA) fragments, which are then sequenced using high-throughput sequencing technologies (Hrdlickova, Toloue and Tian 2017, Nagalakshmi, Waern and Snyder 2010). RNA-seq provides researchers with a comprehensive view of gene expression profiles, including the identification of novel transcripts, alternative splicing events, and differential gene expression patterns (Hrdlickova et al. 2017).

RNA-seq is a powerful tool to study the transcriptome of cells or tissues. Specifically, the RNA from a pool of cells is extracted and sequenced, and the resulting data provides an average gene expression profile of the cells in the sample (Marinov et al. 2014). However, this approach cannot detect cellular heterogeneity, which may be important in understanding biological processes such as development and disease (Marinov et al. 2014). Single-cell RNA-seq (scRNA-seq) technology has emerged as a solution to this limitation by allowing gene expression analysis at the single-cell level (Saliba et al. 2014). It provides a more comprehensive view of cell heterogeneity and can identify rare cell types or subpopulations (Saliba et al. 2014, Islam et al. 2011). In addition, scRNA-seq has the potential to reveal cellular dynamics and transitions during development, differentiation, and disease progression, enabling the reconstruction of cellular trajectories and the identification of key regulatory genes and pathways (Islam et al. 2011, Jovic et al. 2022). The advantages of scRNA-seq make it a powerful tool for advancing

our understanding of cellular function and disease mechanisms at the single-cell level (Jovic et al. 2022).

1.4.2 scATAC-seq: profiling the chromatin accessibility on single-cell resolution

Chromatin accessibility is a crucial aspect of gene regulation that influences the accessibility of DNA to transcription factors, thereby impacting gene expression (Klemm, Shipony and Greenleaf 2019b). The state of chromatin accessibility is dynamic and can be modulated by various cellular processes, including epigenetic modifications and chromatin remodeling (Klemm et al. 2019b). Several genome-wide assays for chromatin accessibility have been developed including ATAC-seq (Assay for Transposase-Accessibility Chromatin using sequencing) (Buenrostro et al. 2015). The ATAC-seq technique utilizes a hyperactive Tn5 transposase that inserts sequencing adapters into regions of accessible chromatin, allowing for the identification of open chromatin regions that are accessible to regulatory proteins (Buenrostro et al. 2015). By providing a detailed map of accessible chromatin regions, ATAC-seq facilitates the identification of key regulatory elements contributing to our understanding of chromatin dynamics and regulatory mechanisms (Li et al. 2019b, Buenrostro et al. 2015).

Biological tissues consist of various cell types, and even seemingly uniform cell lines or isolated cell populations may contain cells in various developmental stages or states (Wobus and Boheler 2005). Standard bulk ATAC-seq suffers from limitations when applied to heterogeneous samples (Armand et al. 2021). Such assay relies on an averaging effect over the constituent cell types or cell states of the input sample, which obscures the underlying heterogeneity (Buenrostro et al. 2015). However, there are many biological contexts in which it is important to maintain and observe cell-cell heterogeneity (Armand et al. 2021). Therefore, the development of single-cell assays, which offer high-resolution readouts on single-cell resolution, has become a

prominent area of research in the past decade (Armand et al. 2021). These assays enable the characterization of chromatin accessibility in heterogeneous samples at single-cell resolution, facilitating a deeper understanding of cellular diversity and gene regulation (Armand et al. 2021, Buenrostro et al. 2015).

The study of chromatin accessibility is essential for gaining insight into the mechanisms that regulate gene expression and the impact of gene regulation on cellular function (Packer and Trapnell 2018). Understanding the relationship between chromatin accessibility and gene expression is particularly important in the context of development, differentiation, and disease.

1.5 Dissertation outline

In this dissertation, I utilize single-cell transcriptome data from multiple time points to understand the molecular mechanisms conferring spatial information during organ of Corti development in mice (Chapter 2) and I develop a computational pipeline to integrate epigenomic and transcriptomic single cell data to investigate the gene regulatory landscape during organ of Corti differentiation (Chapter 3). I also utilize the developed pipeline to further identify the retinoic acid regulated genes in cochlear development (Chapter 4).

In chapter 2 of my thesis, I utilize two scRNA-seq datasets from two distinct time points from the same mouse model to uncover the molecular mechanisms of cochlear duct extension during embryonic stages of mice. In chapter 3, I present a comprehensive computational pipeline that integrates single-cell multi-omics data, including scRNA-seq and scATAC-seq, to decipher the regulatory landscape governing the differentiation and maturation of auditory hair cells at the postnatal stage. In chapter 4, I developed bioinformatics approaches with wet lab experiments to investigate the role of retinoic acid receptor alpha, a retinoic acid receptor, in the differentiation of hair cells in the developing cochlea.

Together, these projects demonstrate the value of epigenomic and transcriptomic data in the investigation of molecular mechanisms of cochlea development, as well as the challenges and limitations of applying epigenomic and transcriptomic data in this context.

Chapter 2 Spatial Transcriptomic Reconstruction of the Mouse Cochlea Suggests Morphogen-based Principles in Apex-to-base Specification

2.1 Abstract

In the mammalian auditory system, frequency discrimination depends on numerous morphological and physiological properties of the organ of Corti that gradually change along the apex-to-base (tonotopic) axis of the organ. For example, the basilar membrane stiffness changes tonotopically, thus affecting the tuning properties of individual hair cells. At the molecular level, those frequency-specific characteristics are mirrored by gene expression gradients; however, the molecular mechanisms controlling tonotopic gene expression in the mouse cochlea remain elusive. Through analyzing scRNA-seq data from E12.5 and E14.5 time points, we predicted that morphogens, rather than a cell division-associated mechanism, confer spatial identity in the extending cochlea. Subsequently, we reconstructed the developing cochlea in 3D space from scRNA-seq data to investigate the molecular pathways mediating positional information. The retinoic acid and hedgehog pathways were found to form opposing apex-to-base gradients, and functional interrogation using mouse cochlear explants suggested that both pathways jointly specify the longitudinal axis during development.

2.2 Introduction

Sound discrimination into individual frequencies is critical for communication and requires a delicate architecture of the auditory organs. In mammals, sensory hair cells (HCs) detect various frequencies according to their position along the elongated tonotopic axis of the

organ of Corti. High frequencies are detected at the base, and low frequencies are detected at the apex (Mann and Kelley 2011b). To resolve the different frequencies, the cochlea forms frequency-specific morphological and physiological characteristics. For instance, the HC size, HC bundle length, and the intracellular calcium buffer concentration change gradually along the longitudinal axis. Together, these and other factors affect parameters such as membrane capacitance, adaptation kinetics, and resting potential, which shape the receptor potential and tuning properties of individual HCs (Davis 2003).

At the molecular level, the morphological and physiological characteristics of the vertebrate cochlea are mirrored by tonotopic gene expression gradients (Son et al. 2012, Frucht et al. 2011), which depend on precise patterning of the auditory organ along the longitudinal axis. In birds, patterning of the basilar papilla (BP) is conferred by multiple signaling pathways (Thiede et al. 2014, Mann et al. 2014, Son et al. 2015c). Changes in frequency-specific characteristics have been observed after modulation of retinoic acid (RA) (Thiede et al. 2014) and Bmp7 (Mann et al. 2014) signaling, thus suggesting that both pathways mediate apical identity. Furthermore, sonic hedgehog (SHH) has been identified to function upstream of Bmp7 and to induce apical gene expression in the chicken BP (Son et al. 2015c). Experiments in mice expressing constitutively activated smoothened, a hedgehog (HH) signaling mediator, have suggested that HH signaling plays a similar role in conferring apical identity in the mammalian cochlea (Son et al. 2015c).

SHH not only plays a role in establishing longitudinal patterning, but also affects the timing of cell cycle exit in prosensory progenitors of the cochlea (Bok et al. 2013). During cochlear duct extension, prosensory cells exit the cell cycle at the cochlear apex first around E12.5, followed by new cells being continually added at the basal end of the organ until division

of the progenitor cells ceases around E14.5 (Löwenheim et al. 1999, Lee, Liu and Segil 2006b). Once the proliferation of prosensory cells is completed, developmental directionality inverts and HCs develop in a base-to-apex gradient (Chen et al. 2002, Cai et al. 2013). In absence of SHH, prosensory progenitors exit the cell cycle prematurely, as indicated by reduced proliferation (Bok et al. 2013). Similarly, genes that function downstream of SHH, such as *Fst*, have been shown to modulate the cell cycle and contribute to longitudinal patterning of the cochlea (Prajapati-DiNubila et al. 2019, Koo et al. 2023). Together, these findings raise the question: 1) whether the primary function of SHH is to modulate the cell cycle exit and the timing of the cell cycle exit plays a critical role in cochlear patterning, as observed in drosophila neuroblasts (Homem and Knoblich 2012), or 2) if SHH acts as a morphogen to mediate positional information, as seen in the developing vertebrate hindbrain (Tufcea and François 2015)? In both cases, developmental patterning of the mammalian cochlea could be explained by a genetic timer that controls a gene regulatory network and thereby induces spatial gene expression gradients along an age (apex-to-base) axis (**Figure *2.1*A**, adopted from (Negrete and Oates 2021)). The gene expression gradients may look identical regardless of whether the genetic timer is triggered by cell division or morphogens. However, we hypothesize that the mode of the genetic timer can be identified by analyzing the gene expression pattern during the time course of cochlear duct extension. Briefly, in a timer with asymmetrical cell division, spatial identity is fundamentally linked to the timing of cell cycle exit. During cell division, the timer of the daughter cell is arrested, while the timer in the dividing progenitor cell continues to run. Thus, the timer is progressively more advanced in each subsequent daughter cell resulting in the formation of gene expression gradients along the longitudinal axis of the organ. Conversely, in a morphogen modulated timer, the morphogen concentration determines the point at which the timer is arrested. This timer is cell cycle

independent, and the morphogen gradient directly translates to the formation of gene expression patterns.

To investigate the function of the genetic timer, we generated single-cell RNA sequencing (scRNA-seq) profiles from the elongating mouse cochlear duct at embryonic day (E) 12.5 and E14.5. Analysis of the spatial gene expression between time points suggested that morphogens, rather than a cell division-associated mechanism, confer spatial identity. Next, to identify novel morphogens involved in patterning the longitudinal axis, we resolved the anatomical origin of each individual cell through a PCA-based approach. A reconstruction of the cochlear duct in 3D space was used to conduct gene set enrichment analysis. RA signaling was predicted to contribute to longitudinal patterning of the organ. The cochlear roof was determined to be a source of the RA signal, whereas signal receiving cells were located in the cochlear floor. Based on the spatial model of the cochlea, a base-to-apex decreasing gradient of RA was predicted *in silico* and confirmed using the *RARE-lacZ* reporter mouse line *in vivo*. Our findings therefore validated that RA and SHH form opposing gradients along the longitudinal axis of the cochlea. Modulation of RA and HH pathways *in vitro* resulted in mirrored phenotypes, thus suggesting that both morphogens form an equilibrium in which SHH patterns the apical identity, and RA patterns the basal identity, of the mouse cochlear duct.

2.3 Results

2.3.1 Predicting the molecular mechanism controlling apex-to-base identity

Longitudinal patterning of the cochlea in mammals has been shown to be modulated by HH signaling (Son et al. 2015c), although molecular mechanisms mediating tonotopic identity remain to be determined. We hypothesize that either a genetic timer with asymmetric cell division or a morphogen-modulated timer mediates positional information during the

development of the cochlea (**Figure *2.1*A**) (Negrete and Oates 2021). According to the model of a genetic timer with asymmetric cell division, the transcriptome of the apical cells at E12.5 and E14.5 should be relatively similar, whereas the basal E12.5 cochlear cells should be most similar to the middle section at E14.5. In this scenario, E14.5 basal cells would not have a matching counterpart in the E12.5 future organ of Corti. In contrast, if the cochlea were patterned by a morphogen-modulated timer, we anticipate that the transcriptional signatures along the apex-to-base axis would dynamically adjust based on the morphogen concentration. Hence, pairs of cells with highest similarities between E12.5 and E14.5 should be located at similar positions with respect to the relative length of the cochlea, regardless of the absolute length of the organ. Our strategy to test both hypotheses was to generate scRNA-seq data for the E12.5 and E14.5 cochlear duct, extract the cochlear floor cells, resolve the anatomical origin of each individual cell, and align both samples to compare the gene expression patterns along the longitudinal axis (**Figure *2.1*B**).

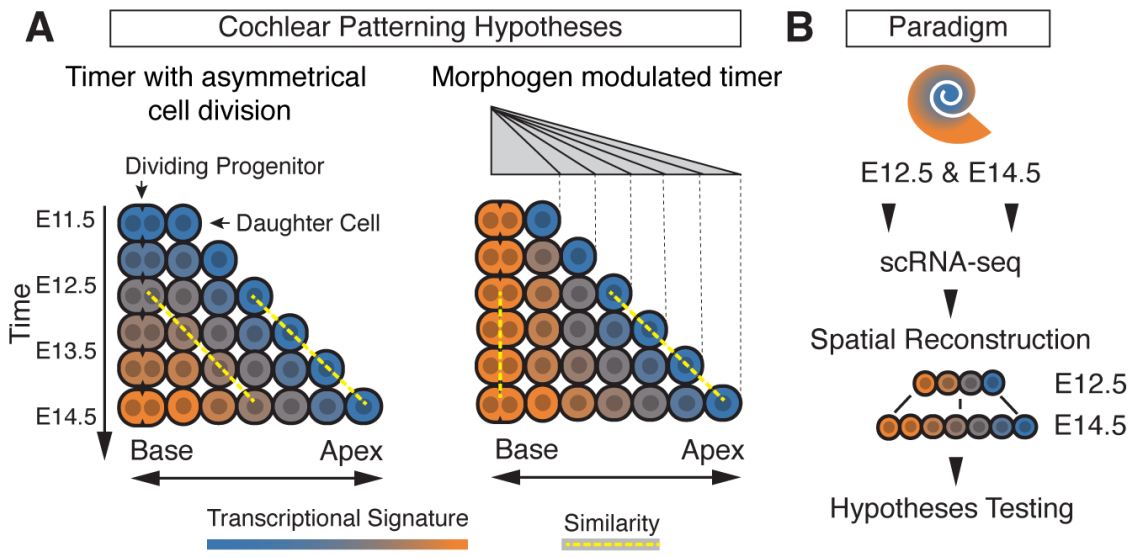

Figure 2.1 Asymmetrical cell division model vs morphogen modulated models. (A) Model of two different genetic timers hypothesized to confer apex-to-base identity in the cochlea. A genetic timer represents a gene regulatory network that changes gene expression dynamics in a sequential manner. Patterning occurs when the timer is arrested in different cells, which can be

triggered by cell cycle exit or morphogen concentration. The arrest results in spatial gene expression signatures, which are represented by different colors for apex (blue) and base (orange). In timers modulated by asymmetrical cell division, the daughter cell's genetic timer is arrested at the time of division, while the timer of the progenitor cell continues to run. In the morphogen model, the timer is controlled by the concentration of the morphogen, which allows for dynamic adjustment of the positional information as the duct extends over time. Dotted yellow lines between the E12.5 and E14.5 cells indicate highest transcriptional similarity. (B) Experimental paradigm to test the hypotheses.

First, we generated scRNA-seq profiles from the developing cochlear duct at E12.5 and E14.5 using the *Sox2*-GFP mouse line (Arnold et al. 2011) to enrich for the target cell population from whole cochlea preparations. As previously reported for E12.5 and E14.5 (Wilkerson et al. 2019a), GFP is expressed in the cochlear floor, giving rise to the prosensory domain, and to a lesser extent in the roof, giving rise to Reissner's membrane and stria vascularis. Cochlear samples were digested to the single-cell level and subjected to fluorescence activated cell sorting (FACS) gating for cells expressing *Sox2*-GFP at detectable levels. Library preparation for scRNA-seq was then performed with the 10x Genomics protocol. Two independent libraries were generated for each time point and sequenced with an average unique count of 17K reads per cell. After stringent quality control, a total of 1,711 cells for both developmental time points were analyzed further. Single cells were clustered with the Seurat v4 (Hao et al. 2021) pipeline for each time point separately (**Figure *2.2***).

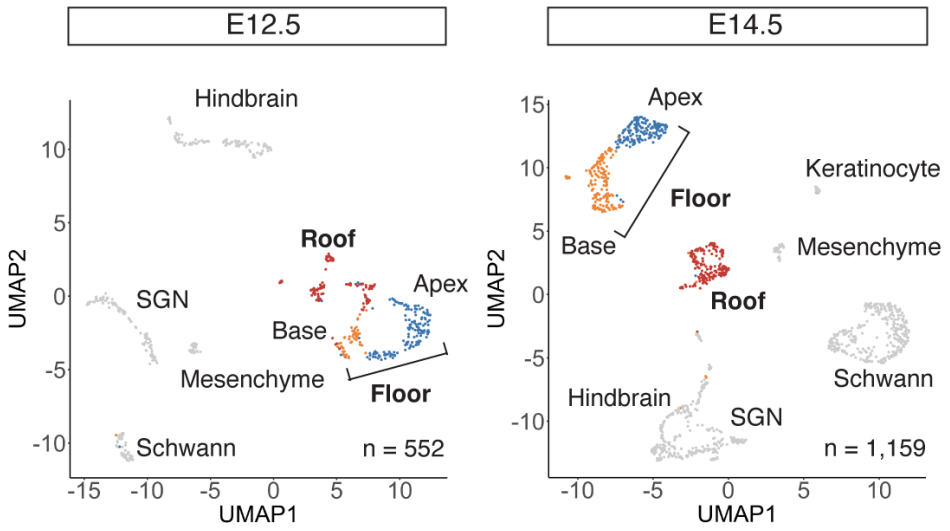

Figure 2.2 UMAP plots of cells isolated at E12.5 and E14.5 with cell type annotation. Cell types constituting the cochlear duct are color coded: roof (red), cochlear floor segregating into apex (blue) and base (orange).

Differentially expressed genes (DEGs) were determined through pairwise comparison for each cluster with the remaining cells of each age group. In total, 2,902 DEGs were identified at E12.5, and 3,279 DEGs were identified at E14.5, with a median number of 268 and 298 DEGs per cluster, respectively. Next, canonical gene markers among DEGs were used for cluster annotation (**Figure *2.3*A**). The cochlear duct segregated into three clusters: the *Oc90*-positive roof (Hartman et al. 2015), the apical floor characterized by *Fst7* expression, and the proliferating basal floor expressing markers including *Mki67* (**Figure *2.2*** and **Figure *2.3*A**) (Yang et al. 2019). Several *Sox2*-GFP-positive off-target populations were identified and excluded from further analysis. To validate the accuracy of the cell type identification, we integrated E12.5 and E14.5 datasets for joint alignment analysis with LIGER (**Figure *2.3*B**) (Welch et al. 2019), which supported the initial annotation.

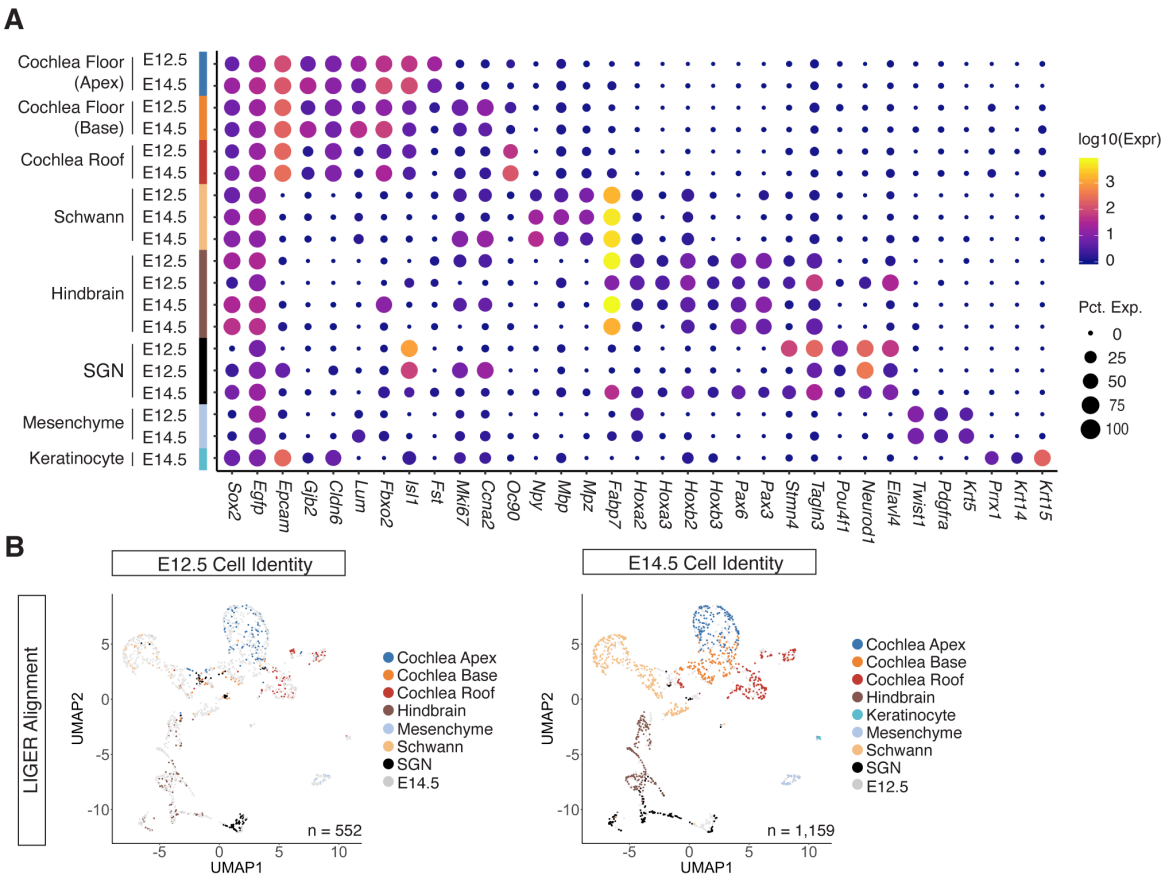

Figure 2.3 Cell type annotation and validation. (A) Dot plot of candidate gene expression levels for each scRNA-seq cluster for both E12.5 and E14.5 time points. The dot size represents the percentage of cells expressing a given transcript for the clusters. Gene expression levels are color coded from purple (low) to yellow (high). (B) UMAP plot of LIGER alignment, color coded by cell identity to visualize overlap of similar cell types isolated from different developmental time points.

Next, we extracted the cochlear floor cells and resolved the longitudinal origin for each cell by conducting principal component analysis (PCA) using all genes detected as features. Briefly, we hypothesized that a 1-dimensional PCA would be sufficient to determine the spatial origin of the individual cells, as previously shown for the P2 organ of Corti (Wang et al. 2021, Waldhaus, Durruthy-Durruthy and Heller 2015). To test this hypothesis and to identify the principal component (PC) capturing the highest variability along the apex-to-base axis, we performed a systematic comparison using the first five PCs. The largest distance between the geometric centers, called centroids, for the apex and base clusters was found along PC1, which

we consider as resolving the longitudinal axis. For each individual gene, we used LOWESS regression (William) to determine the relationship between the gene expression level and PC1. To identify features potentially reflecting longitudinal identity, we determined gradually expressed genes (GEGs) along the apex-to-base axis (PC1) by using Kullback-Leibler (KL) divergence (Kullback and Leibler) to compare the simulated theoretical regression line and empirical regression line. Next, we filtered for gene candidates exhibiting gradual expression with identical orientation for both time points (**Figure *2.4*A**). Shared decreasing expression from the apex to the base was calculated for 26 genes, whereas 86 genes had increasing gene expression from the apex to the base at E12.5 and E14.5 (**Table *2.1***). *Hmga2* and *Hmgb2* were among the GEGs identified with opposing gene expression gradients (**Figure *2.4*B**) and validated by RNA fluorescence *in situ* hybridization (FISH) at E14.5 (**Figure *2.4*C**).

	Gene Symbol
Highly Expressed in Apex	*Igfbp5, Gata3, Rprm, Hey1, Car13, Dclk1, Id3, Hs3st1, Uchl1, Nr2f2, Aqp11, Ypel3, Btg1, Hmga2, Efnb2, Grb10, Skp1a, Sparc, Fst, Isl1, Id2, Pvrl3, App, Atp6v0e, Malat1, Trpm3*
Highly Expressed in Base	*Ptma, Nucks1, Tubb4b, Hat1, 2700094K13Rik, Ckap5, Ccdc34, Dut, Nxt1, Rbm3, Hmgb3, Plk4, Smc4, Cks1b, Anp32e, H2afz, Anp32b, Smc2, Usp1, Magoh, Nasp, Ybx1, Snrnp40, Rpa2, Hmgn2, Stmn1, Dbf4, Tyms, Cenpa, Lyar, Hnrnpd, Rfc5, Ran, Hmgb1, Mest, Lsm5, H1fx, Lsm3, Ube2s, Sae1, Prmt1, Arl6ip1, Mettl9, Hirip3, Dctpp1, Nsmce4a, Bub3, Ppa1, Mif, Tmpo, Pa2g4, Hmgb2, Lsm4, Lsm6, Ddx39, Tkt, H2afx, Ppia, H2afv, Npm1, Pttg1, Hint1, Cbx1, Hn1, Alyref, Tubb2b, Dek, Cks2, Odc1, Erh, Cdca4, H1f0,*

	Tuba1b, Tuba1a, Tuba1c, Ranbp1, Atp5o, Snrpc, Srsf3, U2af1, Lsm2, Ddx39b, Tubb5, Snrpd1, Lmnb1, Rnaseh2c

Table 2.1 List of overlapped gradually expressed genes betweem E12.5 and E14.5 data.

To examine whether the data supported the model of a genetic timer with asymmetric cell division, or the morphogen modulated timer, we leveraged the GEGs and compared the apex-to-base aligned cells for both developmental time points by using Euclidean distance with a radial basis function kernel to determine similarity, as visualized in heatmap format (**Figure *2.4*D**). Initially, metacells were generated to denoise the data by aggregating the ten nearest neighboring cells. Metacells from the E12.5 apex aligned to E14.5 apical metacells, whereas E12.5 basal metacells aligned to E14.5 basal metacells. Given that the cochlear duct is extended through cell division at the basal end, this finding indicated dynamically adjusted gene expression gradients, thus supporting the morphogen modulated timer (**Figure *2.1*A**). To validate the robustness of this finding, we systematically tested various similarity matrix parameters. Together, the findings supported the presence of a morphogen modulated timer in the developing cochlea, rather than providing evidence for the genetic timer with asymmetric cell division hypothesis.

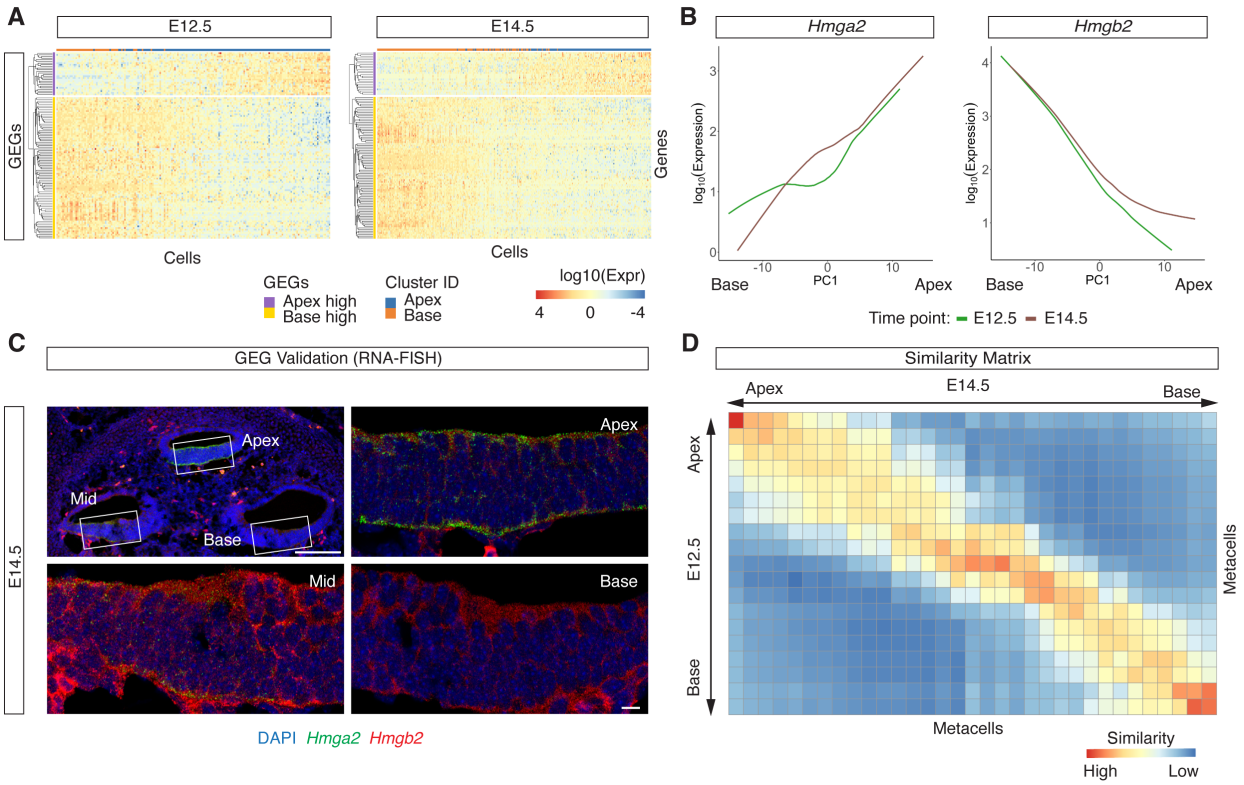

Figure 2.4 Gradually expressed gene identification and hypothesis testing. (A) Heatmap showing the E12.5 expression level of the overlapping GEGs between the E12.5 and E14.5 time points. Columns represent individual cochlear floor cells that are rank ordered along the base-to-apex (*y*-) axis. Rows depict GEGs ordered by hierarchical clustering. Genes highly expressed in the apex are outlined in purple, and genes highly expressed in the base are in yellow. Gene expression levels are color coded from low (blue) to high (red). The heatmap is scaled by rows. (B) Line plots showing the LOWESS regressed expression value of the selected GEGs along the base-to-apex (*x*-) axis, as represented by PC1. *Hmga2* and *Hmgb2* are two GEGs with opposing gradients. The lines are color coded by age: E12.5 (green) and E14.5 (brown). (C) Representative E14.5 histological sections of the cochlea stained for *Hmga2* (green) and *Hmgb2* (red) mRNA with FISH. Upper left: overview. Remaining panels: insets of the cochlear floor at apex, mid, and base locations. A minimum of two samples per probe were analyzed and yielded similar results. (G) Heatmap showing the affinity between E12.5 metacells and E14.5 metacells. Both columns and rows represent metacells ordered along the apex-to-base axis. Color coding indicates similarity from low (blue) to high (red). The heatmap is scaled by rows. Scale bars in (D): 200 μm (overview) and 10 μm (insets).

2.3.2 3D spatial reconstruction of the cochlear duct

The initial analysis used single-cell transcriptional profiles for hypothesis testing regarding the molecular mechanisms mediating apex-to-base identity during cochlear duct extension. Next, we aimed to reconstruct the cochlear duct from single-cell data in 3D space to

allow for digital dissection. Briefly, during development, the cochlear duct differentiates into spatial domains asymmetrically arranged along the duct's circumference (**Figure *2.5*A**). Specifically, the floor and roof segregate into medial and lateral compartments (Kolla et al. 2020), and the prosensory cells develop from the cochlear floor, which includes the zone of non-proliferating cells (Chen and Segil 1999). We hypothesized that the spatial domains of the developing cochlear duct are embedded in a continuum of gene expression, thus enabling reconstruction of the cochlear duct in 3D space. On the basis of this assumption, we reconstructed each cell's relative position along the roof-floor, medial-lateral, and apex-base axes in a PCA-based approach (**Figure *2.5*B-D**). Briefly, cells annotated as apical cochlear floor, basal cochlear floor, and roof cells were extracted. To preserve latent spatial information and identify cellular subgroups, we applied CellTrails (Ellwanger et al. 2018) and identified 9 and 11 CellTrails states for the E12.5 and E14.5 time points, respectively. The CellTrails states for each time point were annotated based on DEGs and reflected the major spatial domains of the cochlear floor and roof (**Figure *2.5*A**). State S9 from E12.5 was comprised of five cells that were identified as HC precursors. Cochlear hair cell precursors have been reported as early as E13.5, while vestibular HC precursors develop earlier (Chen et al. 2002, Cai et al. 2013). To validate that the HC precursors in the E12.5 dataset are of organ of Corti origin, we added an additional quality control step by calculating the otoscore. Briefly, the otoscore was determined for each cell by subtracting the vestibular from the cochlear gene set enrichment score, computed from whole genome expression microarray data (Elkon et al. 2015) using AUCell (Aibar et al. 2017). Cells with positive otoscore were deemed to be of cochlear origin. After validating the otoscore with two reference datasets (Kolla et al. 2020, Wilkerson et al. 2021), we removed 15 cells (E12.5: 1; E14.5: 14) out of a total of 1,711 cells from further analysis.

With respect to the spatial reconstruction, we observed that E12.5 and E14.5 HCs and SCs clustered separately from the cochlear floor, which represents their anatomical origin, instead exhibiting higher similarity with the cochlear roof, as observed in the PCA-based analysis. Therefore, we hypothesized that the unique transcriptomes of HCs and SCs might hinder spatial reconstruction in the PCA-based approach. Both cell types were excluded from the 3D spatial reconstruction, accordingly. However, to provide a cochlear reconstruction including all cell types, we considered HCs and SCs in a separate approach after the framework of the cochlear duct was reconstructed.

For accurate spatial reconstruction of the E12.5 and E14.5 cochlear duct, we applied PCA by using the DEGs between CellTrails states and the original apex, base, and roof clusters for each time point. The results were projected onto a 2D scaled PCA plot (**Figure *2*.5B**), and projection of the original cluster identities allowed for orientation (inset in **Figure *2*.5B-D**). The 3D anatomy of the cochlear duct was reconstructed by projection of the 2D scaled PCA onto a cylindrical surface (**Figure *2*.5C**) with the height of the cylinder representing the longitudinal axis. For better visualization, we generated a circular projection by flattening the apex-base axis (**Figure *2*.5D**).

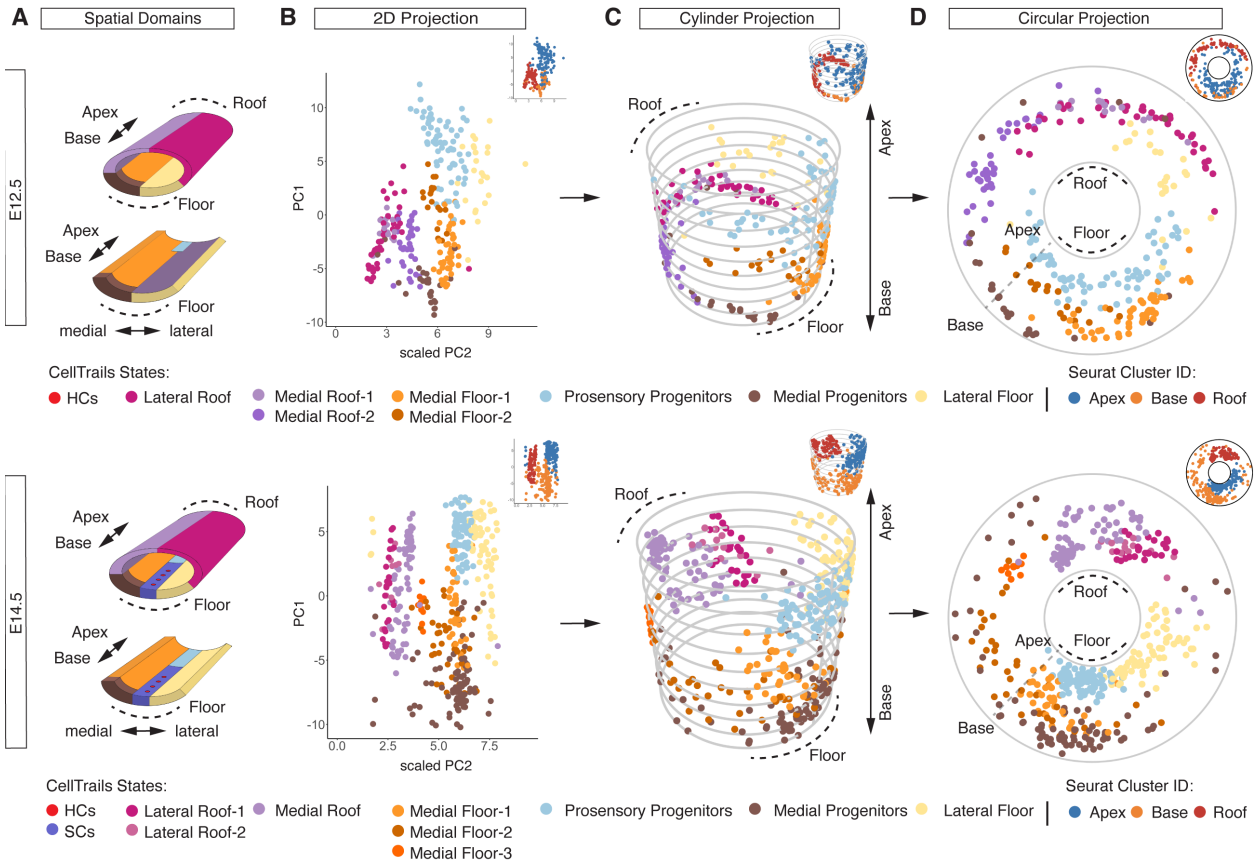

Figure 2.5 2D and 3D spatial reconstruction of the developing cochlear duct. (A-D) Visualizations of the cochlear duct with spatial domains color coded for E12.5 (1st row) and E14.5 (2nd row). (A) 3D schematic representation of spatial domains asymmetrically distributed across the cochlear duct. Shown are 3D representations of the cochlear duct (top) and 3D approximations of the cochlear floor without the roof (bottom). (B) Spatial domains color coded on 2D scaled PCA plots. PC1, corresponding to the longitudinal axis, was projected onto the *y*-axis for intuitive visualization. PC2, scaled by PC3, was projected onto the *x*-axis to distinguish the spatial domains of the cochlear duct. The inset shows the same 2D scaled PCA plot with the original cluster IDs and color code as in Figures 1B, C. (C) Spatial domains visualized with 3D cylinder projection. The height of the cylinder corresponds to the apex-to-base axis of the cochlea with the apex facing up. The inset shows the original cluster IDs and color code projected onto the same cylinder. (D) Spatial domains visualized on 2D circular projections with a flattened apex-to-base axis. The lower half corresponds to the cochlear floor, whereas roof cells form the upper half of the reconstruction. Basal cells are located at the outer perimeter of the projection, and apical cells are located at the center. Medial cells contribute to the left side, whereas lateral cells form the right side. The inset highlights original cluster IDs with original color code.

Next, we spatially validated the 3D reconstruction by comparing projections of differentially expressed marker genes along the roof-floor, medial-lateral, and the apex-base axes

(**Figure *2.6*A-C**) with previously published *in situ* hybridization data deposited in the GenePaint database (Visel, Thaller and Eichele 2004). Briefly, the roof compartment was characterized by *Oc90* expression (Hartman et al. 2015), whereas *Lum* expression (Scheffer et al. 2015) was confirmed for the floor (**Figure *2.6*A**). The medial compartment segregated according to the expression of markers such as *Fgf10* (Pauley et al. 2003), and the lateral compartment expressed markers such as *Bmp4* (**Figure *2.6*B**) (Morsli et al. 1998). In addition, *Fst* expression (Waldhaus et al. 2015) indicated apical identity, whereas cells at the base expressed proliferation markers such as *Mki67* (**Figure *2.6*C**) (Yang et al. 2019). In summary, the 3D reconstruction of the cochlear duct faithfully recapitulated the three major axes of the developing organ.

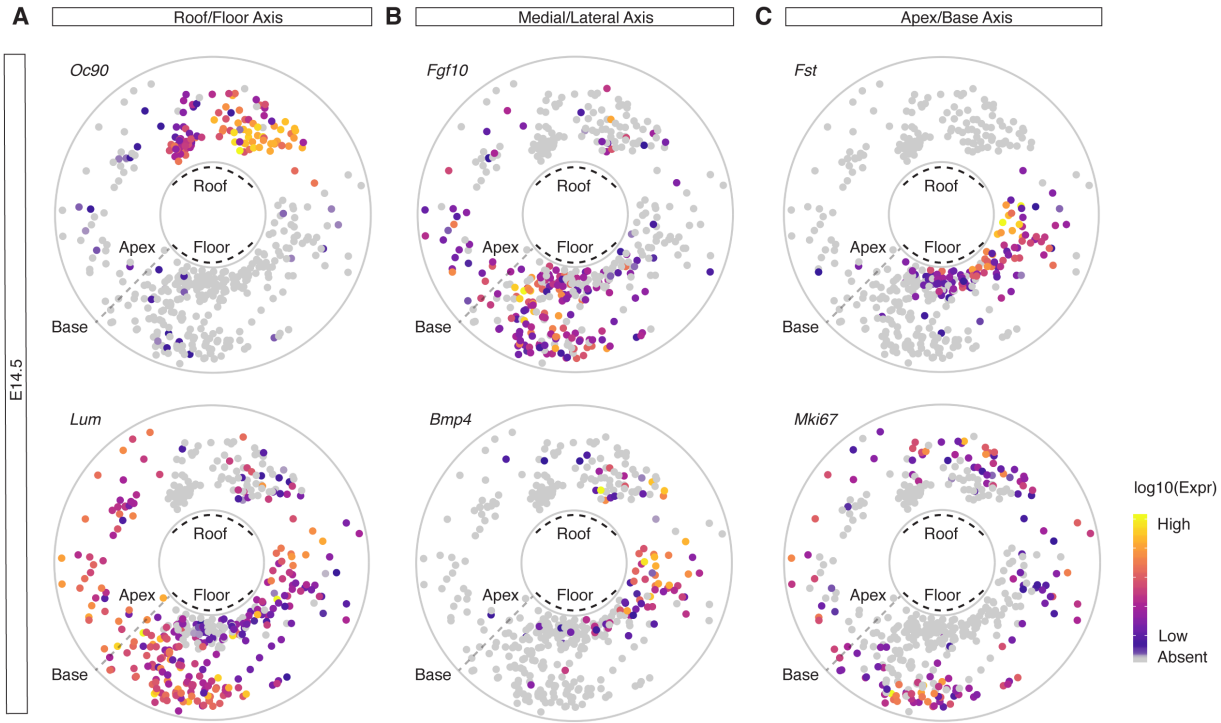

Figure 2.6 Validation of 2D and 3D spatial reconstruction of the developing cochlear duct. (A-C) Three major body axes of the cochlear duct, visualized according to canonical marker gene expression. (A) *Oc90* and *Lum* segregate along the roof-floor axis. (B) *Fgf10* and *Bmp4* expression indicate the medial-lateral axis in the cochlear floor. (C) The apex-base axis is represented by opposing expression of *Fst* and *Mki67*. Gene expression levels are color coded from absent (gray) to low (purple) to high (yellow).

To test whether floor-specific GEGs could be used to reconstruct the longitudinal origin of developing HC and SC precursor, we used the floor GEGs as features and reconstructed all cell types in a 1D PCA. For validation, the *Atoh1* and *Lfng* FISH probe sets were utilized to visualize HC and SC precursors, respectively. At E12.5, small amounts of *Atoh1* transcripts form an irregular pattern in the E12.5 cochlear floor at the apex and base, as detected by FISH, likely indicating the onset of *Atoh1* expression in the cochlea. Analysis of the 1D PCA revealed that *Atoh1*-positive HC precursors were located in the center of the reconstruction. At E14.5, FISH revealed a refined expression pattern, where *Atoh1* highlights a narrow band of nascent HCs in the mid-compartment of the cochlea. Similarly, HC precursors localize to the center of the 1D reconstruction. With respect to *Lfng*, dispersed expression was observed in the cochlea at E12.5, while no distinct SC precursor cluster was apparent in the E12.5 scRNA-seq data. 48 h later, high expression of *Lfng* was found in the mid and base compartments of the future organ of Corti, and highest levels were visualized around the nascent inner HC. Specifically, *Lfng*-positive SC precursors localize to the mid region of the 1D reconstruction. In addition, two GEGs, *Isl1* and *Hmgb2*, were used to visualize longitudinal identity of HC and SC precursor in the 1D reconstruction. In conclusion, the spatial reconstruction of HC and SC precursor was concordant with previous reports of early organ of Corti development (Cai et al. 2013, Wu and Kelley 2012, Cai et al. 2015), thus suggesting that cochlear floor GEGs can be used to approximate the apex-to-base origin of HC and SC precursor from scRNA-seq data.

2.3.3 Spatial reconstruction predicts graded RA signaling along the apex-to-base axis

In analyzing gene expression patterns in the spatially reconstructed cochlear floor, we predicted that morphogens rather than a cell division-associated mechanism were responsible for patterning apex-to-base identity. Although previous research has suggested that SHH signaling

specifies the apical identity in mice (Son et al. 2015c), an inversely oriented morphogen gradient controlling basal identity remained to be determined. Therefore, we used scRNA-seq data to identify longitudinally enriched pathways at single-cell resolution. We used gene sets from the Gene Ontology database (Basch et al. 2016b, Ashburner et al. 2000) and calculated enrichment scores with AUCell (Aibar et al. 2017) for the E12.5 and E14.5 time points. Pairwise comparisons between the apex and base clusters were performed, and differentially enriched GO terms were determined (**Figure *2.7*A**). Overall, 1,646 and 2,659 differentially enriched GO terms were identified for E12.5 and E14.5, respectively. Initially, the GO analysis was validated by confirmation of differential BMP signaling pathway (GO:0030509) enrichment scores at E14.5 between the medial and lateral floor compartments (Consortium 2021). Next, ten RA signaling related GO terms were found to have differential enrichment in the developing cochlea (**Figure *2.7*B**).

Retinoic acid biosynthetic process (GO:0002138) was enriched in the cochlear roof at both time points, thus indicating a source of RA signaling (**Figure *2.7*C**). According to the retinoic acid biosynthetic process GO term, we identified individual genes that were differentially expressed between roof and floor compartments (**Figure *2.7*D-G**). Briefly, RA is a retinol derivative whose availability depends on a two-step enzymatic reaction catalyzed by retinol dehydrogenases (RDHs) and retinaldehyde dehydrogenases (RALDHs). We found that *Rdh10* and *Aldh1a3*, which have been reported to catalyze RA synthesis in the mouse vestibular end organs (Ohyama et al. 2010, Ono et al. 2020a) exhibited differential expression in cochlear roof cells at E14.5 (**Figure *2.7*D-E**). Antibody staining confirmed expression for both enzymes, specifically in the basal roof compartment (**Figure *2.7*F-G**).

Differential enrichment in the cellular response to retinoic acid (GO:0071300) term between apex and base floor compartments indicate presence of RA signal receiving cells in the floor with graded activity along the longitudinal axis (**Figure *2.7*H**). RA regulates the transcription of target genes via binding to nuclear RA receptors that function as transcription factors. Various RA receptors such as *Rara*, *Rxrb*, and *Rxrg* were found to be ubiquitously expressed throughout the cochlear duct at E14.5. Therefore, diffusion of the RA ligand potentially determines its range of activity and requires control. *Cyp26b1*, an RA degrading enzyme (Ohyama et al. 2010), showed a decreasing apex-to-base expression gradient at E14.5 in the center of the cochlear floor (**Figure *2.7*I**). Furthermore, *Dhrs3*, a short-chain dehydrogenase/reductase catalyzing the reduction of the RA precursor all-trans retinaldehyde to retinol (Ono et al. 2020b), showed a similar decreasing apex-to-base gradient at E14.5 (**Figure *2.7*J**), thus implying that an intracellular gradient of bioavailable RA is formed in the opposite direction from the metabolizing enzymes (Feng et al. 2010). To visualize activity of RA in the embryonic and perinatal cochlea, we used a *RARE-lacZ* reporter mouse line (Schilling, Nie and Lander 2012) in which lacZ is under transcriptional control of an RA response element. A base-to-apex decreasing gradient of β-galactosidase was identified, indicating a decrease in RA activity from the base towards the apex of the cochlear duct between E12.5 and P0 (**Figure *2.7*K**). Despite differential expression of RA-synthesizing enzymes along the roof-floor axis, immunological staining of the E14.5 cochlea did not indicate the formation of a β-galactosidase expression gradient between roof and floor. However, a base-to-apex decreasing gradient of β-galactosidase was detected in the cochlear duct, including the prosensory progenitors (**Figure *2.7*L**).

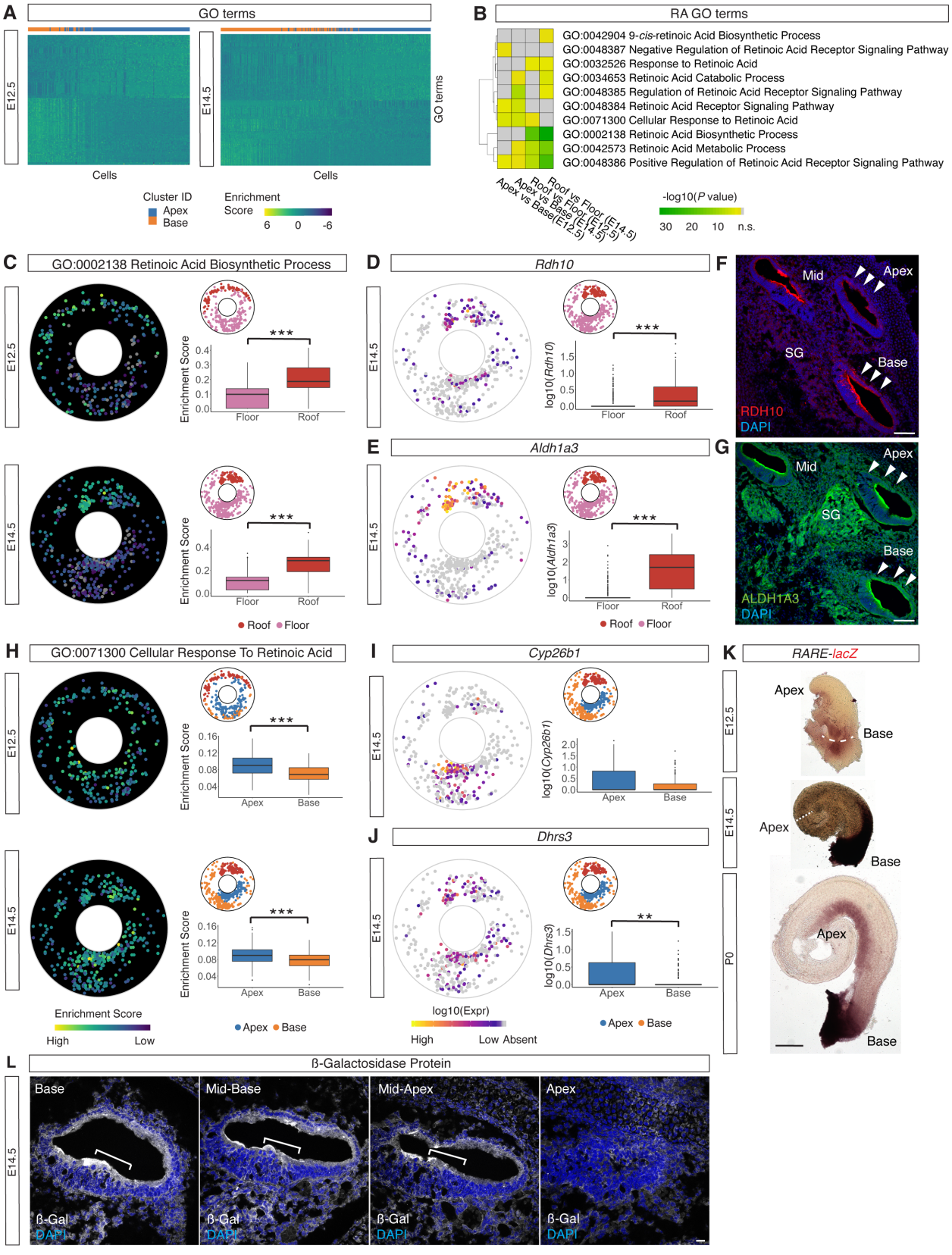
A
GO terms
E12.5
E14.5
GO terms
Cells
Cells
Cluster ID
Apex
Base
Enrichment Score
6 0 -6
B
RA GO terms
GO:0042904 9-cis-retinoic Acid Biosynthetic Process
GO:0048387 Negative Regulation of Retinoic Acid Receptor Signaling Pathway
GO:0032526 Response to Retinoic Acid
GO:0034653 Retinoic Acid Catabolic Process
GO:0048385 Regulation of Retinoic Acid Receptor Signaling Pathway
GO:0048384 Retinoic Acid Receptor Signaling Pathway
GO:0071300 Cellular Response to Retinoic Acid
GO:0002138 Retinoic Acid Biosynthetic Process
GO:0042573 Retinoic Acid Metabolic Process
GO:0048386 Positive Regulation of Retinoic Acid Receptor Signaling Pathway
Apex vs Base(E12.5)
Roof vs Base (E12.5)
Apex vs Base (E14.5)
Roof vs Floor (E14.5)
-log10(P value)
30 20 10 n.s.
C
GO:0002138 Retinoic Acid Biosynthetic Process
E12.5
E14.5
Enrichment Score
Floor
Roof
Roof
Floor
D
Rdh10
log10(Rdh10)
E
Aldh1a3
log10(Aldh1a3)
F
Mid
Apex
SG
Base
RDH10
DAPI
G
ALDH1A3
H
GO:0071300 Cellular Response To Retinoic Acid
High
Low
I
Cyp26b1
log10(Cyp26b1)
J
Dhrs3
log10(Dhrs3)
log10(Expr)
High
Low
Absent
K
RARE-lacZ
P0
L
ß-Galactosidase Protein
Base
Mid-Base
Mid-Apex
Apex
ß-Gal
DAPI

Figure 2.7 RA signaling components in the developing cochlea. (A) Heatmaps showing enrichment scores of the top 100 differentially enriched GO terms for the E12.5 and E14.5 time points. Columns represent single cells ordered along the base-to-apex (*x*-) axis. Rows represent differentially enriched GO terms with ordering based on hierarchical clustering. Significance: adjusted $P < 0.05$ (two-sided Wilcoxon rank-sum test with BH correction). Heatmaps are scaled by rows. (B) Heatmap showing statistical significance for ten RA-associated GO terms. Statistical comparisons include apex versus base, and floor versus roof compartments for the E12.5 and E14.5 time points. High significance, green; low significance, yellow; not significant (n.s.), gray. (C) Retinoic acid biosynthetic process (GO:0002138) GO term enrichment scores projected onto E12.5 (1st row) and E14.5 (2nd row) circular plots. The inset is color coded by floor (pink) and roof (red). The boxplots show significantly different activity scores between the floor and roof compartments for both time points. E12.5: ***P=1.62E-18. E14.5: ***P=9.92E-33 (two-sided Wilcoxon rank-sum test with BH correction). (D-E) mRNA expression levels projected onto E14.5 circular plots. (D) *Rdh10* is differentially expressed in roof cells. ***P=2.58E-12 (two-sided Wilcoxon rank-sum test with Bonferroni correction). (E) *Aldh1a3* is differentially expressed in roof cells. ***P=2.88E-46 (two-sided Wilcoxon rank-sum test with Bonferroni correction). (F-G) Representative E14.5 histological staining of the cochlea and the spiral ganglion (SG) using antibodies raised against (F) RDH10 (red) and (G) ALDH1A3 (green) and counterstained with DAPI (blue). Arrows highlight the roof at both apex and base locations for comparison. A minimum of three sections were analyzed for each antibody, and similar results were obtained. (H) Cellular response to retinoic acid (GO:0071300) GO term projected. The inset is color coded by apex (blue), base (orange), and roof (red). Boxplots show significantly different activity scores between the apical and basal compartments for both time points E12.5: ***P=2.42E-05. E14.5: ***P=7.28E-06 (two-sided Wilcoxon rank-sum test with BH correction). (I) *Cyp26b1* is gradually expressed in a narrow band of cells centered in the prosensory domain extending along the tonotopic axis at E14.5. The difference was not significant when all cells annotated as cochlear floor were considered in the statistical comparison after Bonferroni correction. (J) Significantly higher *Dhrs3* expression in apical cells than basal cells. **P=4.87E-03 (two-sided Wilcoxon rank-sum test with Bonferroni correction). A minimum of three sections was analyzed and yielded similar results. The box plots show the interquartile range (box limits), median (centre line), minimum to maximum values (whiskers). (K) β-galactosidase histochemical staining of E12.5, E14.5, and P0 cochleae. *RARE-lacZ* signal was localized to the basal end of the cochlea. *RARE-lacZ* staining was also found in the spiral ganglion along the entire length of the cochlea, though at lower levels compared to the basal cochlea. Three samples were analyzed and yielded similar results. (L) Representative E14.5 histological sections of the cochlea stained using an anti-β-galactosidase antibody (white) and DAPI (blue). Brackets indicate the nascent organ of Corti. Scale bars in (F, G) 100 μm, in (K) 200 μm, and (L) 10 μm.

Together, these findings suggest that the basal roof is a cellular source of RA in the cochlea. Given the solubility of RA in water (up to 200 nM) (Niederreither et al. 2002), it appears likely that a diffusion gradient at physiological relevant concentrations could be established within the fluid space of the developing cochlear duct, decreasing from the base to

the apex. The *RARE-lacZ* reporter mouse confirmed graded RA signaling activity along the base-to-apex axis and identified prosensory progenitors as RA signal-receiving cells for the paracrine signaling.

2.3.4 Functional RA signal transduction in the developing cochlea

To examine whether the embryonic cochlea is capable of RA signal transduction, we cultured E14.5 cochlear ducts *in vitro*, applied ectopic RA, and monitored changes in *Cyp26b1* expression. *Cyp26b1* is a known RA target gene providing negative feedback in the autoregulation of RA (Ono et al. 2020a). Differential counts for *Cyp26b1* transcripts were determined in a narrow band of cells in the center of the cochlear floor along the apex-to-base axis after 3 h organ culture for the DMSO control with FISH (**Figure *2.8*A-B**). This finding provided additional validation for the 3D reconstruction of the organ, as graded *Cyp26b1* expression was predicted to be restricted to the center of the cochlear floor at E14.5 *in silico* (**Figure *2.7*I**). Next, exposure to 500 nM all-trans-retinoic acid (hereafter RA) for 3 h was sufficient to significantly increase *Cyp26b1* expression comparing the basal compartments of control and experimental explants (**Figure *2.8*A-B**). In conclusion, RA signal transduction was tested to be functional in the E14.5 cochlear floor *in vitro*.

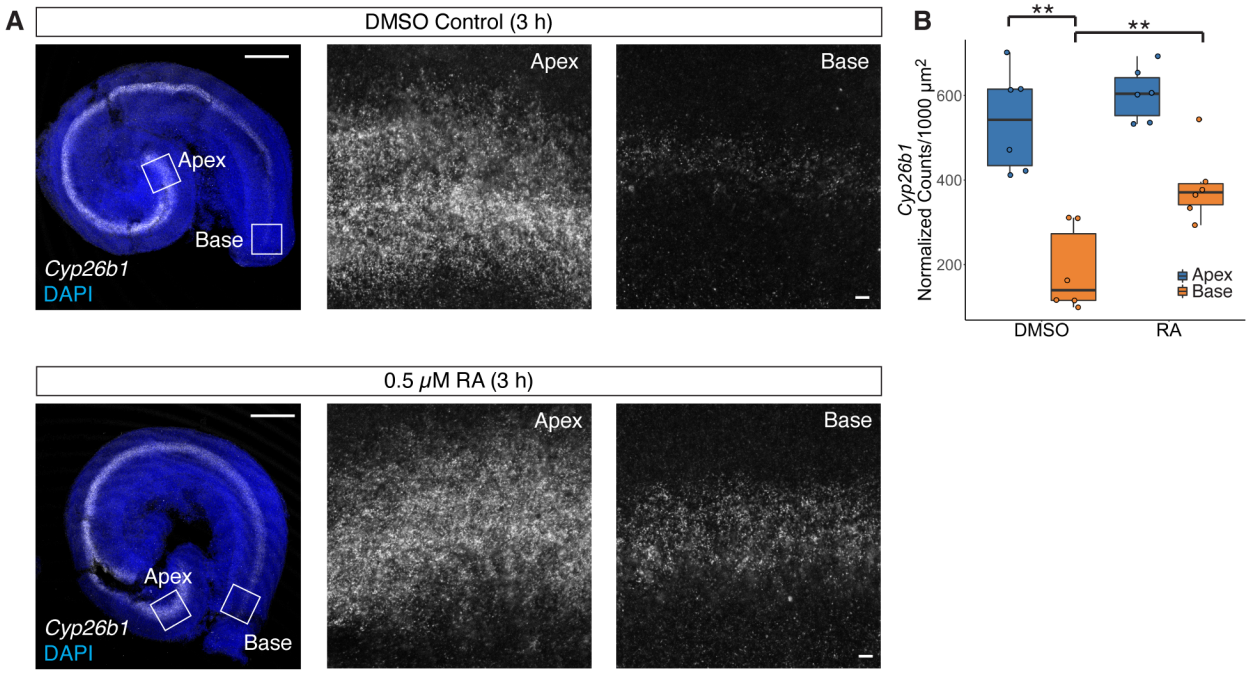

Figure 2.8 RA gradient *in vivo* and functional RA signal transduction in E14.5 cochlear explants. (A) Representative confocal micrographs of E14.5 cochlear explants cultured for 3 h in control medium and medium supplemented with 500 nM ectopic RA. Specimens were stained for *Cyp26b1* mRNA, counterstained with DAPI, imaged in whole mount format, and analyzed in Fiji software (Schindelin et al. 2012). Insets represent higher magnification images that were collected at representative apex and base locations. (B) Quantification of *Cyp26b1* puncta normalized to 1000 μm^2 indicated significantly higher *Cyp26b1* transcript counts for the control apex (n=6) than the control base (n=6). ***P*=2.8E-03 (two-sided paired *t*-test). In addition, *Cyp26b1* expression significantly increased in the basal compartment after exposure to 500 nM RA for 3 h (n=6) compared with the control treatment (n=6). ***P*=4.1E-03 (two-sided unpaired *t*-test). The box plots show the interquartile range (box limits), median (centre line), minimum to maximum values (whiskers), and biologically independent samples (circles). Scale bars in (A), first panels: 200 µm. Scale bar in remaining panels, same for all insets, 10 µm.

2.3.5 Activation of HH signaling enhances Cyp26b1 expression

Because of its catabolic function, CYP26 enzymes play a key role in controlling RA bioavailability during organogenesis of tissues such as the hindbrain (Szuts and Harosi 1991), prefrontal cortex (Maden 2007), and inner ear (Shibata et al. 2021). However, the opposing gradients of *Cyp26b1* (**Figure *2.8*A-B**) and RA (**Figure *2.7*K**) cannot be explained by the autoregulatory capacity of the RA pathway alone. Therefore, identifying additional pathways controlling *Cyp26b1* expression was critical to further address the molecular mechanisms

shaping the RA gradient in the cochlea. On the basis of the tonotopic activity of SHH in the cochlea apex (Son et al. 2015c, Bok et al. 2013) and its potential to exert transcriptional control over CYP26 proteins in limb buds (Bok et al. 2011b), we hypothesized that SHH might function upstream of RA signaling. In support of this hypothesis, we observed graded enrichment scores for SHH- (GO:0060831) and RA- (GO:0002138) GO-terms with opposed orientation along the longitudinal axis of the cochlear floor at E14.5 (**Figure *2.9*A**). In addition, a positive correlation between SHH GO term scores and the expression of *Cyp26b1* was determined. To test whether activation of SHH might be sufficient to increase the expression of *Cyp26b1* in the cochlea, we cultured E14.5 organ of Corti explants and supplemented them with the SHH agonist SAG (1 μM) (**Figure *2.9*B**) (Cunningham and Duester 2015). The culture time was extended to 72 h due to the need for the activation of the HH pathway using SAG, which requires the upregulation of downstream effectors such as the Gli transcription factors. Hence, a delay in the response of the *Cyp26b1* expression was anticipated. The quantification of *Cyp26b1* puncta in the DMSO control revealed a flattening of the gradient after 72 h compared to the 3 h culture paradigm (**Figure *2.8*A** and **Figure *2.9*B**). To test if the flattening of the *Cyp26b1* gradient is due to continued development *in vitro*, we analyzed previously published data from the postnatal day (P)2 organ of Corti (Wang et al. 2021). Robust expression of *Cyp26b1* was evident in the P2 supporting cells, suggesting that factors related to the extended cell culture duration are likely to have caused the flattening of *Cyp26b1* expression in vitro after 72 h. However, supplementation with SAG (1 μM) maintained *Cyp26b1* expression along the entire length of the cochlea at significantly higher levels compared to the control (**Figure *2.9*C**). This finding supported the hypothesis that SHH functions to enhance *Cyp26b1* expression in the cochlea, which suggests that SHH plays a role in shaping the RA gradient.

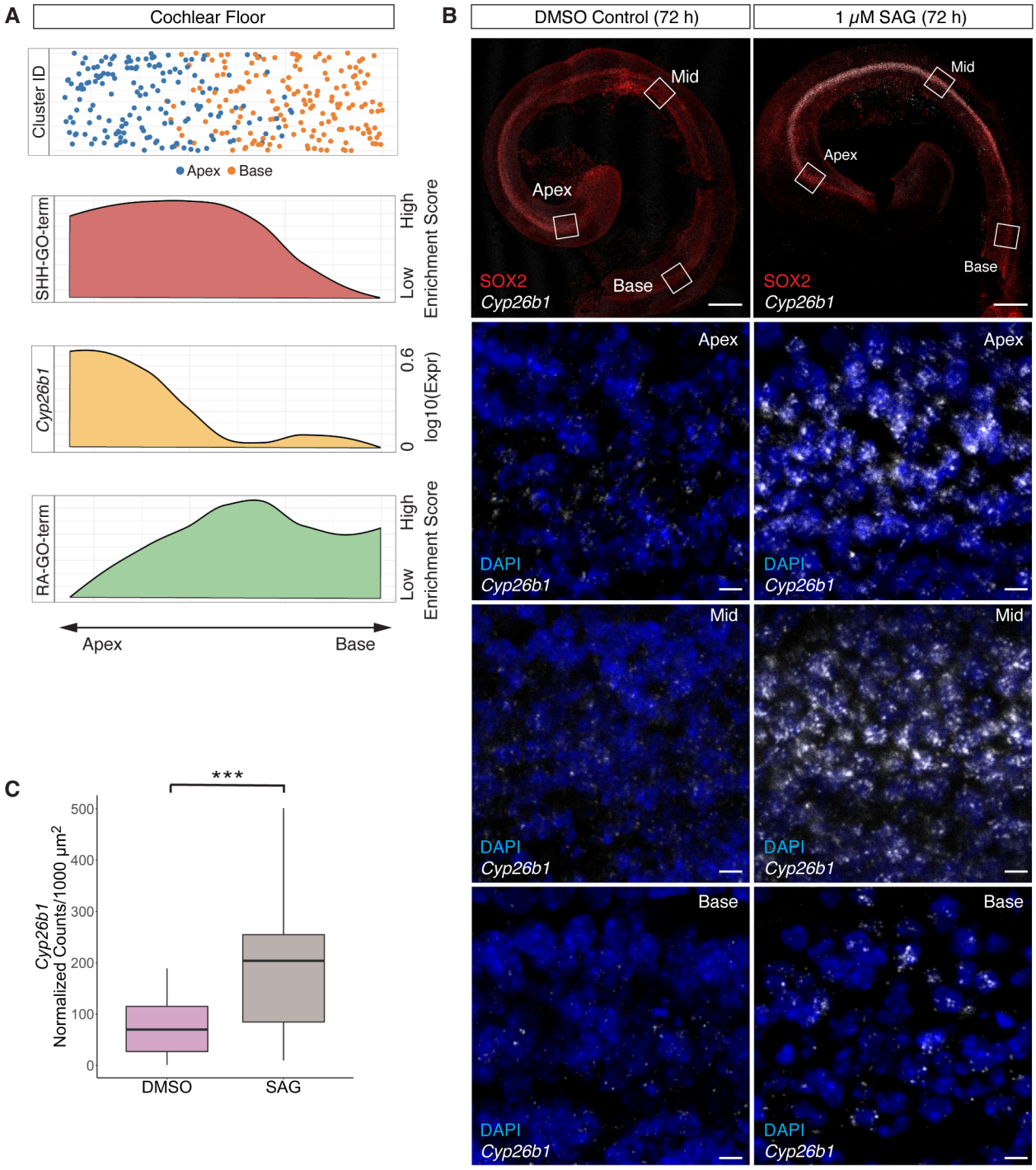

Figure 2.9 SAG enhances *Cyp26b1* expression in E14.5 cochlear explants. (A) PCA-based rank ordering of individual cells of the E14.5 cochlear floor along the apex-to-base (*x*-) axis. Data points are randomly spread along the *y*-axis for better visualization (top panel). Color code: cluster identity apex (blue) and base (orange). Activity scores for the smoothened signaling pathway (GO:0060831) and retinoic acid biosynthetic process (GO:0002138), visualized with LOWESS regression lines, show opposing gradients along the tonotopic (*x*-) axis. In addition, *Cyp26b1* mRNA expression levels show a positive correlation with SHH related GO term

(GO:0060831). (B) Representative micrographs of E14.5 cochlear explants cultured for 72 h in control medium or medium supplemented with the smoothened agonist SAG (1 µM). Explants were stained for *Cyp26b1* transcripts and counterstained with anti-SOX2 antibody and DAPI to enable imaging of the prosensory domain. High resolution images were taken at representative apex, mid, and base locations, and *Cyp26b1* transcripts were quantified in Fiji software. (C) *Cyp26b1* expression levels averaged across the total length of the explant were significantly higher in the SAG group (n=27) than the DMSO control group (n=18). Data are normalized to 1000 μm^2. ***P=1.7E-04 (two-sided unpaired t-test). The box plots show the interquartile range (box limits), median (centre line), minimum to maximum values (whiskers). Scale bars in (B): upper panels, 200 µm; lower panels, same for all insets, 10 µm.

2.3.6 Modulation of RA and HH signaling results in mirrored phenotypes

According to our findings, we hypothesized that RA and SHH form an equilibrium of two opposing morphogen gradients, which control apex-to-base patterning of the cochlear duct. To test this hypothesis, we first identified an apical marker gene from the 3D reconstruction and demonstrated remodeling of its spatial expression upon manipulation of RA and HH signaling in vitro. Briefly, *Hmga2*, a chromatin modifier, was identified as apical reporter based on its classification as GEG at E12.5 and E14.5 (**Figure *2.10*A-B**) and its differential expression along the apex-to-base axis at P0, P2, and P8.3,25 The function of HMGA2 in the cochlea remains to be determined. However, given its stable apex-to-base expression during embryonic development and the postnatal maturation of the organ, we examined the effects of RA and HH signaling pathway modulation on *Hmga2* expression.

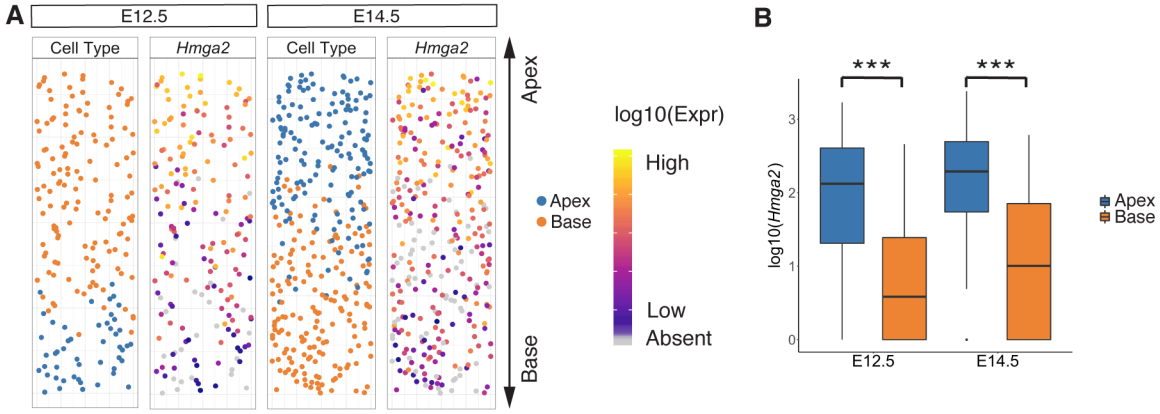

Figure 2.10 Tonotopic expression of *Hmga2* during cochlear duct extension. (A) 1D PCA-based reconstruction of the E12.5 (left) and E14.5 (right) cochlear floor, showing cell identities and *Hmga2* expression levels along the tonotopic axis. The cochlear floor cells are ordered along the base-to-apex (*y*-) axis, with the apex facing up. (B) Statistical analysis of *Hmga2* expression, comparing the apical and basal compartments. For both time points, *Hmga2* expression was significantly higher in apical floor compartments than basal floor compartments. E12.5: ***P=2.17E-05. E14.5: ***P=4.27E-21 (two-sided unpaired Wilcoxon rank sum test with Bonferroni correction). The box plots show the interquartile range (box limits), median (centre line), minimum to maximum values (whiskers).

E14.5 explants were cultured for 72 h, and changes in *Hmga2* expression after pathway modulation were quantified with FISH. To focus the analysis on cell types contributing to the development of the organ of Corti, we co-stained explants with an antibody raised against SOX2, detecting the prosensory domain (Waldhaus et al. 2015). First, differential expression of *Hmga2* along the longitudinal axis was confirmed after 72 h culture in the DMSO control (**Figure *2.11*A, F**). Next, explants were cultured for 72 h and supplemented with 500 nM RA (**Figure *2.11*B, F**), which significantly decreased the *Hmga2* expression in the apical compartment. In contrast, culture with the RA receptor antagonist AGN 193109 (100 nM) (Di Minin et al. 2022) significantly increased *Hmga2* transcript levels at the base (**Figure *2.11*C, F**). Activation of the HH pathway by the smoothened receptor agonist SAG (1 µM) (Cunningham and Duester 2015) significantly increased *Hmga2* expression in the basal compartment after 72 h (**Figure *2.11*D, F**), a phenotype similar to that observed after blocking RA signal transduction. Additionally, supplementation with SANT-1 (10 µM) (Cunningham and Duester 2015), an antagonist that directly inhibits the HH pathway by binding smoothened, significantly decreased *Hmga2* expression to levels comparable to those after application of ectopic RA (**Figure *2.11*E, F**). In summary, the occurrence of mirrored phenotypes strongly suggested that RA and SHH jointly pattern the longitudinal identity of the developing cochlea, whereby RA patterns the base, and SHH patterns the apex of the organ (**Figure *2.11*G**).

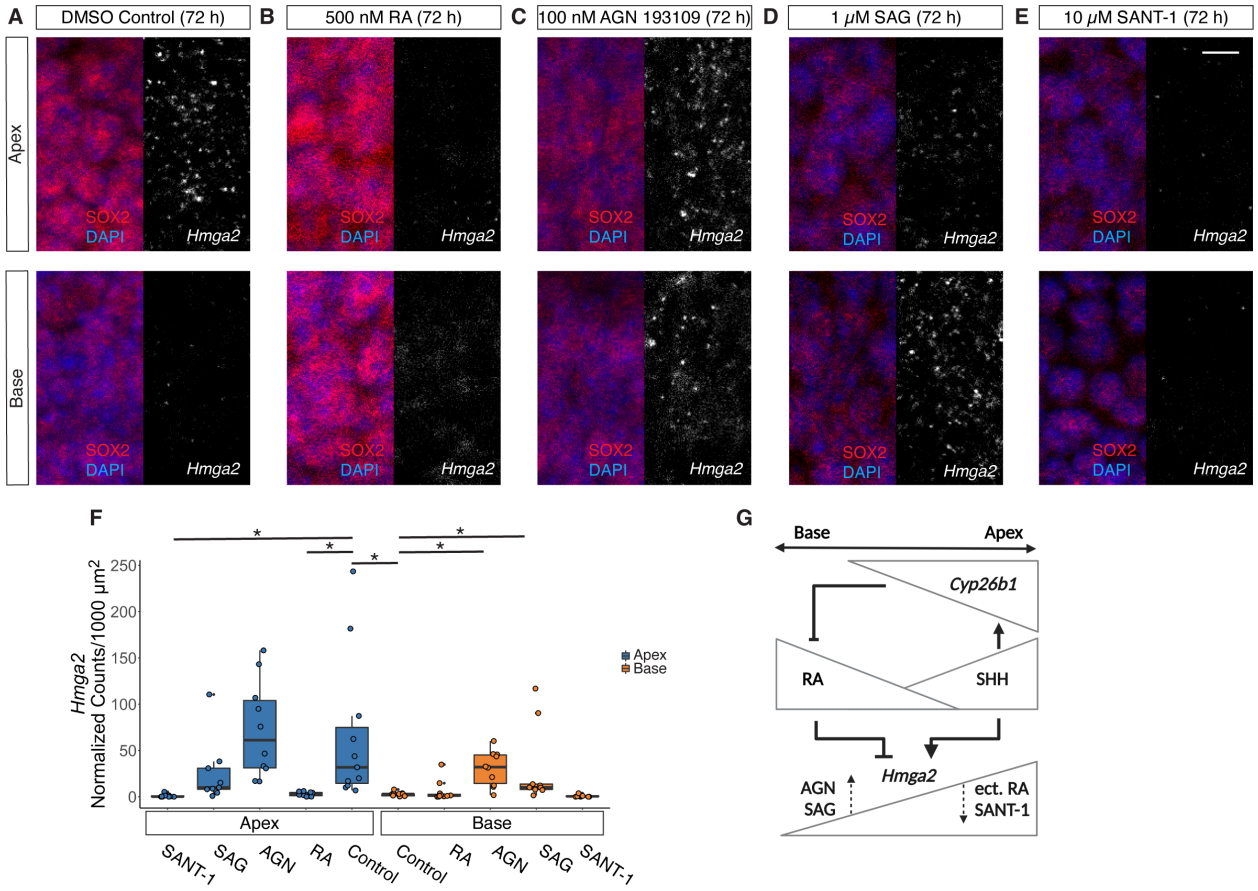

Figure 2.11 Manipulation of RA and SHH signaling results in mirrored phenotypes. (A-E) Representative confocal micrographs of E14.5 cochlear explants cultured for 72 h in (A) control medium or medium supplemented with (B) ectopic RA, (C) the RA receptor blocker AGN 193109, (D) smoothened agonist SAG and (E) smoothened antagonist SANT-1. Explants were stained for *Hmga2* mRNA and counterstained with anti-SOX2 antibody and DAPI. *Sox2*-positive cells of the prosensory domain were imaged at representative locations in apical and basal compartments of the explant, and *Hmga2* puncta were analyzed in Fiji software (Schindelin et al. 2012). (F) Quantification of *Hmga2* puncta normalized to 1000 μm^2 indicated significantly higher *Hmga2* transcript counts for the control apex (n=11) than the control base (n=11). **P*=0.0247 (two-sided paired *t*-test). With the DMSO control as a baseline, differential *Hmga2* expression was determined for the following conditions: exposure to 0.5 μM RA for 72 h resulted in significantly lower *Hmga2* expression in the apical compartment (n=11) than the apical control compartment (n=11). **P*=0.0195 (one-way ANOVA with *post-hoc* Tukey's test). Similarly, blocking SHH signaling with SANT-1 (n=10) resulted in significantly lower *Hmga2* in the apical compartment than in the apical control compartment (n=11). **P*=0.018 (one-way ANOVA with *post-hoc* Tukey's test). In contrast, application of the RA-receptor blocker AGN 193109 (n=10) resulted in significantly higher *Hmga2* in the basal compartment than in the control basal compartment (n=11). **P*=0.0221 (one-way ANOVA with *post-hoc* Tukey's test). The SHH agonist SAG (n=9) also resulted in greater *Hmga2* expression in the basal compartment than in the control basal compartment (n=11). **P*=0.0326 (one-way ANOVA with *post-hoc* Tukey's test). The box plots show the interquartile range (box limits), median (centre

line), minimum to maximum values (whiskers), and biologically independent samples (circles). (G) Summary diagram of the inverse relation between RA and SHH signaling gradients, which is a key component in controlling the tonotopic expression of *Hmga2*. Scale bars (A-E): 10 μm.

2.4 Discussion

Patterning of the apex-to-base axis, a critical step during development of the organ of Corti, provides the spatial information necessary for the differentiation of tonotopically arranged characteristics. Those characteristics are mirrored by tonotopic gene expression gradients, and numerous gene transcripts have been identified to be differentially expressed along the longitudinal axis of the developing mouse cochlea (Son et al. 2012). While signaling pathways, such as the HH pathway, were identified to confer longitudinal information in the mouse cochlea (Son et al. 2015c), the molecular mechanisms providing positional information for regulation of spatial gene expression remain largely unknown. In agreement with the different functions of SHH in organ of Corti development (Son et al. 2015c, Bok et al. 2013, Zhang et al. 2020), we hypothesized that either a genetic timer with asymmetric cell division or a morphogen modulated timer might give rise to graded gene expression (Negrete and Oates 2021). The apex-to-base reconstructions from scRNA-seq data of the E12.5 and E14.5 cochlear floor in 1D space provided a basis for the subsequent apex-to-base alignment and statistical comparison of transcriptional similarities. Therefore, our data analysis strategy integrated spatial and temporal information, thus setting it apart from previously applied trajectory-based analysis of the same tissue (Kolla et al. 2020). The results suggested that gene expression gradients dynamically adjust during the proliferative extension of the prosensory domain, thereby strongly supporting the morphogen modulated model rather than the cell division-associated mechanism.

While the initial hypothesis testing supported the morphogen modulated model, subsequent analysis strategy was specifically tailored to investigate spatiotemporal gene

expression in 3D space. RA signaling was identified as a potential candidate pathway governing spatial identity. RA is a morphogen generally known to be involved in patterning other embryonic organs such as the hindbrain; tissues such as the limb bud (Bok et al. 2011b); and the sensory epithelia of the vestibular end organs (Ohyama et al. 2010). A role for endogenous RA in the organ of Corti has been reported based on the ability to respond to exogenously applied RA and phenotypes observed upon blocking RA receptor alpha (Tateya et al. 2013, Kelley et al. 1993). Expanding on these reports, our results indicate a basal gradient of RA activity in the developing organ of Corti using the *RARE-lacZ* reporter mouse line at E14.5 (Schilling et al. 2012). In agreement with previous findings, our *in vitro* experiments confirmed functional RA signal transduction after the application of exogenous RA. Together, these findings support the hypothesis that RA signaling potentially provides a basis for positional identity during mouse cochlear development.

Further evidence regarding formation of the RA gradient was identified through 3D reconstruction of the cochlear duct for statistical comparison of RA related gene products in different compartments of the model. The RA source and signal receiving cells were found to be spatially separated in the roof and floor. Although this spatial separation may contribute to the formation of RA gradients, other factors must be considered. For example, the cochlear floor may contribute to final RA concentrations, as visualized by low level expression of RA synthesizing enzymes *Aldh1a3* and *Rdh10* in the circular reconstructions of the cochlea and previously reported for the chicken BP (Thiede et al. 2014). In addition, substantial amounts of RA may potentially emanate from areas outside of the cochlear duct such as the periotic mesenchyme (Raz and Kelley 1999). Therefore, tissue-specific enzymatic networks negatively controlling RA availability are relevant. CYP26B1 (Romand et al. 2006) and DHRS3 (Ono et al.

2020b) are part of the catabolizing network to reduce RA bioavailability, and both are expressed in decreasing apex-to-base gradients in the cochlear floor at E14.5. This finding suggests that both enzymes contribute to shaping the RA gradient, as has been observed in the developing forebrain, spinal cord, and vestibular end organs in mice (Ohyama et al. 2010, Ono et al. 2020a, Szuts and Harosi 1991). Specifically, in the E6.5 chicken BP a decreasing base-to-apex gradient of *Raldh3* and an inversely oriented gradient for *Cyp26c1* have been reported. These findings suggest that a similar decreasing base-to-apex gradient of RA is also present in the E6.5 chicken BP; however, an inversion of the gradient was reported for later time points (Thiede et al. 2014). With respect to the mouse cochlea, our data indicate a stable RA gradient between E12.5 and P0, instead a general downregulation of the RA signal has been reported for the adult mouse cochlea (Tateya et al. 2013). In summary, these findings further support the hypothesis that an RA gradient confers spatial information in the mouse cochlea.

Intriguingly, the gradient of RA along the apex-to-base axis depends not only on physical parameters such as diffusion but also on catabolizing enzymes, thus prompting questions regarding the pathways functioning upstream of the enzymes. During hindbrain development, CYP26 proteins have been shown to integrate Fgf signaling (Feng et al. 2010). However, no tonotopically differential enrichment for Fgf signaling was found in our analysis of the cochlear reconstruction. In comparison, HH signaling is known to specify apical identity in the mouse and chicken cochlea, and differential enrichment scores were confirmed with our model of the E14.5 cochlea. Our findings regarding the graded RA activity implied the existence of opposing morphogen gradients between RA and SHH in the cochlea. A similar inverse relationship between both pathways has been reported in motor neuron specification (White et al. 2007, Sockanathan and Jessell 1998) and differentiation of the forebrain (Novitch et al. 2003, Ribes et

al. 2006). Furthermore, transcriptional control of HH signaling over *Cyp26* expression has been confirmed for forebrain patterning and limb bud development (Schneider et al. 2001, El Shahawy et al. 2019). In agreement with these reports, we observed differential upregulation of *Cyp26b1* after exposure to the HH agonist SAG across the total length of the E14.5 cochlear explant. In contrast, RA signaling has been reported to negatively control HH signaling by inhibiting GLI activity in immortalized mouse keratinocytes (Probst et al. 2011). A potential interaction between RA and HH signaling pathways prompts the question of whether a carefully regulated equilibrium between both morphogens might be involved in patterning spatial identity in the mouse cochlea. Application of an RA-receptor blocker or an HH agonist induced expression of the apical reporter *Hmga2* in the basal compartment of the explant. In contrast, exogenous RA or blocking of HH signaling decreased the expression of the apex-to-base reporter in the apical compartment. In summary, our predictions based on the spatial reconstruction of the cochlea supported by our pharmacological approach resulting in mirrored phenotypes provided initial evidence suggesting that opposing RA and SHH gradients function to pattern the apex-to-base identity of the mouse embryonic cochlear duct.

In conclusion, in this study, we presented 3D reconstructions of the developing cochlear duct for two developmental time points from scRNA-seq data. Predictions based on our model were validated *in vivo* and with functional experiments in organ of Corti explants, thus suggesting that our model provides a valuable tool for further investigation of the embryonic development of the organ of Corti.

2.5 Methods

2.5.1 Experimental model

All animal maintenance and experimental procedures were performed in accordance with NIH guidelines and were approved by the Institute Animal Care and Use Committee at the University of Michigan (protocol: PRO00010056, J.W.).

RARE-lacZ (Tg(RARE-Hspa1b/lacZ)12Jrt), *Sox2*-GFP (B6;129S-Sox2tm2Hoch/J) and FVB/NJ mice were purchased from Jackson Laboratory. Sex of mouse samples in this study was not characterized.

2.5.2 Single cell isolation and flow sorting

The inner ear labyrinths from E12.5 and E14.5 *Sox2*-GFP embryos were dissected, and a fluorescent dissection microscope was used to identify the GFP-positive cochlea and the various GFP-positive sensory epithelia in the vestibular compartment. Subsequently, the cochlea was separated from the vestibulum based on this evaluation. Cochlear ducts were processed for single cell preparation as previously described (Fornes et al. 2020). To enrich for cochlear duct cells, we purified cells with FACS with a MoFlo Astrios instrument (Beckman Coulter, University of Michigan Flow Cytometry Core). These samples were then used for standard 10x Genomics preparations for scRNA-seq experiments.

2.5.3 10x Genomics protocol

Single-cell processing and next-generation sequencing were performed at the Advanced Genomics Core at the University of Michigan. Sequencing was performed with a 10x Chromium and Next GEM accessory kit (10x Genomics, 1000202) and Chromium Next GEM Chip G Single Cell Kit (10x Genomics, 1000120) for scRNA-seq. The following kits were used for library preparation: Chromium Next GEM Single Cell 3' Kit v3.1 (10x Genomics, 1000268),

Library Construction Kit (10x Genomics, 1000190), and Dual Index Kit TT Set A (10x Genomics, 1000215).

2.5.4 scRNA-seq analysis

E12.5 and E14.5 datasets were analyzed individually with the Seurat v4 pipeline (Hao et al. 2021). First, we selected cells according to the number of expressed genes (E12.5: 200-6,000; E14.5: 200-9,500). The maximum allowed fraction of mitochondrial genes per cell was set to 8% and 10%, respectively. Overall, 552 cells for E12.5 and 1,159 cells for E14.5 passed the quality control for further analysis. After the pre-processing step, log normalization was performed, and the top 2,000 (E12.5) and 3,000 (E14.5) highly variable genes were identified with the *vst* method with default settings. We scaled the datasets to avoid the domination of highly expressed genes and used the data as input for PCA to decrease the dimensions. The first 30 principal components for both E12.5 and E14.5 data were chosen to construct the shared nearest neighbor graph with 20 nearest neighbors (*k.param=20*). The shared nearest neighbor modularity optimization-based clustering algorithm was used to identify clusters with resolution 0.45 and 0.5, respectively. We used UMAP to visualize the scRNA-seq clustering results and metadata information, such as read depth and sample ID. To determine cell identities for each cluster, we first identified DEGs for each cluster with the *FindAllMarkers* function in the Seurat package with the following parameters: *only.pos=TRUE, min.pct=0.25, logfc.threshold=0.25, test.use="wilcox"*. Adjusted Bonferroni-corrected *P*-values of 0.05 were used for multiple testing correction. We determined cell identities by comparing cluster specific DEGs with published canonical marker genes.

2.5.5 LIGER multiple datasets integration

We applied LIGER (Welch et al. 2019) to jointly define cell identities from multiple scRNA-seq datasets. Briefly, LIGER delineates shared and dataset-specific features to integrate multiple scRNA-seq data by using non-negative matrix factorization. We initialized the LIGER object by using normalized data from Seurat v4 with two input data: E12.5 and E14.5. We scaled the data to avoid the domination of highly expressed genes by using the *scaleNotCenter* function. Then we used a joint matrix factorization algorithm on the normalized and scaled object with 20 defined latent variables (*k=20*). We conducted quantile normalization, Louvain clustering (*resolution=0.25*), dimensionality reduction, and visualization with UMAP (*distance="cosine", n_neighbors=20, min_dist=0.3*). To validate the Seurat clustering, we projected annotated cell types onto the co-embedding UMAP.

2.5.6 3D cylinder reconstruction

To reconstruct the 2D and 3D original structure of the cochlea, we first identified sub-clusters of the cochlear duct by using CellTrails (Ellwanger et al. 2018) for the E12.5 and E14.5 datasets. The cells of the cochlear apex, cochlear base, and cochlear roof cluster were used to generate a gene expression matrix as input. Next, we applied the spectral embedding function *embedSample* with default parameters to find a low-dimensional representation and determined 9 and 12 latent variables for E12.5 and E14.5, respectively. Hierarchical clustering with a *post-hoc* test was conducted to determine states with the function findStates with the following parameters: E12.5: *min_size=0.01, min_feat=2, max_pval=1e-4, min_fc=1.5*; E14.5: *min_size=0.01, min_feat=2, max_pval=1e-4, min_fc=1.5*. We annotated CellTrails states by leveraging canonical gene markers.

To resolve the original anatomy of the developing cochlea, we conducted PCA for E12.5 and E14.5 data by using DEGs between CellTrails states of the cochlear duct and DEGs among

the apex, base, and roof clusters identified from Seurat. Next, we visualized the PCA results on 2D scaled PCA plots in which the *x*-axis showed *arctan(PC3/PC2)*, and the *y*-axis represented PC1. To reconstruct the 3D space of the cochlea, we projected the cells onto a cylindrical surface for E12.5 and E14.5. Specifically, we scaled the PC2 and PC3 as the *x*-axis and *y*-axis to project the cells onto a circle. We used PC1 to resolve the height of each individual cell as the *z*-axis in the 3D cylinder projection. For better visualization, we flattened the tonotopic axis by multiplying PC2 and PC3 by the factor h, corresponding to PC1, scaled by the difference in the maximum and minimum of the PC1 values.

2.5.7 Otoscore quality control

To calculate the otoscore, we employed murine P1 whole-genome expression microarray datasets from cochlear and vestibular HCs and epithelial non-HCs (ENHCs). First, the limma (Durruthy-Durruthy et al. 2014) package was utilized to identify DEGs between auditory and vestibular HCs and ENHCs, respectively. Based on those gene sets, we used AUCell (Aibar et al. 2017) to calculate cochlear and vestibular HC enrichment scores (cHCscore and vHCscore) for E12.5 and E14.5 for HC precursor, while cENHCscore and vENHCscores were determined for E12.5 and E14.5 SC precursor cells and cochlear floor cells. For comparison, similar scores were calculated for previously published and annotated E14.5 cochlear (Kolla et al. 2020) and E16.5 vestibular (Wilkerson et al. 2021) HCs and SCs. The otoscore was determined as follows: *cHCscore - vHCscore* for the HC precursors or *cENHCscore - vENHCscores* for the floor and SC precursor cells. As a quality control measure, only cells with positive otoscores were considered to be of cochlear origin for the purpose of this study.

2.5.8 Gradually expressed gene identification

The E12.5 and E14.5 datasets were analyzed separately with the same pipeline. First, for each individual gene, we conducted Wilcoxon sum-rank tests (P-value < 0.05) as a feature selection step to determine whether the gene was significantly different between cochlear apex and base. Next, DEGs were analyzed to identify GEGs along the tonotopic axis. Specifically, PCA was performed by using all genes as features, and PC1 was used to approximate each cell's relative position along the apex-to-base axis. For each individual gene, LOWESS regression (William) was used to determine the relationship between the gene expression level and PC1. In addition, linear theoretical lines along the apex-to-base axis were generated according to the maximum and minimum value of each gene. The regression line as an empirical line was compared with the simulated theoretical line by using Kullback-Leibler (KL) divergence (Kullback and Leibler) with a KL threshold less than 0.7. To remove genes that were not gradually expressed along the tonotopic axis, we calculated the expression level difference between the maximum value and the minimum value for each individual gene. Genes with differences less than 0.5 were removed from further analysis. Additionally, GEGs were classified into two categories: genes with decreasing or with increasing expression levels along the apex-to-base axis. Finally, overlapping candidate genes were filtered for identical gradient orientation between the E12.5 and E14.5 time points.

2.5.9 Hypothesis testing with a similarity matrix

To test two potential mechanisms conferring tonotopic identity, we calculated pairwise cell similarity scores between the E12.5 and E14.5 datasets. Specifically, we first generated metacells to denoise the dataset by aggregating the ten nearest neighbor cells for E12.5 and E14.5 data. By using the GEGs, we calculated the Euclidean distance for each pair of metacells between E12.5 and E14.5. Next, several methods were used to convert the distance matrices into

similarity matrices. For the Euclidean distance matrix, the traditional inverse method ($\frac{1}{1+distance}$) or radial basis function (exp $(-\frac{distance^2}{2\sigma^2})$) was used to generate the similarity matrix. σ bandwidth, was a hyperparameter. In our analysis, we defined $\sigma^2 = 4$. For cosine distance matrix, similarity scores were calculated as $1 - distance$. Finally, the similarity matrix was visualized with a heatmap. Metacells of both age groups were ordered along the apex-to-base axis according to the PC1 value extracted from the PCA by using all genes as features.

To test the robustness of our analysis, we first used a denoised dataset to calculate the pairwise metacell similarity matrix with the MAGIC algorithm. Next, we decreased the number of cells contributing to the metacells to five. To test how the features affected the similarity analysis, we relaxed the KL divergence threshold to identify more GEGs with KL less than 1. In addition, GEGs were replaced with overlapped highly variable genes between the E12.5 and E14.5 datasets. The overlapped highly variable genes were identified with the Seurat v4 package *FindVariableFeatures* function. Furthermore, different distance metrices, such as Euclidean distance and cosine distance, were used to validate the consistency of the analysis. The conversion method, including the inverse method and radial basis function method, was also used to demonstrate the robustness of our analysis. Finally, to simulate a situation supporting the time-space translation model, we compared E12.5 data with a computationally truncated E14.5 cochlear duct by removing the basal one-third of cells from the E14.5 data.

2.5.10 Spatial reconstruction of the cochlear floor including HCs and SCs

To resolve the relative positions of the cochlear floor cells including HCs and SCs, we conducted PCA by leveraging the cochlear floor specific GEGs as features. HCs, SCs, and remaining floor cells after otoscore QC were represented in individual columns of the 1D PCA

visualizations. The y-axis of the PCA plot indicates the tonotopic axis, whereas cells were randomly distributed along the x-axis for better visualization.

2.5.11 Differential pathway analysis

AUCell (Aibar et al. 2017) was used to identify differentially enriched pathways at single-cell resolution. AUCell, a ranking-based method, uses the area under the recovery curve to determine the GO term enrichment (Ashburner et al. 2000) in individual cells. GO terms containing at least four genes were subjected to further analysis. First, we selected cells annotated as cochlear duct after otoscore QC, including the cochlear floor and cochlear roof; we then ranked all genes for each cell by using the function *AUCell_buildRanking* with default settings. Next, the area under the curve for each GO term for each cell was calculated with the *AUCell_calcAUC* function, and the top 10% of genes in the ranking were used. To identify the differentially enriched GO terms between the cochlear apex and cochlear base, we selected the corresponding cells and conducted Wilcoxon sum-rank tests with Benjamini-Hochberg (BH) correction (adjusted $P < 0.05$) for the E12.5 and E14.5 datasets. Similarly, we determined differentially enriched GO terms between cochlear roof and cochlear floor cells. To visualize the differentially enriched pathways between the cochlear apex and cochlear base for both time points, we generated heatmaps with hierarchical clustering for the top 100 differentially enriched GO terms for each cluster. Cells were rank ordered along GEG based PC1.

2.5.12 Cochlear explant culture

Timed-pregnant FVB/NJ female mice were euthanized at E14.5, embryos of either sex were collected, and cochlea were dissected and cultured as explants between 3 and 72 h. Briefly, the cochlea was separated from vestibular compartments and the whole cochlea was cultured

under floating conditions to maintain the 3D structure. Explants were maintained in Neurobasal-A medium supplemented with N2, L-glutamine, D-glucose, and ampicillin (Thermo Fisher) at 37 °C in 5% CO2. Explants were supplemented with 500 nM RA (Sigma-Aldrich) in 0.1% DMSO from the beginning of the culture. To inhibit RA signaling, we treated explants with 100 nM AGN 193109 (Sigma-Aldrich) in 0.1% DMSO from the beginning of culture. The SHH signaling pathway was activated with 1 μM SAG (Stemcell Technologies) in 0.1% DMSO and inhibited by 10 μM SANT-1 (Stemcell Technologies) in 0.1% DMSO, both from the beginning of culture. Controls were treated with 0.1% DMSO alone. Explants were then fixed and subjected to *in situ* staining and immunolabeling to examine the expression of transcripts during cochlear development.

2.5.13 Quantitative FISH

Cochlear whole mounts were processed according to published protocols (van Dijk et al. 2018). To restrict data acquisition to the prosensory domain of the cochlea, we stained explants with anti-SOX2 antibody (Santa Cruz Biotechnology) and counterstained them with DAPI (Thermo Fisher). HCR probe sets were obtained (Molecular Instruments) to detect *Cyp26b1* (Molecular Instruments, NM_175475, lot: PRK769), *Hmga2* (Molecular Instruments, NM_010441.2, lot: PRL079), *Hmgb2* (Molecular Instruments, NM_001363445.1, lot: PRL007), *Atoh1* (Molecular Instruments, NM_007500.5, lot: PRL500), and *Lfng* (Molecular Instruments, NM_008494.3, lot: PR1896) transcripts. Z-stacks were acquired with a laser scanning confocal microscope (Leica, SP8), and 145 × 145 μm images with 0.3 μm spacing were collected. Transcript puncta were counted through an automated semi-approach (Diaz and Heller 2021) in Fiji software. First, five optical *z*-slices with 0.7 μm thickness were used for analysis. Regions of interest (ROIs) covering the prosensory domain were applied on the basis of the *Sox2* signal.

Background was removed from the images with a top hat filter, and images were smoothed with a Gaussian kernel to remove noise. Transcripts were detected as local maxima in this image and distinguished from background noise with an identical intensity threshold applied to all analyzed images. Transcripts were segmented through watershed segmentation, and the ROIs were automatically counted. The total number of puncta per ROI was normalized to 1000 μm^2.

Two-sided *t*-tests were used for comparisons between two groups. To compare the difference between apical and basal compartments under the same experimental condition, we used two-sided paired *t*-tests. Additionally, one-way ANOVA followed by Tukey's multiple comparison tests were used for more than two conditions. We conducted a one-way ANOVA on five different condition groups for the apex and base. Data distribution was assumed to be normal, but not formally tested.

2.5.14 Immunofluorescent staining

Cochlear samples from E14.5 mice were fixed in 4% paraformaldehyde (Electron Microscopy Sciences) diluted in 1XPBS (Thermo) for 4 hours on ice, washed in 1XPBS (Thermo), subjected to a sucrose gradient, then embedded in O.C.T. Compound (Fisher) for cryosectioning at 10 μm thickness. Sections were blocked in 1% bovine serum albumin (BSA, Thermo Scientific, BP9700100) in 2% Triton-X/1XPBS for 60 minutes at room temperature and primary antibodies were applied overnight at 4°C in 0.5% BSA/2% Triton-X/1XPBS. The following primary antibodies were used: RDH10 (Proteintech), ALDH1A3 (Abcam), and β-Galactosidase (Abcam). Secondary antibodies were applied in 0.5% BSA/2% Triton-X/1XPBS for 90 minutes at room temperature followed by DAPI (Sigma) nuclear staining. All washes following primary and secondary antibody application were performed with 2% Triton-

X/1XPBS. All fluorescent images were acquired using a laser scanning confocal microscope (Leica, SP8).

2.5.15 β-Galactosidase histochemical staining

Inner ears were dissected at E14.5 from *RARE-lacZ* mouse embryos and drop-fixed in 0.2% glutaraldehyde for 6 h at room temperature. β-Galactosidase staining followed the protocol described previously (Schindelin et al. 2012). We used Red-gal (Sigma-Aldrich, RES1364C-A102X) for the chromogenic reaction.

2.5.16 Statistics and reproducibility

Statistical analysis was performed using R on RStudio. A two-sided *P* value of < 0.05 was considered statistically significant.

2.5.17 Data and code availability

All scRNA-seq raw and processed sequencing data generated in this study have been deposited to the NCBI Gene Expression Omnibus database and can be retrieved using the accession number GSE202588. Source data are provided with this paper. For reviewers, please use the token epotqscanxqfpwn to access the data in GEO. The codes for computational analyses are available on GitHub (https://github.com/waldhaus/3D_cochlea). All of the packages used are available online.

2.6 Acknowledgements

We thank the staff at the University of Michigan Advanced Genomics Core for help and support, and members of the laboratory of J.W. and Linghua Jiang for discussion of the manuscript. We thank Nenad Sestan for support with the *RARE-lacZ* mouse model and Donna

Martin and Keith Duncan for helping with ALDH1A3 and β-galactosidase antibodies, respectively. This work was supported by NIDCD/NIH grant (R21DC015861) to J.W.

2.7 My contributions

This project is under review in Developmental Cell and the preprint is available in (Wang 2022); as indicated by the author list for that paper, this was a project I undertook with Dr. Saikat Chakraborty, Yujuan Fu, Dr. Mary P. Lee, Dr. Jie Liu, and Dr. Joerg Waldhaus. The diverse set of analyses contained within this work was only possible thanks to the efforts of that diverse team. I performed the bioinformatics, computational, and statistical analyses, including analysis of multiple scRNA-seq data produced for the manuscript. Dr. Joerg Waldhaus and I wrote the manuscript; my writing contribution focused on the bioinformatics analyses and methods sections.

Chapter 3 Mapping the Regulatory Landscape of Auditory Hair Cells from Single-cell Multi-omics data

3.1 Abstract

Auditory hair cells transduce sound to the brain and in mammals these cells reside together with supporting cells in the sensory epithelium of the cochlea, called the organ of Corti. To establish the organ's delicate function during development and differentiation, spatiotemporal gene expression is strictly controlled by chromatin accessibility and cell type specific transcription factors, jointly representing the regulatory landscape. Bulk-sequencing technology and cellular heterogeneity obscured investigations of the interplay between transcription factors and chromatin accessibility in inner ear development. To study the formation of the regulatory landscape in hair cells, we collected single-cell chromatin accessibility profiles accompanied by single-cell RNA data from genetically labeled murine hair cells and supporting cells after birth. Using an integrative approach, we predicted cell type specific activating and repressing functions of developmental transcription factors. Furthermore, by integrating gene expression and chromatin accessibility datasets, we reconstructed gene regulatory networks. Then, using a comparative approach, 20 hair cell specific activators and repressors, including putative downstream target genes, were identified. Clustering of target genes resolved groups of related transcription factors and was utilized to infer their developmental functions. Finally, the heterogeneity in the single-cell data allowed us to spatially reconstruct transcriptional as well as chromatin accessibility trajectories, indicating that gradual changes in the chromatin accessibility landscape were lagging behind the transcriptional identity of hair cells along the organ's

longitudinal axis. Overall, this study provides a strategy to spatially reconstruct the formation of a lineage specific regulatory landscape using a single-cell multi-omics approach.

3.2 Introduction

The mammalian genome was estimated to encode approximately 30,000 protein-coding genes (Shabalina and Spiridonov 2004) and numerous unique combinations of the related gene products account for the molecular variety of the different cell types forming an organism. To orchestrate gene expression and to ensure proper differentiation of a given lineage, a delicate interplay between transcription factors (TFs) and chromatin accessibility controls the developmental program (Klemm, Shipony and Greenleaf 2019a). The transcriptional landscape from isolated tissues to whole organisms (Wagner et al. 2018, Packer et al. 2019) has been reconstructed using single-cell whole transcriptome data and resulted in the development of a variety of bioinformatics algorithms (Bendall et al. 2014, Trapnell et al. 2014, Guo et al. 2017, Qiu et al. 2017b, Ellwanger et al. 2018). More recently, single-cell assay for transposase accessible chromatin sequencing (scATAC-seq) protocols became available to investigate chromatin accessibility at matching resolution (Mezger et al. 2018). The technology identifies accessible chromatin regions, which potentially harbor regulatory elements that can be utilized to characterize genome-wide DNA/TF interactions (Buenrostro et al. 2013). In combination, single-cell RNA-seq (scRNA-seq) and scATAC-seq technologies offer the potential to resolve dynamic changes in the regulatory landscape (Buenrostro et al. 2018). However, data interpretation remains challenging due to the sparsity of the scATAC-seq data and biological complexity of the model organism investigated.

The murine organ of Corti is an excellent model to study the development of the regulatory landscape since it consists of only two major cell types, sensory hair cells (HCs) and

supporting cells (SCs), that originate from a shared progenitor (Xu et al. 2017). The two major cell types can be subdivided phenotypically (Corti 1851) as well as transcriptionally (Burns et al. 2015, Kolla et al. 2020) into inner HCs (IHCs), outer HCs (OHCs), and a number of different SC types. Tight spatiotemporal control is required for development of the organ of Corti, which occurs in waves both molecularly (Lee et al. 2006b) and functionally (Lelli et al. 2009) starting at the base and extending towards the apex of the organ. Therefore, isolation of individual cells from the whole organ of Corti at a single developmental time point mirrors a continuum of differentiation, where cells isolated from the base are more mature compared to the cells from the apex. At the transcriptional level, those differences in gene expression were sufficient to reconstruct the organ of Corti in 2-dimensional space from single-cell q-PCR data (Waldhaus et al. 2015). The aim of our study is to identify the regulatory landscape controlling the differentiation and maturation of the organ of Corti. Here we provide a framework of how to analyze the regulatory landscape of HC differentiation using an integrative single-cell pipeline.

3.3 Results

3.3.1 Isolation of organ of Corti HCs and SCs

We generated scATAC-seq profiles from isolated HCs and SCs using fluorescence activated cell sorting (FACS) in combination with the ATOH1-GFP (Rose et al. 2009)/FGFR3-iCRE (Young et al. 2010)/Ai14-tdTomato (Madisen et al. 2010) mouse line at postnatal day 2 (P2) (**Figure *3.1*A**). ATOH1-GFP-expression labeled sensory HCs, whereas conditional expression of tdTomato delineates two SC types, namely Pillar cells (PCs) and Deiters' cells (DCs) (**Figure *3.1*A-B**). Apical OHCs showed co-expression of GFP and tdTomato as previously reported (Waldhaus et al. 2015). After microdissection, we divided cochlear ducts into apical and basal compartments, dissociated the tissue to single-cell level, and performed FACS to enrich for

HCs and PC/DCs (**Figure *3.1*A, C** and **Figure *3.2*A**). Library preparation of sorted cells was performed using the 10x Genomics scATAC-seq platform, and upon application of stringent quality criteria, we yielded high-quality profiles of 1,210 single-cells (**Figure *3.1*D**). The cells clustered into 6 populations (**Figure *3.1*E**) with a median unique fragment count of 17,048 per cell (**Figure *3.2*B**). Fragments were enriched at transcriptional start sites (TSS) (**Figure *3.2*C**), as well as in distal intergenic regions and introns (**Figure *3.2*D**). The length of fragments accumulated at 100bp and 200bp, indicating nucleosome-free and mono-nucleosome-bound fragments (**Figure *3.2*E**).

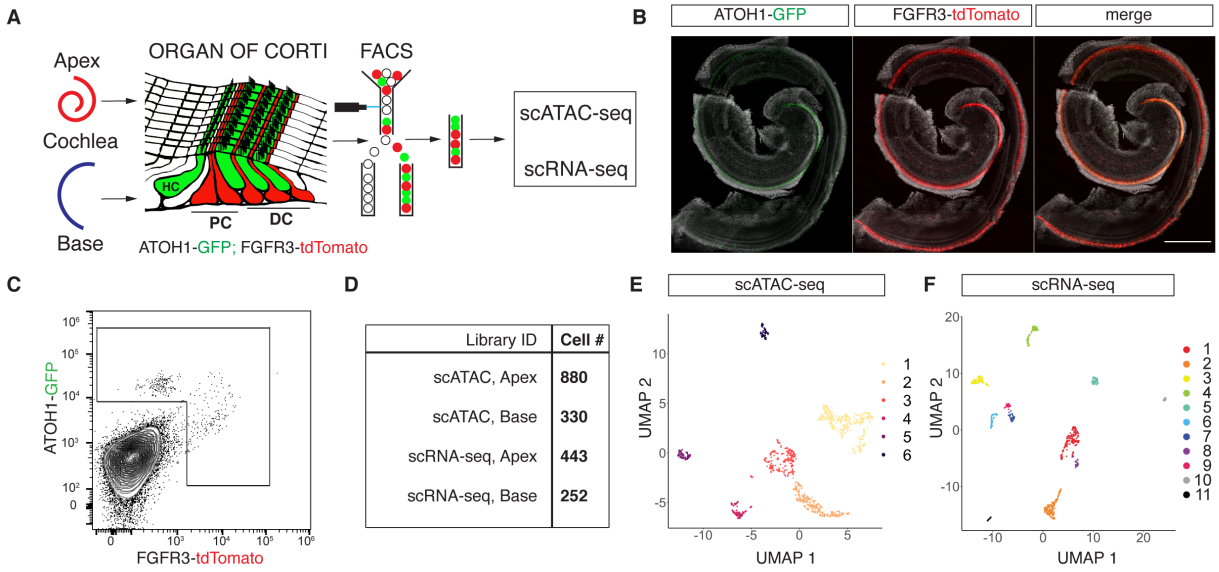

Figure 3.1 scATAC-seq and scRNA-seq profiling of isolated HCs and PC/DCs. (A) Schematic representation of the experimental workflow used in this study. (B) Representative fluorescent reporter gene expression of ATOH1-GFP and FGFR3-tdTomato in wholemount preparations of the organ of Corti at P2. Scale bar represents 200 µm. (C) FACS plot and gating strategy to isolate cells expressing GFP and tdTomato. (D) Table summarizing sequencing libraries generated and total number of cells per library after quality control. (E-F) UMAP plots to show the clustering of all organ of Corti cells processed in two aggregated libraries to rule out technical variations for (E) scATAC-seq and (F) scRNA-seq experiments.

To generate age matched scRNA-seq data with identical genetic background, we collected apical and basal compartments from P2 ATOH1-GFP/FGFR3-iCRE/Ai14-tdTomato cochlea for a second time. After single-cell dissociation, we performed FACS and applied less

stringent gating criteria compared to the scATAC-seq sorting paradigm to ensure a complete overlap with the previously sorted populations. After library preparation using the 10x Genomics scRNA-seq platform, sequencing, and quality control, we analyzed the transcriptomes of 695 cells and identified 11 clusters (**Figure *3.1*D, F**) with a median unique count of 12,343 reads per cell (**Figure *3.2*E**).

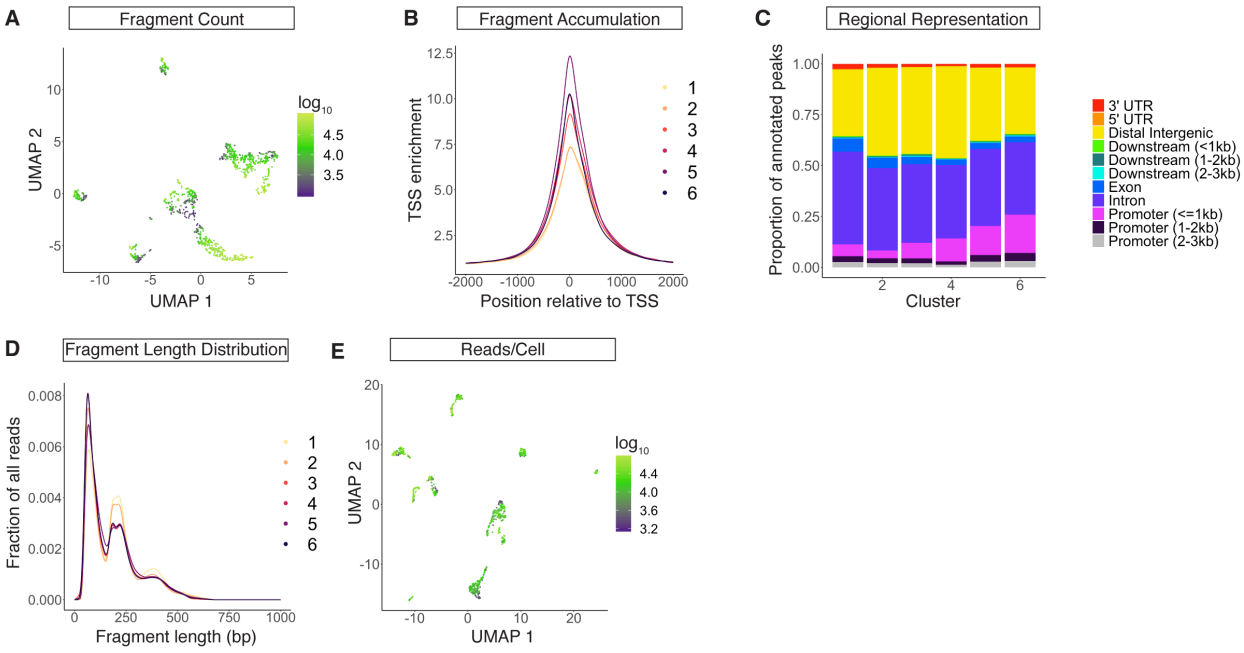

Figure 3.2 Quality control of scRNA-seq and scATAC-seq data. (A) UMAP plot of unique fragment counts per cell in log10 scale of scATAC-seq dataset. (B) scATAC-seq fragment accumulation relative to TSS position using ataqv. (C) Genomic region composition of DARs for each cluster from scATAC-seq data. (D) Fragment length distribution for each scATAC-seq cluster. (E) UMAP plot of unique read counts per cell in log10 scale of scRNA-seq dataset.

3.3.2 Identification of organ of Corti cell types using a similarity matrix

Cellular identities of scATAC-seq data were annotated based on similarities between the scATAC-seq and scRNA-seq clusters. First, we identified 11 clusters from scRNA-seq data using Seurat v3 (Stuart et al. 2019). Each of the 11 scRNA-seq clusters were compared with the remaining cells in order to establish a list of differentially expressed genes (DEGs) (**Figure *3.3*A**). Overall, we identified a total of 5,772 DEGs with a median number of 428 DEGs per

cluster. Known markers among the DEGs were used to determine scRNA-seq cluster identities (**Figure *3.4*A**). Periotic mesenchyme markers like *Pou3f4* and *Tbx18* (Phippard et al. 1998, Trowe et al. 2008) were among the genes differentially expressed in cluster 1, whereas *Fabp7*, *Mpz*, and *Egfl8* (Wang et al. 2013, Weiss et al. 2016, Suzuki et al. 2019) in cluster 2 indicated Schwann cell identity. PCs and DCs were represented in cluster 3 as demonstrated by *Fgfr3*, *Prox1*, and *Hes5* expression (Bermingham-McDonogh et al. 2006, Hartman et al. 2009, Hayashi et al. 2010). Endothelial cells and melanocytes were captured in clusters 4 and 5 as evident by the expression of *Cldn5*, *Cdh5*, *Sox17* (Gory-Fauré et al. 1999, Morita et al. 1999, Zhou et al. 2015) and *Gsta4*, *Pmel*, *Ptgds* (Takeda et al. 2006, Uehara et al. 2009, Hellström et al. 2011), respectively. *Atoh1*, *Pou4f3*, and *Gfi1* (Xiang et al. 1997, Wallis et al. 2003, Woods et al. 2004) were DEGs of sensory HCs characteristic for cluster 6, while lateral SCs in cluster 7 expressed *Gata2*, *Fst*, and *Hs3st1* (Lilleväli et al. 2004, Hartman et al. 2015, Son et al. 2015c). Cluster 8 represented proliferating Schwann cells distinguished by *Fabp7*, *Top2a*, and *Cdc20* (Fuhrmann et al. 2018, Jessen and Mirsky 2019) expression. *Crabp1*, *Slc12a2*, and *Atp1b1* (Kolla et al. 2020, Mutai et al. 2020) indicated medial SCs in cluster 9. Cells in cluster 10 represented roof structures consisting of Reissner's membrane and stria vascularis based on *Oc90*, *Otx2*, and *Cldn8* expression (Kitajiri et al. 2004, Hartman et al. 2015, Vendrell et al. 2015). Finally, immune cells expressed markers like *Lyz2*, and *C1qa* (van Schaarenburg et al. 2016, Cochain et al. 2018) in cluster 11. Next, we identified 6 clusters from scATAC-seq data and cluster-specific differentially accessible regions (DARs) were determined using SnapATAC (Fang et al. 2019) (**Figure *3.3*B**). In summary, we identified a total of 67,415 DARs with a median number of 6,495 DARs per cluster. Subsequently, a proximity-based approach was used to annotate DARs to genes which allowed us to compare similarities between DEGs and annotated DARs using a

Jaccard index similarity matrix (**Figure *3.3*C**). scATAC-seq cluster 1 exhibited the highest similarity to the scRNA-seq HC cluster, while scATAC-seq cluster 2 corresponded to the PC/DC cluster. scATAC-seq clusters 3 through 6 were identified as roof, mesenchyme, endothelial, and immune cells based on their similarities to the scRNA-seq clusters, respectively. Medial and lateral SC-, as well as Schwann cell- and melanocyte scRNA-seq clusters did not exhibit high similarities to any of the scATAC-seq clusters, probably due to the lenient flow sorting strategy applied to the scRNA-seq samples. To validate the accuracy of the similarity-based approach, we integrated scRNA-seq and scATAC-seq for joint alignment analysis using LIGER (Welch et al. 2019) (**Figure *3.4*B-C**). Projecting the similarity-based approach identities onto the LIGER co-embedding UMAP revealed high similarity in cell type annotations for both approaches (**Figure *3.4*C**). Due to the larger number of scATAC-seq cells, the LIGER clustering was dominated by scATAC-seq cells, which potentially obscured the identity of smaller clusters. Therefore, the Jaccard similarity matrix provided an efficient approach to identify and annotate cell types represented by small numbers of cells.

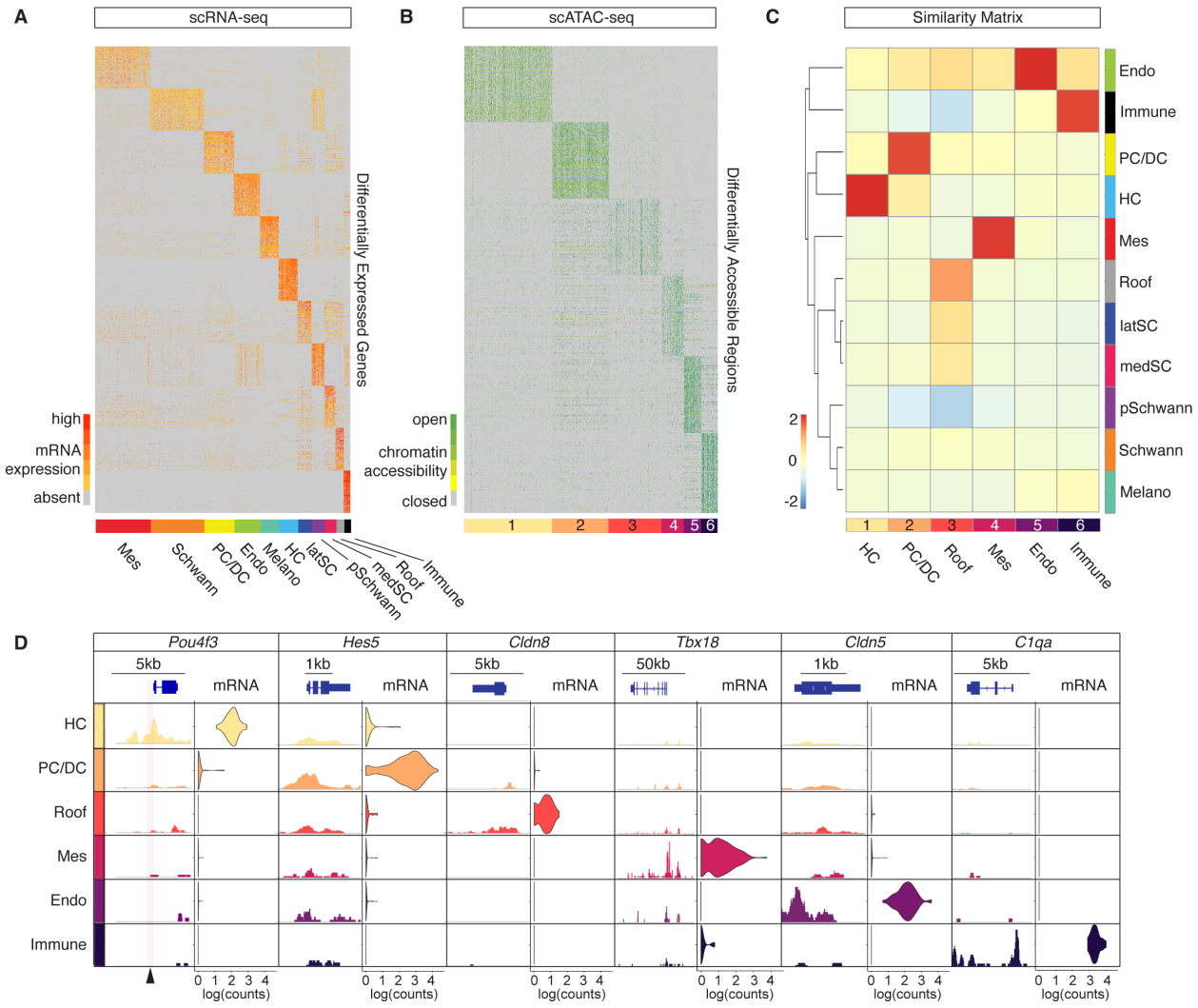

Figure 3.3 scATAC-seq and scRNA-seq cell type identification. (G) Expression heatmap for 695 organ of Corti scRNA-seq cells (*x*-axis) and DEGs (*y*-axis). Shown are the top 100 DEGs for each of the 11 clusters identified. Cluster identities were determined based on DEGs known as canonical markers and indicated with a color bar at the bottom of the heatmap. (H) Accessibility heatmap for 1,210 scATAC-seq cells. Top 100 DARs for each of the 6 clusters identified are shown and cluster IDs are indicated with a color bar at the bottom of the heatmap. (I) Jaccard index similarity matrix reveals relations between scATAC-seq clusters and scRNA-seq clusters based on the overlaps between DEGs and annotated DARs. scATAC-seq cluster annotations were determined by the similarity to scRNA-seq clusters (color coded as in A and B). (J) Enrichment of chromatin accessibility and expression level of candidate genes corresponding to their clusters. Accumulated scATAC-seq fragments at the individual gene locus (left column) and normalized gene expression levels in violin plots (right column) for the 6 scATAC-seq clusters. Arrowhead at the bottom of the plot indicates a position of a previously published organ of Corti specific regulatory element (Wilkerson et al. 2019a).

Generally, DARs are likely to be enriched in gene bodies and gene regulatory elements controlling expression of individual transcripts. To test the quality of our scATAC-seq data, we identified 5 DARs overlapping with previously published organ of Corti-specific enhancer elements (Wilkerson et al. 2019a). Next, we visualized cluster-specific candidate genes contributing to the Jaccard similarity matrix. We plotted chromatin accessibility around the gene body as well as transcript levels, accordingly (**Figure *3.3*D**).

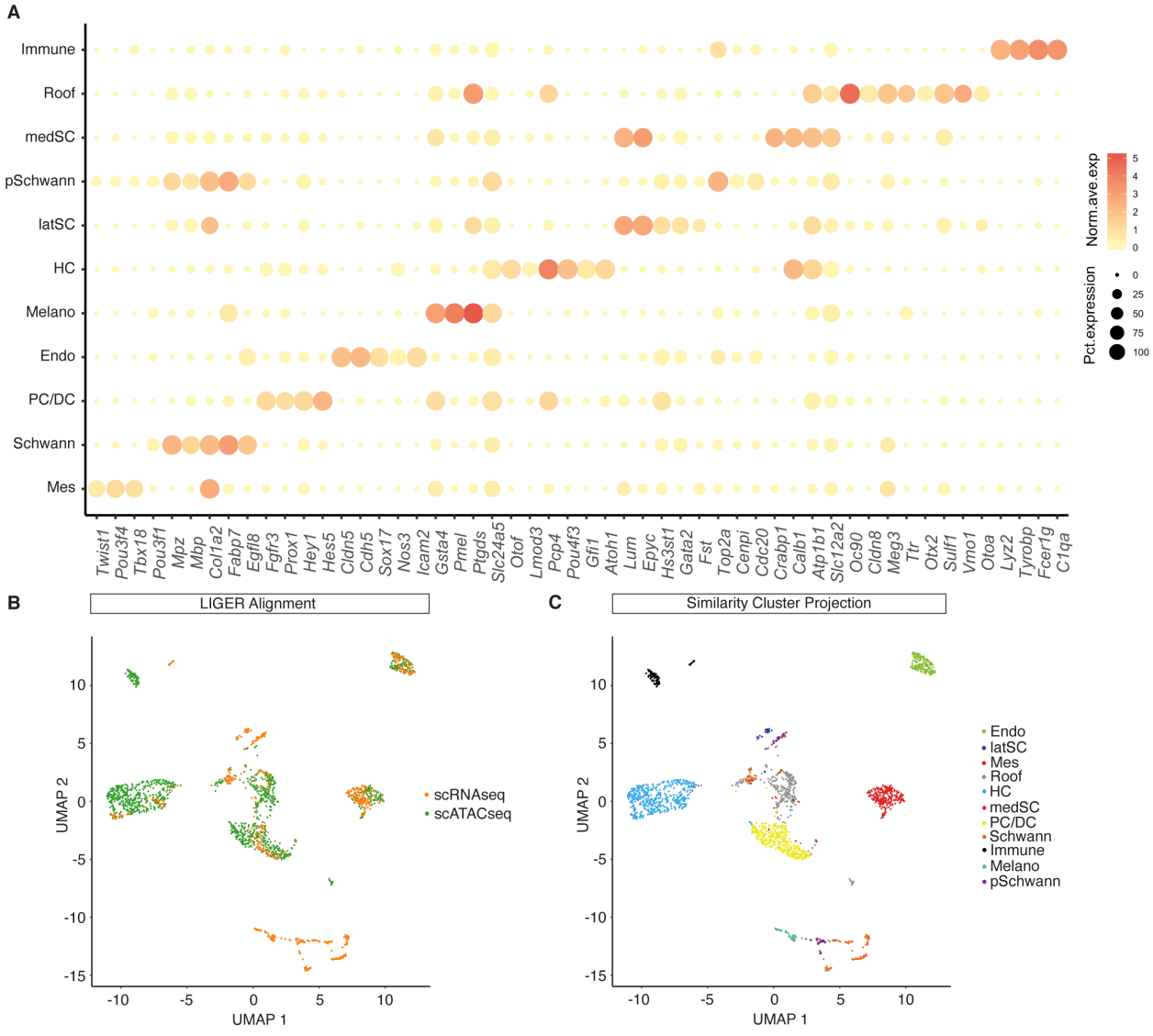

Figure 3.4 scRNA-seq cell type identification and representation of previously published organ of Corti marker genes. (A) Dot plot of candidate gene expression levels for each scRNA-seq cluster. The dot size represents the percentage of cells expressing a given transcript

for the clusters. (B) UMAP plot of LIGER single-cell multi-omics integration analysis, color coded by dataset modality. (C) UMAP plot of LIGER alignment color coded by cell identity from the Jaccard index similarity approach.

Peaks were accumulated and normalized by fragments pileup per million reads for better comparison. *Pou4f3* is a known HC specific marker gene (Xiang et al. 1997) and called peaks at the *Pou4f3* locus resolved accessible chromatin in HCs, while chromatin in PC/DCs and the other cell types was found in a closed conformation at the same locus. Similarly, the *Pou4f3* transcript was only detected in the HC population. *Hes5*, on the other hand, is a known cochlear PC/DC marker gene (Hartman et al. 2009), and exhibited cell type specific chromatin accessibility accompanied by PC/DC-specific expression of the transcript. *Cldn8*, *Tbx18*, *Cldn5*, and *C1qa* exhibit complementary chromatin accessibilities and transcript expression levels that are known to delineate roof, mesenchymal, endothelial, and immune populations, respectively.

3.3.3 Inference of TF activity in maturating HCs and SCs

HCs and PC/DCs of the organ of Corti develop from a shared progenitor starting around embryonic day 14.5 (E14.5) (Chen et al. 2002). We aimed to identify TFs controlling differentiation of the two cell types and to infer their function in a combinatorial approach from postnatal data. The function of a TF is highly context-dependent, nevertheless, it can generally be categorized as a transcriptional activator or repressor. We adopted two assumptions that were previously developed (Berest et al. 2019) to classify TF activity: 1) upon binding of an activating TF, chromatin accessibility at the regulatory element is increased resulting in an upregulation of the respective target gene transcript, and 2) conversely, binding of a repressing TF decreases average chromatin accessibility at the regulatory element and downregulation of the target gene will occur. Based on the assumptions, we established a classification model tailored toward single-cell experiment workflow.

First, by comparing scRNA-seq data from HC and PC/DC populations we identified 93 differentially expressed genes (*P*-adjusted < 0.05) encoding TFs such as Lhx3, Gfi1, Sox2, and Tgif1 (**Figure *3.5*A**). Next, we calculated TF motif accessibility *z*-scores using chromVAR (Schep et al. 2017). Briefly, the algorithm quantifies normalized motif accessibility with a *z*-score, by aggregating accessible regions per given TF motif across the whole genome of a single-cell. Using TF motifs as features, we visualized clusters in UMAP (**Figure *3.5*B**), which faithfully reproduced populations previously identified by SnapATAC. When HC and PC/DC clusters were compared, we identified 353 differentially accessible TF motifs (*P*-adjusted < 0.05) (**Figure *3.5*C**). To infer activating or repressing mode of action, we plotted mRNA fold change versus *z*-score fold change for the TFs investigated (**Figure *3.5*D**). Activating TF function, resulting in chromatin opening upon binding, was inferred if a given TF was differentially expressed in one of the two populations and the corresponding motif was significantly accessible in the same population. A repressor was classified based on its differential expression in combination with a negatively correlated *z*-score, indicating chromatin closure upon binding. Comparing HC and PC/DC populations, we identified 56 activators and 23 repressors. To assess the classification performance, we adopted previously published diffTF algorithm (Berest et al. 2019) and compared the overlap between the two methods. To perform the diffTF analysis, pseudo-bulk samples corresponding to 4 biological replicates were generated by aggregating scRNA-seq and scATAC-seq data from HC and PC/DC clusters, respectively. Using diffTF, we identified 36 activators and 10 repressors. Overall, we found 72% of the diffTF classifications were identical to the current approach. Next, we visualized expression levels and chromatin accessibility for four different HC and PC/DC activators and repressors. Transcription factor LHX3 was classified as a transcriptional activator in HCs (**Figure *3.5*D-E**) and previously

reported differential expression in HCs (Hertzano et al. 2007) was recapitulated, accompanied by differential motif accessibility in HCs as well. In addition, we used HINT-ATAC algorithm (Li et al. 2019a) to generate a footprint from cluster-aggregated scATAC-seq data using HOCOMOCO v10 database (Kulakovskiy et al. 2013), which showed increased chromatin accessibility adjacent to the LHX3 binding site in HCs compared to PC/DCs. Together these findings support the role of LHX3 as a transcriptional activator in HCs. On the other hand, GFI1 (**Figure *3*.5D, F**) is a known zinc-finger transcriptional repressor in HCs (Wallis et al. 2003). Gfi1 transcripts were differentially expressed in HCs, however, the GFI1 *z*-score, supported by the footprint, indicated significantly lower motif accessibility in HCs compared to PC/DCs resulting in a repressor classification. Transcription factor SOX2 is critical for organ of Corti development (Kiernan et al. 2005), and was identified as a transcriptional activator in PC/DCs based on its positive correlation of mRNA expression and motif accessibility (**Figure *3*.5D, G**). Conversely, TGIF1 is a known transcriptional repressor (Shen and Walsh 2005)and was characterized by a negative correlation between mRNA expression level and *z*-score in developing PC/DCs (**Figure *3*.5D, H**). To evaluate the quality of the curated HOCOMOCO v10 motifs, we re-run HINT-ATAC algorithm using the JASPAR 2020 database (Fornes et al. 2020) and obtained virtually identical footprints.

In summary, we classified 23 TFs regulating HC development subdivided into 6 activators and 17 repressors. With respect to PC/DCs, we identified 56 TFs segregating into 50 activators and 6 repressors.

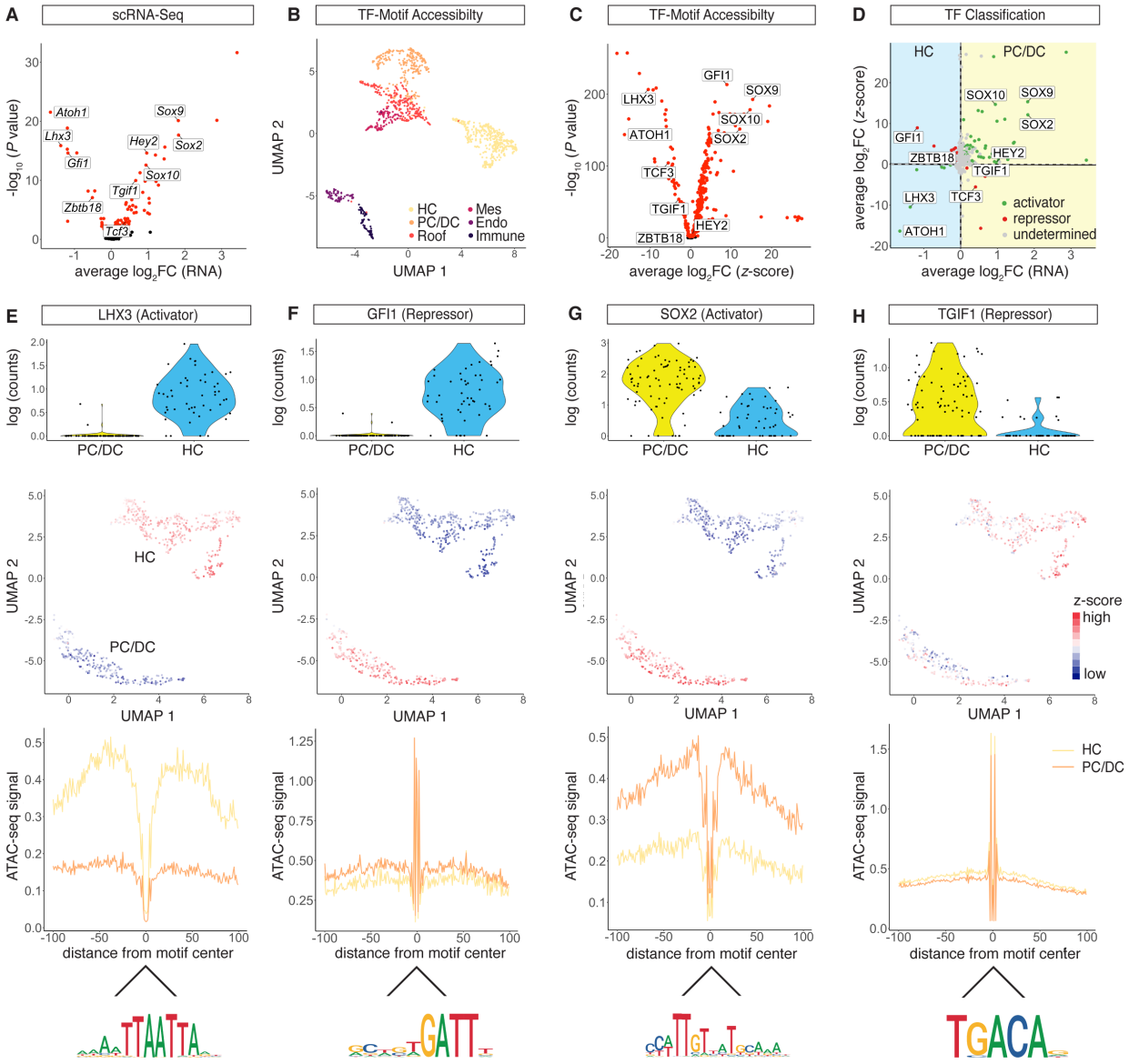

Figure 3.5 Transcriptional activator and repressor classification. (A) Volcano plot of differentially expressed TF genes between HC and PC/DC clusters (*P*-adjusted < 0.05). (B) UMAP of TF motif accessibility z-scores calculated from chromVAR. Cells are color coded based on SnapATAC clusters. (C) Volcano plot of differential TF motif accessibilities calculated from *z*-scores between HC and PC/DC clusters (*P*-adjusted < 0.05). (D) Dotplot of TF classification shown in average log2 fold change (FC) mRNA level and *z*-scores. Differential expression from scRNA-seq between HCs and PC/DCs is plotted on the *x*-axis, while differential accessibility from scATAC-seq is shown on the *y*-axis. Activators are classified in green, repressors in red, and undetermined TFs in gray. (E-H) TF activities in differentiating HCs and PC/DCs in terms of mRNA expression, chromatin accessibility, and footprints. (E) LHX3, a transcriptional activator in HCs. Top row: Violin plot of RNA expression. Each dot represents a single cell. Second row: UMAP plot of LHX3 motif accessibility calculated as *z*-score. Red indicates higher accessibility compared to blue. Each dot represents a single cell. Third row: LHX3 footprint calculated from scATAC-seq data using HINT-ATAC. Activators are

characterized by high scATAC-seq signal in the flanking region of the TF binding sites compared to the control population. Yellow line represents the HC cluster, and orange line represents the PC/DC cluster. Bottom row: mouse HOCOMOCO v10 consensus sequence for the LHX3 motif. (F-H) Analogous data representation for (F) GFI1, classified as a HC repressor, (G) SOX2, a PC/DC activator and (H) TGIF1, a repressor in PC/DCs.

3.3.4 TFs controlling HC and SC differentiation

TFs shape the epigenetic landscape of a given cell and direct differentiation through tight transcriptional control of downstream target genes, commonly summarized as regulons. We predicted TF-specific regulons at the whole transcriptome level by leveraging scRNA-seq and scATAC-seq datasets. First, co-expression modules of previously classified TFs and their respective downstream targets were identified by analyzing the scRNA-seq data using GENIE3 (Huynh-Thu et al. 2010). To determine activator regulons, we filtered for positively correlated target genes, while repressor regulons were constituted from negatively correlated target genes only.

At this point, the list of correlated genes included potential direct as well as indirect target genes of the respective TFs. Next, we screened the loci of potential target genes for accessible TF binding sites using FIMO (Grant, Bailey and Noble 2011). Links lacking TF-binding sites in accessible peaks were considered indirect targets and got removed from the regulon. Once TF-specific regulons were identified, a regulon enrichment score was calculated for each cell using AUCell (Aibar et al. 2017). Overall, regulon activities were visualized for 70 TFs previously categorized as transcriptional activators and repressors (**Figure *3.6*A**).

Given the lengthy experimental procedure, we aimed to exclude a potential bias of the AUC enrichment matrix toward stress-related regulons. We screened for TFs that were associated with the Gene Ontology term “Stress Response” (GO:0006950) and identified 25 TFs. However, 22 out of the 25 stress-associated genes, like Ils1 (Radde-Gallwitz et al. 2004) and

Gata3 (Luo et al. 2013), were previously cited in the context of organ of Corti development as well (**Table *3.1***). The remaining three genes, namely *Atf3* (Maeda et al. 2020), *Hif1a* (Chung et al. 2004) and *Zbtb7a* (Yang et al. 2015), were previously published to be differentially expressed after noise exposure and may change their expression in response to the dissection procedure.

GENE SYMBOL	DEVELOPMENT RELEVANCE	LITERATURE REFERENCE
Stat5b	IGF signaling	(Hertzano et al. 2007)
Rbpj	Notch signaling mediator	(Basch et al. 2011)
Sox4	SOXC TF	(Gnedeva and Hudspeth 2015)
Bach1	TGFβ signaling in SCs	(Cheng et al. 2019)
Nfatc4	Apoptosis; damage independent expression	(Zhang et al. 2019)
Irf3	Constitutively expressed immune gene	(Cai et al. 2014)
Srebf2	TGFβ signaling in SCs	(Cheng et al. 2019)
Hmga2	Stemness	(Golden, Benito-Gonzalez and Doetzlhofer 2015)
Klf4	Yamanaka factor	(Lopez-Juarez et al. 2019)
Atf3	**Expression in response to noise**	(Maeda et al. 2020)
Esr1	Estrogen signaling	(Simonoska et al. 2009)
Etv5	FGF signaling	(Ebeid and Huh 2020)
Isl1	Prosensory development	(Radde-Gallwitz et al. 2004)
Hey2	FGF signaling	(Doetzlhofer et al. 2009)

Nr4a3	SC development	(Maass et al. 2016)
Gata3	Prosensory development	(Luo et al. 2013)
Rora	SC development	(Maass et al. 2016)
Jun	SC development	(Sanz et al. 1999)
Hif1a	**Expression in response to noise**	(Chung et al. 2004)
Tcf7l2	WNT signaling	(Huang et al. 2011)
Rest	Development	(Wilkerson et al. 2019a)
Rel	SC development	(Scheffer et al. 2015)
Zbtb7a	**Expression in response to noise**	(Yang et al. 2015)
Arntl	Embryonic development	(Perl, Shamir and Avraham 2018)
Mtf1	GATA3 target	(Alvarado et al. 2009)

Table 3.1 List of known developmental genes of the organ of Corti.

To validate the performance of the developed approach, we compared the SOX2-regulon with previously published SOX2 ChIP-seq data from an inner ear cell line (Kwan, Shen and Corey 2015). 68% and 29% of the SOX2-regulon associated genes were present in two independently performed ChIP-seq experiments.

Hierarchical clustering of the AUC enrichment matrix resolved HC and PC/DC clusters (**Figure *3.6*A**) and GO term analysis of cluster specific regulons revealed terms such as auditory receptor differentiation in HCs and positive regulation of cell proliferation in PC/DCs. Clustering also revealed the relations between different TFs with respect to their regulons. The regulons of transcriptional activator SOX9 and repressor GFI1 were closely related with an overlap of 71 target genes (**Figure *3.6*B**). All 71 overlapping genes were confirmed to be differentially

expressed in the PC/DC cluster, and thus represented a portion of the PC/DC specific transcriptome to be repressed in *Gfi1*-positive hair cells. For further analysis, we focused on *S100b* and *Sox9* genes, which were differentially expressed in PC/DCs and among the shared targets between SOX9 and GFI1 regulons (**Figure *3.6*B-D**). Using Cicero (Pliner et al. 2018) the *cis*-regulatory landscape of *Sox9* in the PC/DC cluster was reconstructed, and motif scanning identified accessible SOX9 binding sites in the predicted *Sox9* regulatory elements, suggesting autoregulation (**Figure *3.6*E**). SOX9 motifs were also found in the regulatory elements of *S100b* (**Figure *3.6*F**). In absence of the repressor GFI1 in PC/DCs, GFI1 motifs in the regulatory elements of *S100b* and *Sox9* were accessible. Conversely, expression of Gfi1 in HCs rendered its binding sites and flanking regions inaccessible to prevent the expression of the PC/DC specific genes in HCs. Similarly, regulatory elements containing SOX9 motifs were not accessible in HCs.

As the AUC enrichment matrix successfully resolved TFs contributing to the regulatory landscape of HC and PC/DC differentiation, the matrix was used as a discovery tool. The clustering allowed categorization of TFs in groups controlling a similar set of target genes. *Nhlh1*, for example, was previously identified in an RNA-based screening to be expressed in developing HCs (Scheffer et al. 2015). The functional context of transcription factor NHLH1 was not investigated. However, the NHLH1 regulon was closely related to the ATOH1 regulon with an overlap of 665 target genes (**Figure *3.6*A, G**), suggesting synergistic effects in early HC differentiation. Conversely, the ZBTB18 regulon clustered further away from ATOH1 regulon and more similar to the LHX3 regulon, which is expressed later during HC development (Hertzano et al. 2007) (**Figure *3.6*A**). ATOH1 and NHLH1 TF binding sites at the *Zbtb18* TSS indicate that the gene is a shared target (**Figure *3.6*H**). Protein expression of ZBTB18 was

confirmed (**Figure *3.6*I**) and regulon associated genes such as *Cdh23*, *Cib2*, *Espn*, *Myo7a*, *Pcdh15*, *Tmie*, *Ush2a*, and *Whrn* (Fettiplace 2017), among others, suggest a role for *Zbtb18* in hair bundle formation. In summary, the AUC enrichment matrix was employed to visualize regulon activities for 16 HC- and 54 PC/DC-associated TFs at single-cell resolution.

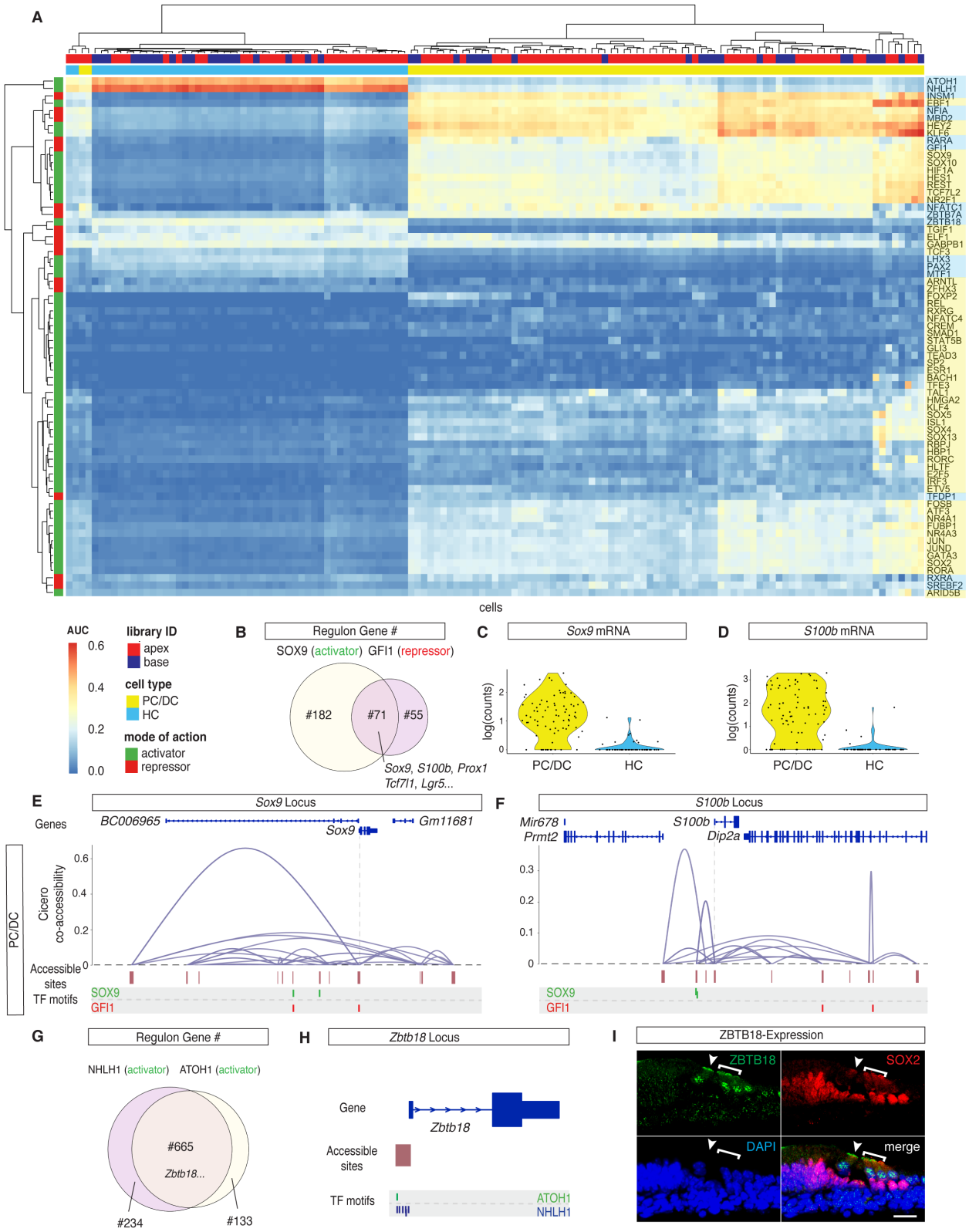

Figure 3.6 TFs controlling HC and PC/DC differentiation. (A) AUC enrichment matrix with hierarchical clustering at single-cell resolution revealed the regulon activities during

differentiation of HCs and PC/DCs. A regulon summarizes putative downstream target genes as a group of the respective TF. The activity of the regulon is color coded from blue (depletion) to red (enrichment). Hierarchical clustering reveals similarities between individual cells (*x*-axis) as well as between different regulons (*y*-axis). Color bars on the top and to the side of the heatmap indicate library ID, cell type, mode of action, and cell type specificity. (B) Venn diagram of the number of overlapped downstream target genes between SOX9 regulon and GFI1 regulon. (C-D) Violin plots of *Sox9* (C) and *S100b* (D) expression level. The two genes are representatives of overlapping downstream target genes between SOX9 and GFI1 regulons. (E-F) Coaccessibility analysis of *Sox9* and *S100b* loci in the PC/DC cluster using Cicero. (E) In PC/DCs, *Sox9* TSS is directly and indirectly connected to the accessible sites. They correspond to predicted regulatory elements that contain putative TF binding sites for SOX9 and GFI1 as determined by FIMO motif scanning. Top row: Genome annotation from UCSC Known Genes. Second row: Coaccessibility plot connects predicted regulatory elements with the TSS. Third row: Accessible regions aligned with the locus. Fourth row: putative TF binding sites of SOX9 and GFI1 motifs relative to the accessible regions. TSS position is indicated with a dashed line. (F) Analogous data representation for the *S100b* locus. (G) Overlapping downstream target genes between known HC transcriptional activator ATOH1 and NHLH1. (H) *Zbtb18* is a shared target gene between ATOH1 and NHLH1 regulons with accessible TF binding sites for both TFs at the TSS in HCs. (I) Immunostaining of ZBTB18 protein expression in IHCs and OHCs in cryosections of the organ of Corti (P2). Arrowhead pointing at the IHC. Bracket delineates OHC-location. Scale bar: 20μm.

3.3.5 Spatial reconstruction of HCs from scATAC-seq and scRNA-seq data

Organ of Corti development proceeds in gradients, where cells located in the base of the organ are more mature compared to the cells in the apex (Chen et al. 2002, Lee et al. 2006b). To further analyze effects of differentiation on the regulatory landscape of HCs, we aimed to reconstruct individual HC's anatomical position from scRNA-seq and scATAC-seq data. We followed the conceptual idea previously published for reconstruction of the mouse organ of Corti from single-cell qPCR data (Waldhaus et al. 2015). During the process of dissection (**Figure *3.7*A**), flow sorting (**Figure *3.7*B**), and library preparation, the apical and basal compartments of the organ of Corti were processed separately in both scRNA-seq and scATAC-seq experiments (**Figure *3.7*C-D**). In total, 427 DEGs (*P*-value < 0.005) (**Figure *3.7*E**) and 147 DARs (*P*-value < 0.001) (**Figure *3.7*F**) between apical and basal compartments were identified.

Using the DEGs and DARs as features, we were able to project the HCs in a 1-dimensional PCA along the *y*-axis (**Figure *3.7*G-H**). The distribution along the *x*-axis reflects random jitter for better visualization. HCs were plotted according to their rank order, which resolved the relative position of each individual cell along the apex-to-base axis for both, scRNA-seq and scATAC-seq data. For validation of the spatial reconstruction, library IDs were plotted onto the 1D spatial reconstruction maps. *Pkhd1l1* was among the DEGs and annotated DARs with expression and accessibility gradients predicted to be significantly higher in basal HCs compared to the apical counterparts. Graded expression of *Pkhd1l1* transcript was previously reported (Wu et al. 2019), and reproduced by RNA-staining (**Figure *3.7*I-J**)

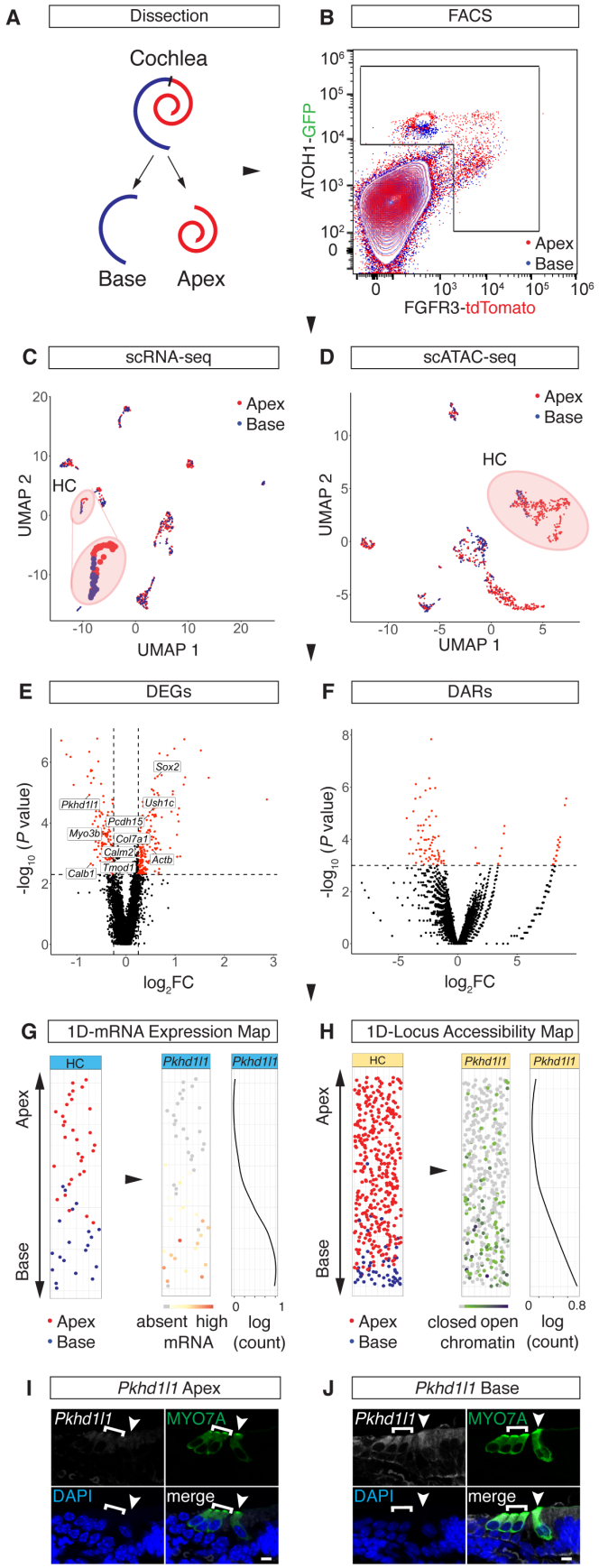
A
Dissection
Cochlea
Base
Apex
B
FACS
ATOH1-GFP
FGFR3-tdTomato
Apex
Base
C
scRNA-seq
UMAP 1
UMAP 2
HC
D
scATAC-seq
E
DEGs
-log10 (P value)
log2FC
Sox2
Pkhd1l1
Ush1c
Pcdh15
Myo3b
Col7a1
Calm2
Actb
Tmod1
Calb1
F
DARs
G
1D-mRNA Expression Map
absent high mRNA
log (count)
H
1D-Locus Accessibility Map
closed open chromatin
I
Pkhd1l1 Apex
MYO7A
DAPI
merge
J
Pkhd1l1 Base

Figure 3.7 Spatial reconstruction of HC origins along the longitudinal axis. (A) Schematic representation of the sampling strategy used in this study. Color code: apex-red, base-blue. (B) FACS plot and gating strategy to isolate GFP- and tdTomato-expressing cells. Color code identifies compartmental identities (color code same as in A). (C-D) UMAP projections of all cells analyzed in the scRNA-seq (C) and scATAC-seq (D) experiments with color code for library ID (color code as in A and B). HC populations are highlighted with a circle and magnified for better visibility in (C). Dots correspond to single cells. (E-F) Volcano plots of DEGs (E) and DARs (F) comparing apical and basal compartments. scRNA-seq cutoff: $P < 0.005$ and absolute value of log2FC greater than 0.25. scATAC-seq cut off: $P < 0.001$. (G-H) 1D spatial reconstruction of single-cell transcript expression levels and chromatin accessibilities. (G) 1D HC expression map. Left column: 1D PCA based on the DEGs shown in (E). *Y*-axis resolves predicted apex (top) to base (bottom) axis. Data points are randomly spread along *x*-axis for better visibility. Dots correspond to single cells. Color code depicts library ID (same as in A-D). Middle column: Gene expression level of *Pkhd1l1* projected onto the 1D expression map. Right column: *Pkhd1l1* expression fitted into a regression line. *Y*-axis corresponds to the apex-to-base axis, *x*-axis to expression level shown in log counts. (H) Analogous data representation as in G, showing 1D accessibility map with library ID and *Pkhd1l1* accessibility projected. (I-J) RNAScope staining of *Pkhd1l1* transcript comparing HCs of apical (I) and basal (J) origin. HCs were counter stained with Anti-MYO7A and DAPI nuclear stain. IHC (arrowhead) and OHCs (bracket) staining using identical imaging settings. Scale bar: 10µm.

3.3.6 Chromatin dynamics during HC differentiation

Around birth, segregation into IHCs and OHCs is distinct, based on anatomical position and differential gene expression (Kolla et al. 2020). IHC and OHC subclusters, with respect to the scRNA-seq data, were identified based on a set of previously published marker genes (Waldhaus et al. 2015) (**Figure *3.8*A**). Differential gene expression analysis revealed 169 IHC- and 115 OHC-specific genes ($P < 0.01$) (**Figure *3.8*B**). Plotting cluster ID, library ID, and DEGs like *Fgf8* and *Cdh1* onto the 1D spatial expression map allowed for visualization of cell type specific transcriptomes spanning the longitudinal axis of the developing organ of Corti (**Figure *3.8*C**). However, at the chromatin level further sub-clustering using *z*-scores appeared to be driven by original position along the apex-to-base axis rather than IHC and OHC identities. To visualize this observation we projected DAR-based rank order, library ID and *z*-scores of OHC specific TF INSM1 (Wiwatpanit et al. 2018) onto the UMAP (**Figure *3.8*D**). To test if IHC- and OHC-specific chromatin remodeling occurs along the tonotopic axis around birth, we

reconstructed a HC-specific trajectory based on *z*-scores (**Figure *3.8*E**). Using CellTrails (Ellwanger et al. 2018), single HCs were aligned on a Y-shaped trajectory representing 4 individual states. To validate the trajectory prediction, Slingshot (Street et al. 2018) and Monocle (Trapnell et al. 2014, Qiu et al. 2017a, Qiu et al. 2017b) were used. Projecting DAR-based rank order onto the CellTrails map (**Figure *3.8*F**) resolved apical identity for state S4, which corresponded to the smaller of the two subclusters seen in the UMAP projection (**Figure *3.8*D**). Basal rank order identities related to states S2 and S3. Similarly, library IDs were distributed asymmetrically along the trajectory. States S1 and S4 were constituted by cells dissected from the apex only, while S2 and S3 contained both, apical and basal HCs. Given the gradual differentiation along the apex-to-base axis, we hypothesized that S4 may correspond to an apical, immature HC state, and that S2 and S3 may represent more mature IHC and OHC states at the base. To test this hypothesis, we first visualized differential *Atoh1* mRNA expression increasing from the base toward the apex (**Figure *3.8*G**). Next, differential *z*-scores between the 4 states were determined in pairwise comparisons using Wilcoxon sum rank tests. In support of the hypothesis that states S4 corresponds to the apical end of the organ of Corti, we found that both the ATOH1 *z*-score and the footprint were significantly more accessible in state S4 compared to S2 and S3. To further validate our hypothesis that S2 and S3 may correspond to basal IHCs and OHCs, we focused on TF INSM1, a transcriptional repressor expressed in OHCs (Wiwatpanit et al. 2018) (**Figure *3.8*H**). Differential expression of *Insm1* mRNA was confirmed and consistent with its repressive function, state S3 exhibited lower *z*-scores compared to S2 and the footprint was less accessible in state S3 compared to S2 as well. Together, these findings imply OHC identity for cells representing state S3. Aiming to test if state S2 represented IHCs, we visualized IHC marker *Hivep2* mRNA levels and motif accessibility (**Figure *3.8*I**). Although the function

of HIVEP2 in HC development remains to be determined, differential expression has been reported for IHCs and OHCs (Li et al. 2016). The current study confirms the differential mRNA expression in IHCs and that the HIVEP2 motif was significantly more accessible in state S2 compared to S3. These findings suggested HIVEP2 may function as a transcriptional activator in IHCs. In summary, the data presented support the hypothesis that state S4 represented apical immature HCs while S2 and S3 corresponded to IHCs and OHCs, respectively.

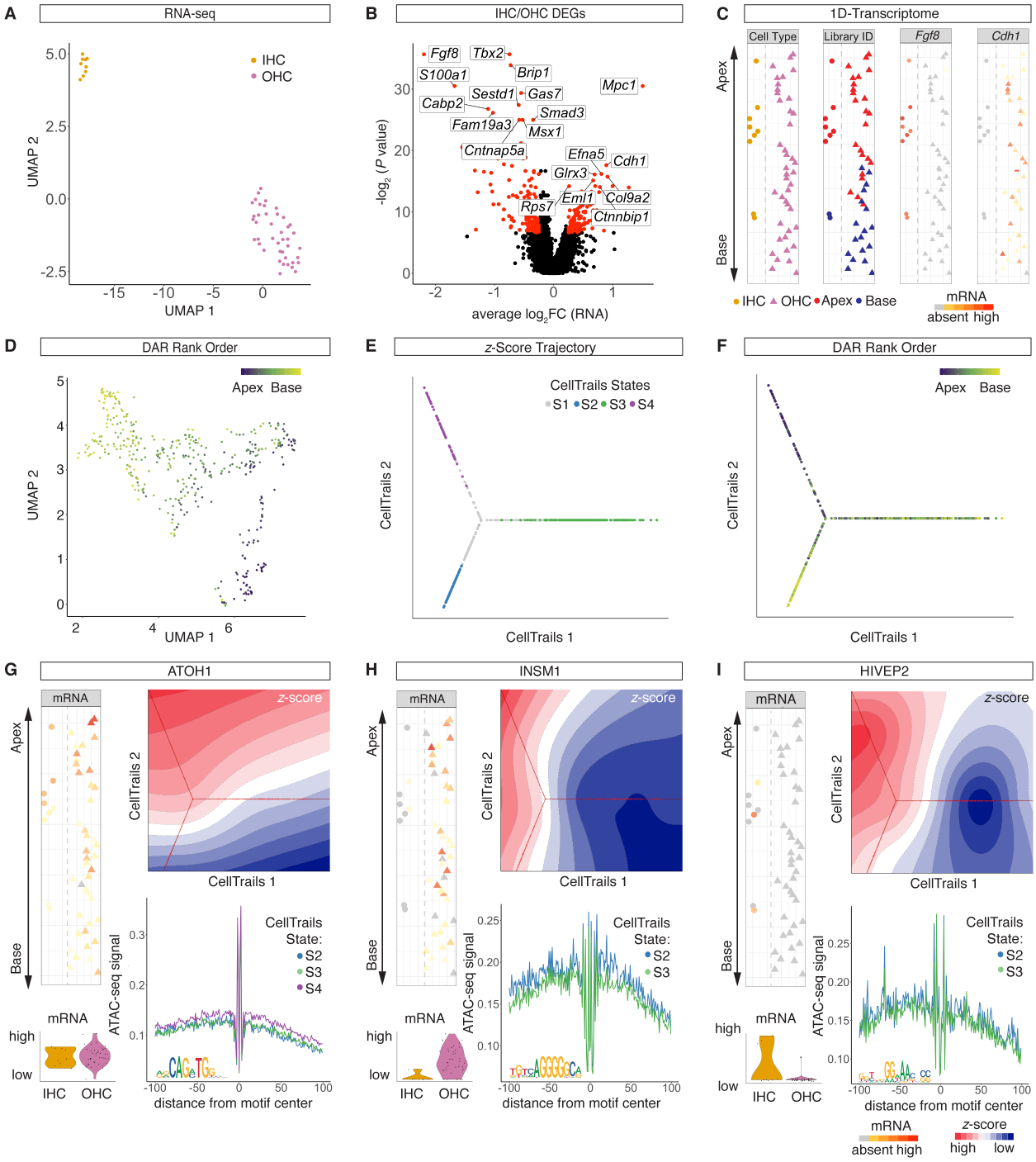

Figure 3.8 Developmental bifurcation of IHCs and OHCs. (A) UMAP projection of scRNA-seq HCs delineates IHCs and OHCs subclusters. Single dot represents a single cell. (B) Volcano plot of DEGs ($P < 0.01$) between IHC and OHC clusters. (C) 1D spatial reconstruction map with cell identity (first column) and library ID (second column) projected. Expression levels of IHC-specific gene *Fgf8* (third column), and OHC-specific gene *Cdh1* (fourth column) were projected onto the 1D spatial reconstruction map. Dashed line delineates IHCs (left) from OHCs (right). (D) UMAP plot of HC cluster from scATAC-seq data with projection of spatial rank order as

determined by 1D spatial reconstruction map. (E-F) Trajectory reconstruction based on scATAC-seq *z*-scores using CellTrails. (E) CellTrails states, and (F) DAR-based rank order projected onto the trajectory. (G-I) Comparative analysis of selected TFs in terms of mRNA expression, motif accessibility, and footprints. (G) Top left column: *Atoh1* mRNA expression projected onto the 1D spatial reconstruction map. Dashed line delineates IHCs (left) from OHCs (right). Bottom left column: violin plots with mRNA levels for IHCs and OHCs. Top right column: Contour plot of ATOH1 *z*-scores with CellTrails trajectory in the background. Bottom right column: ATOH1 footprint from scATAC-seq data for selected CellTrails states (same color code as in Fig 5E). ATOH1 consensus sequence is depicted at the bottom left of the footprint plot. (H-I) Analogous data representation for (H) INSM1 and (I) HIVEP2.

3.3.7 TFs controlling IHC and OHC differentiation

Utilizing the AUC enrichment matrix, we aimed to identify novel IHC- and OHC-specific TFs in order to add to our knowledge of the regulatory landscape during HC maturation. A total of 7 differentially expressed TFs (*P*-adjusted < 0.05) were identified (**Figure *3.9*A**). Given the small number of IHCs identified from the scRNA-seq data, we confirmed robustness of the 7 TFs identified by comparison with previously published bulk RNA-seq data from perinatal and adult IHCs and OHCs (Li et al. 2018, Wiwatpanit et al. 2018). Next, 254 differential *z*-scores (*P*-adjusted < 0.05) were calculated (**Figure *3.9*B**) from scATAC-seq data. Correlation of expression level with motif accessibility correctly annotated INSM1 as an OHC repressor and HIVEP2 as an IHC activator (**Figure *3.9*C**). In addition, one OHC activator (TCF4) and 2 IHC activators (FOXO4 and GLIS3) were categorized and visualized in the AUC enrichment matrix (**Figure *3.9*D**). Projecting mRNA levels and *z*-scores of OHC-activator TCF4 revealed differential expression between IHCs and OHCs, and a major gradient in TCF4 motif accessibility was observed along the apex-to-base axis (**Figure *3.9*E**). TCF4-antibody staining revealed qualitative differences, in the nucleus as well as the cytoplasm, between IHCs and OHCs (**Figure *3.9*F**). *Foxo4* mRNA was differentially expressed in IHCs, and FOXO4 motif was differentially accessible in state S2 compared to S3 (**Figure *3.9*G**). FOXO4-antibody staining revealed the presence of FOXO4 in the nucleus and the cytoplasm of IHCs and OHCs

(**Figure *3.9*H**). *Glis3* mRNA was differentially expressed in IHCs and GLIS3 motif was differentially accessible in state S2 compared to the OHC state S3 (**Figure *3.9*I**). Nuclear staining was present in IHCs with GLIS3-antibody (**Figure *3.9*J**). Together these findings reveal dynamic changes in the regulatory landscape of IHCs and OHCs along the apex-to-base axis.

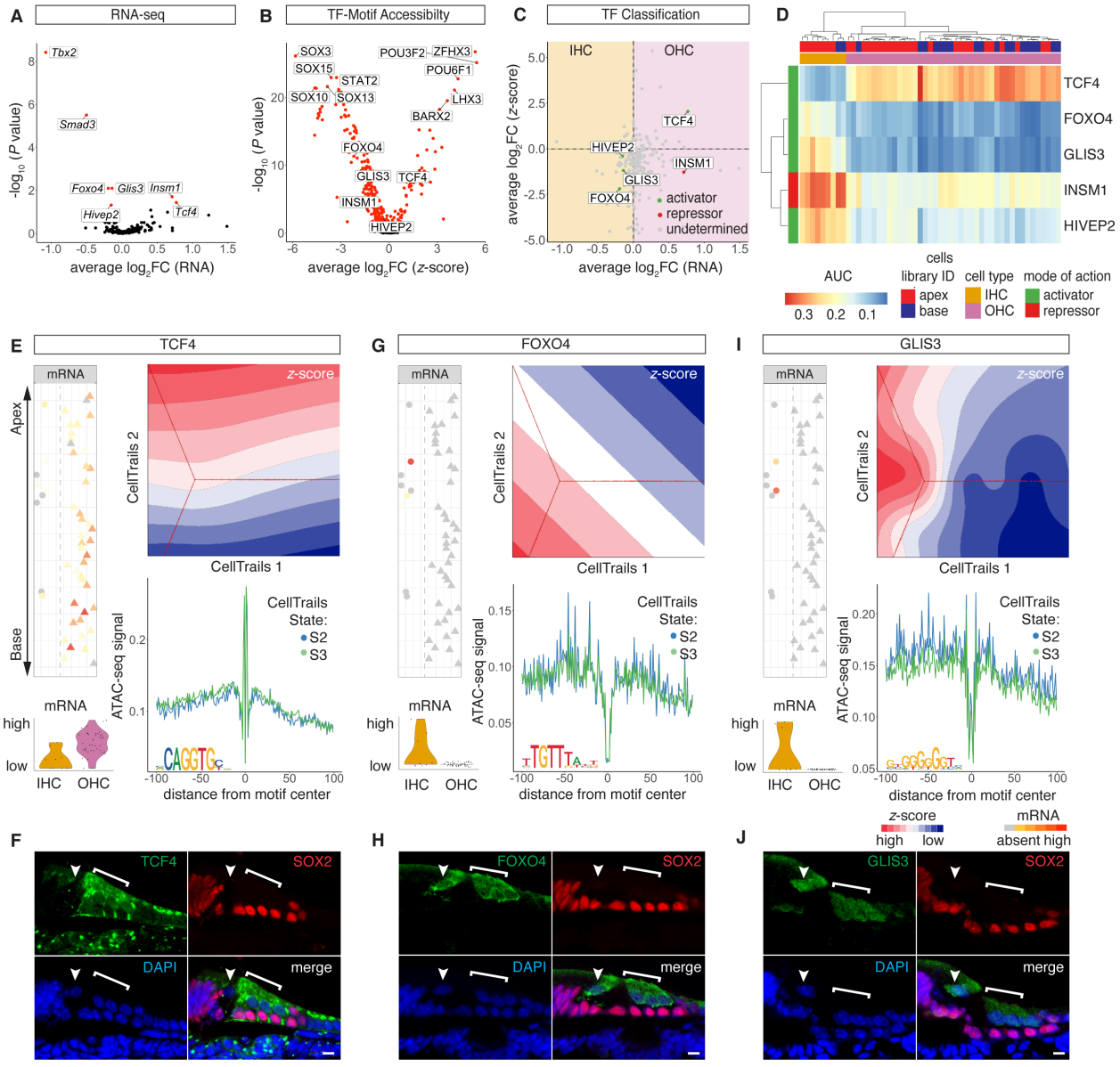

Figure 3.9 TFs controlling IHC and OHC differentiation. (A) Volcano plot of differentially expressed TF genes (*P*-adjusted < 0.05) between IHCs and OHCs. (B) Volcano plot of differentially accessible TF motifs (*P*-adjusted < 0.05) comparing IHC and OHC cluster. (C) Dot plot of TF classification shown in average log2FC mRNA transcripts and *z*-scores. Differential expression between IHCs and OHCs is plotted on the *x*-axis, while differential accessibility is

shown on the *y*-axis. Activators are classified in green, repressors in red, and undetermined TFs in gray. (D) AUC enrichment matrix of TF regulons contributing to IHC/OHC segregation. Color bars on the top and to the side of the heatmap indicate library ID, cell type as determined based on DEGs, and mode of action. (E,G,I) Comparative analysis of selected TFs in terms of mRNA expression, motif accessibility, and footprints. Analogous data representation as in Fig. 5F-G. (E) OHC activator TCF4. (F) Anti-TCF4 staining localizes to OHC nuclei and cytoplasm. HCs are counter stained with Anti-MYO7A and DAPI nuclear stain. Arrowhead points at IHC nucleus, bracket highlights OHC region. Scale bar: 10 μm. (G) IHC activator FOXO4. (F) Anti-FOXO4 staining in IHC and OHC cytoplasm and nuclei. Counter stain, scale bar, and labeling analogous to F. (I) IHC activator GLIS3. (J) Anti-GLIS3 in IHC and OHC cytoplasm and nuclei. Counter stain, scale bar, and labeling analogous to F.

3.4 Discussion

Current single-cell-based RNA-seq and ATAC-seq protocols resolve thousands of genes and accessible chromatin regions per individual cell. This is in stark contrast to many classic developmental tool sets focusing on gene expression and regulatory networks such as ChIP-seq, knock out, or over expression studies, resolving one candidate gene at a time. The amount of data generated using novel sequencing protocols provides information at steadily increasing resolution. Therefore, there is a need for novel data analysis strategies to provide a biological context for the accumulating information. The AUC enrichment matrix presented in this study identified 20 regulons contributing to the differentiation of sensory HCs. Previous whole transcriptome-based studies (Burns et al. 2015) resolved each of the 20 TFs to be expressed in the developing organ of Corti as well. However, based on previous study design their roles in inner ear development remained elusive. Here we present an integrative approach, combining scRNA-seq and scATAC-seq technology, to compare cell types that develop from shared progenitors. Analyzing differentially expressed TFs that showed differential motif accessibility allows us to robustly resolve how multiple TFs function in concert to activate or repress cell type specific target genes at the whole transcriptome level. The organ of Corti was utilized as a model

due to its developmental gradient along the longitudinal axis. The same analytical framework can be applied to other organ systems, where cells analyzed share a common progenitor.

The scRNA-seq and scATAC-seq data were generated from age-matched, genetically labeled HCs and PC/DCs of the organ of Corti. In order to integrate both datasets, an AUC enrichment matrix was computed in a sequential workflow. We leveraged existing algorithms and developed novel elements to study HC and PC/DC differentiation and started by predicting activating and repressing function of differentially expressed TF genes. Existing algorithms like diffTF (Berest et al. 2019) were developed for bulk-based experiments comparing two groups with multiple biological replicates using Pearson's correlation analysis. We tested this approach with pseudo bulk samples from single-cell data and identified a number of activator and repressor TFs in each cell type. However, diffTF failed to classify key TFs previously described for inner ear development, likely due to the limitations of cell numbers and sample numbers. To overcome this challenge, we adopted the hypothesis that upon binding of an activator the flanking regions of the TF binding sites would open and conversely binding of a repressor would decrease the average accessibility at the regulatory elements controlled by the TF. Therefore, we compared fold changes in TF expression levels with TF motif accessibility. This approach successfully identified known TF activators and repressors, like LHX3 and GFI1, with remarkable robustness and helped us classify 79 known and unknown TFs contributing to organ of Corti development. Although this classification algorithm virtually considers all TFs expressed in the scRNA-seq dataset, it is limited by the motif database used to calculate motif accessibilities using chromVAR. Specifically, previously published TFs like POU4F3 and IKZF2 (Xiang et al. 1997, Chessum et al. 2018) were not annotated in the mouse HOCOMOCO v10 database and therefore not considered in this study.

To calculate the AUC enrichment matrix, general concepts from the SCENIC algorithm were adopted (Aibar et al. 2017), and we integrated information regarding TF classification and motif accessibility from the scATAC-seq experiment. First, a co-expression matrix was computed using GENIE3 (Huynh-Thu et al. 2010) considering both positively and negatively correlated TF-target gene links by integrating activator and repressor predictions, respectively. Next, indirect target genes were excluded by leveraging scATAC-seq data. Finally, the regulon activities for each single cell were calculated with AUCell and projected to the AUC heatmap. Integration of data from independently acquired scRNA-seq and scATAC-seq experiments robustly identified developmentally relevant activating and repressing TFs and provided insights into TF function by resolving direct target genes. This approach was not conceived to replace classic knock out and over expression experiments, but to provide an alternative approach accessing the whole regulatory network in a single experiment. For example, ChIP-seq experiments require considerably larger amounts of input material compared to the single-cell technology, explaining limited numbers of inner ear specific ChIP-seq data in the literature (Cai et al. 2015, Kwan et al. 2015, Stojanova, Kwan and Segil 2016, Li et al. 2020, Menendez et al. 2020b). Together, this illustrates why the current approach is specifically useful for populations with limited cell numbers, like IHCs in mice, where only about 800 cells exist per inner ear (Ehret and Frankenreiter 1977). Finally, the current approach may prove less sensitive compared to ChIP-seq technology, however, the overlap between both methods aiming to identify SOX2 target genes underlined its relevance in understanding gene regulation during organ of Corti differentiation.

The AUC enrichment matrix identified 20 TFs including regulons contributing to the differentiation of sensory HCs. Many of the TFs like ZBTB18 were known to cause

sensorineural hearing loss (SNHL) (Aleksiūnienė et al. 2017) but their role in inner ear development remained elusive. This is of particular interest, as a limited set of only 4 TFs, namely SIX1, ATOH1, POU4F3 and GFI1, is sufficient to convert fibroblasts into induced HC like cells (Menendez et al. 2020b). Together, these findings illustrate that a limited number of TFs play key roles in controlling the regulatory landscape of HC differentiation, nevertheless, a significantly larger array of TFs is necessary to allow for differentiation of functional HCs. Generally, after undergoing terminal mitosis, HCs develop in three overlapping phases. Initially, the regulatory landscape is represented by TFs, like ATOH1, LHX3, and GFI1 (Wallis et al. 2003, Woods et al. 2004, Hertzano et al. 2007), establishing an early HC fate by delineating HCs from PC/DCs. Later around birth, the developmental bifurcation into IHCs and OHCs is controlled by TFs like INSM1 and IKZF2 (Chessum et al. 2018, Wiwatpanit et al. 2018). In parallel, genes contributing to functions like mechanotransduction and synaptic transmission are up-regulated to complete the developmental progression (Fettiplace 2017). The 20 TFs identified contribute across the entire continuum of HC development. Comparing NHLH1- and ZBTB18-regulons, for example, allowed us to annotate their roles in initial differentiation and functional maturation, respectively. Likewise, comparing IHC with OHC regulatory landscapes, 5 differentially active TFs were identified. Among the 5 TFs, INSM1 was previously published to control OHC development supporting our findings. Except for HIVEP2, the remaining 4 TFs namely INSM1, FOXO4, TCF4 and GLIS3, were either directly or indirectly associated with SNHL (Hishiya et al. 2006, Dimitri et al. 2011, de Winter et al. 2016). While clustering of previously published marker transcripts allowed for IHC and OHC separation in scRNA-seq data, cellular identities were less prominent when analyzing scATAC-seq data. Based on the trajectory reconstruction, we were able to visualize differential motif accessibility for

transcription factors INSM1, FOXO4, TCF4, GLIS3, and HIVEP2 between basal IHCs and OHCs. The trajectories were used to visualize differences between transcriptome and chromatin-based identities of HCs during differentiation. Together, our findings support the observation that during development, dynamic changes of the chromatin accessibility landscape on average lag behind changes of the transcriptional landscape (Hu et al. 2018, Li et al. 2020).

In conclusion, this study provides a framework to analyze dynamic changes in the regulatory landscape of various cellular lineages that develop from a shared progenitor. With respect to the development of auditory HCs, we reconstructed a regulatory landscape featuring 20 individual TFs. Given the observation that several of those TFs have been linked to SNHL, the data provided by this study will help to further the knowledge regarding sensory HC differentiation and maturation in the mammalian inner ear.

3.5 Methods

3.5.1 Animal models

All animal maintenance and experimental procedures were performed in accordance with NIH guidelines and were approved by the Institute Animal Care and Use Committee at the University of Michigan (protocol: PRO00008096, JW).

All mice were maintained on a mixed genetic background. FGFR3-iCre (Young et al. 2010) were crossed with Ai14-tdTomato (Madisen et al. 2010) and ATOH1-GFP (Rose et al. 2009). In order to induce FGFR3-iCre activity, P0 pups were given intraperitoneal injections of tamoxifen (Sigma, T5648-1G) at 200 mg/kg, diluted in corn oil (Sigma, C8267). Cochlear samples were isolated at P2 from FGFR3-iCre;Ai14-tdTomato;ATOH1-GFP-mice.

3.5.2 Single cell isolation and flow sorting

At P2, the cochlear ducts of FGFR3-iCre;Ai14-tdTomato;ATOH1-GFP pups were microdissected and divided into apical and basal samples. Tissues were then dissociated with enzymatic (accutase and thermolysin) and mechanical dissociation and passed through a strainer in order to create a single-cell suspension, as previously described (Durruthy-Durruthy et al. 2014). In order to enrich for HCs and PC/DCs before sequencing, cells were purified with FACS using a MoFlo Astrios (Beckman Coulter, University of Michigan Flow Cytometry Core). The FACS gating strategy was designed to isolate and pool together cells expressing, tdTomato+, tdTomato+/GFP+, and GFP+ from either the apical or basal samples before being subjected to standard 10x Genomics preparations for scRNA-seq or scATAC-seq experiments.

3.5.3 RNAScope and immunofluorescence combined staining

Cochlear samples from P2 neonatal mice were fixed in 4% paraformaldehyde (Electron Microscopy Sciences, 15710) diluted in 1XPBS (Thermo, 20012017) for 3 hours at room temperature, washed in 1XPBS (Thermo), subjected to a sucrose gradient, then embedded in O.C.T. Compound (Fisher, 4585) for cryosectioning. 18 μm sections were utilized for RNAScope and immunofluorescent experiments.

For RNAScope, sections were incubated in RNase/DNase Free Water (Invitrogen, AM9932) for 5 minutes, dehydrated using an ethanol gradient (50%, 70%, 90%, 100%), and subjected to RNAScope staining using the Advanced Cell Diagnostics (ACD) RNAScope Multiplex Fluorescent Reagent Kit v2 (ACD, 323110) with the following modifications. Antigen retrieval was performed at 65°C for 5 minutes and no blocking steps were performed following development of fluorophores.

RNAScope samples were then prepared for immunofluorescence staining by washing in 0.1% Triton-X (Sigma, 1086431000) in 1XPBS (Thermo), primary antibodies were applied in

0.05% Triton-X in 1XPBS overnight at 4°C. Then, secondary antibodies were applied in 0.05% Triton-X in 1XPBS for 60 minutes followed by DAPI (Sigma, 10235676001) nuclear staining for 10 minutes. All washes between primary and secondary antibody application were performed with 1XPBS (Thermo). The following primary antibodies were used: MYOSINVIIA (Proteus Biosciences, 25-6790) and SOX2 (Santa Cruz, sc-17320). The RNAScope probe was designed by and ordered from ACD, mm-*Pkhd1l1* (44001-C3). All fluorescent images were acquired using a laser scanning confocal microscope (Leica, SP8).

3.5.4 Immunofluorescence staining

Cochlear samples from P2 neonatal mice were fixed in 4% paraformaldehyde (Electron Microscopy Sciences) diluted in 1XPBS (Thermo) for 2 hours on ice, washed in 1XPBS (Thermo), subjected to a sucrose gradient, then embedded in O.C.T. Compound (Fisher) for cryosectioning at 18 μm thickness. Sections were blocked in 1% bovine serum albumin (BSA, Thermo Scientific, BP9700100) in 2% Triton-X/1XPBS for 60 minutes at room temperature and primary antibodies were applied overnight at 4°C in 0.5% BSA/2% Triton-X/1XPBS. The following primary antibodies were used: MYOSINVIIA (Proteus Biosciences), SOX2 (Santa Cruz, sc-17320), TCF4 (Proteintech Group, 50560760), GLIS3 (Thermo Scientific, PIPA541677), FOXO4 (Proteintech Group,501733469), and ZBTB18 (Invitrogen, PA5100372). Secondary antibodies were applied in 0.5% BSA/2% Triton-X/1XPBS for 90 minutes at room temperature followed by DAPI (Sigma) nuclear staining. All washes following primary and secondary antibody application were performed with 2% Triton-X/1XPBS. All fluorescent images were acquired using a laser scanning confocal microscope (Leica, SP8).

3.5.5 10x Genomics pipeline

Single-cell processing and next-generation sequencing was carried out in the Advanced Genomics Core at the University of Michigan. Sequencing was performed on the 10x Chromium and Next GEM accessory kit (10x Genomics, 1000202) using Chromium Next GEM Chip G Single Cell Kit (10x Genomics, 1000120) for scRNA-seq and Chromium Next GEM Chip H Single Cell Kit (10x Genomics, 1000162) for scATAC-seq. The following kits were utilized for library preparation: Chromium Next GEM Single Cell 3' Kit v3.1 (10x Genomics, 1000268), Library Construction Kit (10x Genomics, 1000190), and Dual Index Kit TT Set A (10x Genomics, 1000215) for scRNA-seq, and Chromium Next GEM Single Cell ATAC Library and gel bead kit v 1.1 (10x Genomics, 1000175) and Single Index Kit N Set 4 A (10x Genomics, 1000212) for scRNA-seq.

3.5.6 scATAC-seq analysis

We started with preprocessing the data using SnapTools (Fang et al. 2019) (*snaptools snap-pre --min-flen=50 --min-cov=100 --max-num=20000 --keep-single=FALSE --overwrite=True*). Then we binned the whole genome into 5kb fixed windows and estimated the read coverage for each bin to generate a cell-by-bin matrix (*snaptools snap-add-bmat --bin-size-list 5000*). Bins that overlapped with ENCODE-defined blacklist regions were removed and bins within unwanted chromosomes, like ChrUn, Chr_random, and chrM, were filtered out as well. To select high-quality cells, we kept cells with a log10 UMI count between 3 and 5 and with a promoter ratio ranging from 0.2 to 0.8. After stringent quality control, 1,210 single cells were subject to further analysis. First, we binarized the cell-by-bin matrix. We then followed the pipeline to run the dimensionality reduction method, Diffusion maps, and selected the first 15 significant components (*eigs.dim=15*). The 15 significant components were used to construct the k-nearest neighbor graph and the Leiden algorithm was leveraged for clustering with resolution

0.2 (*resolution=0.2*). Finally, 6 clusters from the scATAC-seq dataset were identified and visualized by projecting meta-data, like read depth and library ID, using UMAP.

Upon clustering, cells from each cluster were aggregated to generate an ensemble track for peak calling. Peak calling was performed for each cluster separately using runMACS function in SnapATAC with following parameters: *--nomodel --shift 100 --ext 200 --qval 5e-2 -B --SPMR*. Two output files for each cluster were generated: a narrawPeak file including identified peaks; a bedGraph (.bdg) file was converted into BigWig format (.bw) using *bedGraphToBigWig* downloaded from UCSC Genome Browser for visualization. Next, all peaks were merged across clusters and a cell-by-peak matrix was created for differential analysis. Differentially accessible regions (DARs) for 6 clusters were determined using *findDAR* function in the SnapATAC with following parameters: *cluster.neg = NULL, cluster.neg.method="knn", test.method="exactTest", bcv=0.1*. In total, we identified 67,415 DARs under the adjusted *P*-value with Bonferroni correction of 0.05. Additionally, we annotated the DARs to the nearest gene by employing the *annotatePeak* function in ChIPseeker R package.

3.5.7 Quality control of scATAC-seq dataset

We used ataqv (Orchard et al. 2020), an ATAC-seq QC and visualization tool, to measure and estimate quality of the scATAC-seq data. Once 6 clusters were identified from scATAC-seq dataset, we aggregated the cells from the same cluster and treated each cluster as a small bulk ATAC-seq dataset. We included mm10 blacklist and mm10 TSS reference files and ran *ataqv* for each cluster separately with the following parameters: *--ignore-read-groups, --tss-extension 2000bp*. To visualize the TSS enrichment based on the transposition activity around TSS, we generated a 100bp window to aggregate the signals and took an average. Next, we applied a

natural spline method to interpolate data points. Similarly, we created a 20bp window and applied the natural spline method to visualize the fragment length distribution.

3.5.8 scRNA-seq analysis

The scRNA-seq dataset was analyzed using Seurat v3 pipeline (Stuart et al. 2019). We selected the cells with the number of features ranging from 600 to 8,000, and the maximum allowed fraction of mitochondrial genes per cell was 10%. Overall, 695 cells passed the quality control for further analysis. After the preprocessing step, log normalization was performed, and the top 2000 highly variable genes were identified using method *vst* with default settings. We scaled the datasets to avoid the domination of highly expressed genes and used it as input for PCA to reduce dimensions. The first 10 principal components were chosen to construct the shared nearest neighbor graph with 20 nearest neighbors (*k.param=20*). Leiden algorithm was performed to identify clusters with resolution 0.5 (*resolution=0.5*) and 11 clusters were resolved. We leveraged UMAP to visualize the scRNA-seq clustering results and meta-data information, like read depth and library ID.

To determine cell identities for each cluster, we first identified differentially expressed genes (DEGs) for each cluster using *FindAllMarkers* function in the Seurat package with following parameters: *only.pos = TRUE, min.pct = 0.25, logfc.threshold = 0.25, test.use = "wilcox"*. In total, we determined 5,772 DEGs for 11 clusters under the adjusted *P*-value with Bonferroni correction of 0.05. Next, we annotated cell identities by comparing cluster specific DEGs with published canonical marker genes.

3.5.9 Cell type identification in scATAC-seq clusters using Jaccard index similarity matrix

We generated a Jaccard index similarity matrix by calculating normalized overlaps between DEGs and annotated DARs from scRNA-seq and scATAC-seq data. Specifically, we performed the calculation for each comparison between pairs of scRNA-seq and scATAC-seq clusters:

$$J(A_i, B_j) = \frac{|A_i \cap B_j|}{|A_i \cup B_j|} \quad i = 1,2,\dots,11 \;\; j = 1,2,\dots,6$$

where A_i is the DEGs of cluster i $(i = 1,2,\dots,11)$ from scRNA-seq, and B_j is the annotated DARs of cluster j $(j = 1,2,\dots,6)$ from scATAC-seq. $J(A_i, B_j)$ is the Jaccard index by calculating the number of intersected genes between A_i and B_j over the total number of unique genes of A_i and B_j. The values were centered and scaled in scATAC-seq clusters. Based on the Jaccard index similarity matrix, we annotated the scATAC-seq clusters with the most similar cell identities from scRNA-seq data.

3.5.10 LIGER multi-omics integration

We applied LIGER (Welch et al. 2019) to jointly define cell identities by leveraging scRNA-seq and scATAC-seq datasets. Briefly, LIGER delineates shared and dataset-specific features to integrate single-cell multi-omics data using integrative non-negative matrix factorization. In order to run LIGER, we first annotated the fragments to the gene level in SnapATAC and generated gene-by-cell matrix for scATAC-seq. We took gene-by-cell raw counts from scRNA-seq as another input. Next, we extracted differentially expressed genes across cell types, identified from Seurat package from scRNA-seq, as variable genes in LIGER. Then, joint matrix factorization algorithm was performed on the normalized and scaled scRNA-seq and scATAC-seq data with defined 20 latent variables (*k = 20*). We conducted quantile normalization, Louvain clustering, and dimensionality reduction and visualization using UMAP

(*distance="cosine", n_neighbors=30, min_dist=0.3*). To validate the similarity-based approach, we projected the cell identities as determined from Jaccard index similarity matrix onto the co-embedding UMAP.

3.5.11 TF motif activity estimation

We applied chromVAR (Schep et al. 2017) to infer TF-associated accessibility and to characterize potential TFs regulating cell differentiation and function from scATAC-seq dataset. Briefly, chromVAR aggregates peaks that share a common feature (e.g. TF motif) and corrects bias in terms of technical confounders (e.g. GC content, average accessibility) based on background peak sets. The accessibility of a TF motif was determined by calculating standardized *z*-scores. To prepare for chromVAR, the mouse HOCOMOCO v10 database was applied and peaks with less than 3 fragments overlapped (*min_fragments_per_peak = 3*) were filtered. We ran the pipeline using the default settings. A TF-by-cell matrix of *z*-scores was generated for further analysis.

To validate the clustering consistency of the scATAC-seq dataset between SnapATAC and chromVAR methods, we applied the dimensionality reduction and visualization method, UMAP, to the TF-by-cell matrix generated from chromVAR. SnapATAC cluster IDs were projected onto the *z*-score-based UMAP.

3.5.12 TF classification into activators and repressors

We developed an integrative approach to classify the mode of action of developmental TFs into activators and repressors by comparing two populations that share a common progenitor using multi-omics single-cell datasets. In the first step, we conducted Student *t*-tests with Bonferroni correction (*P*-adjust < 0.05) and identified differentially expressed TF genes and

differential TF motifs from scRNA-seq and scATAC-seq datasets, respectively. Additionally, the Wilcoxon sum rank test and median value comparison were also provided for consideration. Classification was based on the relation between the TF gene expression level and TF motif accessibility for each individual TF.

The same pipeline was employed to identify TFs regulating HC vs PC/DC differentiation and IHC vs OHC differentiation. For the IHC/OHC comparison, Wilcoxon sum rank tests with Bonferroni correction (P-adjusted < 0.05) were conducted because of the biased sample size and violation of normality assumption.

To validate our classification approach, we adopted previously published algorithm, diffTF (Berest et al. 2019), and compared the overlaps between the two methods. diffTF, a bulk-based approach, compares two groups with multiple biological replicates using Pearson correlation by leveraging matching RNA-seq and ATAC-seq datasets. To apply diffTF, we divided individual cells into 4 groups based on the cell order ranks from 1D spatial reconstruction map for scRNA-seq and scATAC-seq data, separately, to satisfy the matching datasets. Then we created 4 "pseudo" bulk replicates, for RNA-seq and ATAC-seq separately, by aggregating cells from the same group. Next, we ran diffTF using the mouse HOCOMOC v10 database with the following parameters: *nPermutations: 100, nBootstraps: 0, nCGBins: 10, RNASeqIntegration: true, pairedEnd: true, peakType: "narrow", minOverlap: 2*.

3.5.13 TF footprint identification

Footprints are generated by TFs bound to DNA, preventing the Tn5 transposase from cutting DNA in nucleosome-free regions. HINT-ATAC (Li et al. 2019a), an HMM-based algorithm, was employed to identify TF binding sites with footprints for HC- and PC/DC-populations. In preparation for running HINT-ATAC, peak files and indexed bam files for HCs

and PC/DC were generated by aggregating cells from the same clusters. We started with calling footprints for HCs and PC/DCs separately by running the function *rgt-hint* footprinting with the following parameters*: --atac-seq --paired-end --organism=mm10*. Next, TF-associated footprints for each cluster were identified by detecting motifs from the mouse HOCOMOCO v10 database overlapping with predicted footprints using the *rgt-motifanalysis* matching function. Finally, we generated average scATAC-seq profiles around binding sites of each TF for the two clusters separately by running the *rgt-hint* differential function with the following parameters: *--organism=mm10 --bc --nc 2*. We applied the same analytical workflow and predicted footprints among 4 different states of HCs identified by CellTrails.

3.5.14 Gene regulatory network inference

A gene regulatory network (GRN) is a directed graph, which is made up of nodes (e.g. genes, TFs) with directed links between them. Inferring regulatory relationships between TFs and putative downstream target genes is essential for understanding cell differentiation and development. Up to date, numerous algorithms exist to reconstruct GRNs. However, there are few methods integrating gene expression and chromatin accessibility profiles at single-cell resolution. We followed the SCENIC algorithm (Aibar et al. 2017) and developed a 3-step pipeline to reconstruct GRNs. We took HCs and PC/DCs as an example to reconstruct the regulatory landscape.

The first step is to identify co-expression modules from scRNA-seq data using GENIE3 (Huynh-Thu et al. 2010). Briefly, GENIE3 decomposes the network into a lot of regressions. For each regression, the gene expression level of a target gene is predicted from the expression patterns of the TFs using tree-based methods such as Random Forest or Extra-Trees. We applied GENIE3 to identify co-expression modules for HCs and PC/DCs. For running GENIE3, we

selected 1,846 genes, including DEGs for both cell types and TF genes identified from the mouse HOCOMOCO v10 database, and generated a gene-by-cell matrix as input for the GENIE3 algorithm. We calculated the Spearman correlation between each pair of genes. Next, we ran GENIE3 to determine co-expression modules and integrated the correlations with the following parameters: *treeMethod = "RF", threshold = 0.005*. The threshold parameter filtered out the TF/target gene links with a weight below 0.005. In total, GENIE3 yielded 103,041 TF/target gene links for further analysis.

The second step is to identify direct target genes of TFs, which includes setting up a quality control for GENIE3 by scanning putative TF binding sites within accessible regions and removing the links lacking TF binding sites. Specifically, we performed an analysis of TF binding using FIMO (Grant et al. 2011) for HCs and PC/DCs with default settings and the mouse HOCOMOCO v10 database. The TF-target gene links which lack putative TF binding sites within an upstream and downstream 50kb window of the target gene TSS were filtered out. Next, we defined TF regulons, groups of genes regulated by TFs, by considering all possible interacted genes associated with the respective TFs. Furthermore, we filtered out regulons in which the number of downstream target genes was less than 10 or greater than 900 to keep the methods robust. Based on previous classifications, activator and repressor regulons were determined separately. Additionally, since GENIE3 does not consider autoregulation, we complemented the regulons with autoregulated genes by checking whether the TF binding sites are within the 100kb window of the TSS of the same TF gene.

The third step is to calculate regulon enrichment scores for each individual cell using AUCell (Aibar et al. 2017). Briefly, AUCell, a ranking-based method, uses the “Area Under the Curve” (AUC) of the recovery curve to determine the enrichment of regulons for individual

cells. We first ranked all genes for each cell using the function *AUCell_buildRanking* with default settings. Next, AUC for each regulon in each cell was calculated using *AUCell_calcAUC* function, and only the top 1% of the genes in the ranking were used. Additionally, hierarchical clustering was conducted for both regulons and cells and was added in the heatmap.

We followed the 3-step pipeline to identify TFs controlling IHC and OHC differentiation by predicting the GRN. We selected IHC-specific genes, OHC-specific genes, and TF genes from the mouse HOCOMOCO v10 database. GENIE3 was applied to identify co-expression modules with parameters: *treeMethod = "RF", threshold = 0.001*. In step 2, we performed FIMO motif scanning algorithm for HC peaks only. We filtered out regulons in which the number of downstream target genes was less than 10 or greater than 200. To calculate regulon enrichment scores for IHCs and OHCs, we used exactly the same settings as the previous analysis.

3.5.15 1D spatial reconstruction of HCs

We resolved the anatomical positions of HCs at the single-cell level from scRNA-seq and scATAC-seq data by following the conceptual idea previously published for the reconstruction of the mouse organ of Corti from single-cell qPCR data (Waldhaus et al. 2015). First, we identified 427 DEGs ($P < 0.005$) and 127 DARs ($P < 0.001$) between apical and basal compartments from scRNA-seq and scATAC-seq data, respectively. While loosening the threshold would include more DARs, a lot of false positive DARs would likely be included. To deal with the problem, we ran a permutation test for 100 iterations. Specifically, we permutated the cells 100 times while keeping the original apical/basal cell ratio. For each iteration, peaks were called for permutated apical and basal cells, separately, and DARs were determined using the function findDAR from SnapATAC. We used the boxplot to show the number of DARs identified for 100 iterations under different cutoffs.

The hypothesis is that using spatially differential features (e.g. DEGs and DARs) can resolve the anatomical position of individual cells. Next, we projected the individual cells onto a 2D PCA coordinate system and calculated the centroid locations for apical and basal cells, separately. 2D PCA space was rotated based on the apex-to-base centroid-centroid-vector with the apex facing up. Finally, HCs were placed according to their rank order of PC1, indicating each individual cell's relative position along the tonotopic axis for both scRNA-seq and scATAC-sec data.

3.5.16 Prediction of cis-regulatory interactions

We applied Cicero (Pliner et al. 2018) to calculate peak-to-peak coaccessibility from scATAC-seq data for HC and PC/DC cluster, separately. Briefly, Cicero aggregates accessibility profiles for individual cells from the same cluster and calculated a regularized correlation score for each pair of peaks within a 500kb window using a Graphical Lasso model. We started with projecting the cell-by-peak matrix, identified from SnapATAC, into a lower-dimensional space by using the function *reduceDimension* with *num_dim=6*. Next, we ran Cicero for accessible regions to compute coaccessibility scores using the default parameters. We then zoomed in a few genomic loci, related to genes *Sox9*, *S100b*, and *Zbtb18*, and visualized the *cis*-regulatory interactions within these loci in different clusters with a lenient cutoff (*coaccess_cutoff=0*). Additionally, putative TF binding sites scanned from FIMO were added to the Cicero map to validate the predicted TF-target gene interactions.

3.5.17 IHC and OHC identification using scRNA-seq data

We identified IHC and OHC subpopulations, with respect to the scRNA-seq data, based on 7 previously published marker genes (Waldhaus et al. 2015). The 7 genes included *Fgf10*,

Fgf8, and *S100a1* as IHC specific genes, and *Slc26a5*, *Fgfr3*, *Cdh1*, and *Ocm* as OHC specific genes. We used these 7 marker genes as features to run UMAP with default parameters. Two subpopulations were identified, and differential analysis was conducted between the two subclusters using Wilcoxon sum rank test ($P < 0.01$).

3.5.18 HC chromatin accessibility trajectory inference

We applied CellTrails (Ellwanger et al. 2018) to reconstruct HC developmental trajectory using *z*-scores from scATAC-seq data. Celltrails employs spectral embedding technique to find a low-dimensional manifold that represents the spatiotemporal relation of cells. To infer the HC differentiation trajectory at epigenomic level, we first prepared a TF-by-cell *z*-score matrix with 426 TF motifs identified from the mouse HOCOMOCO v10 database and 420 HCs. Next, we applied spectral embedding function *embedSample* with default parameters to find a low-dimensional representation and we determined 7 latent variables for further analysis. Hierarchical clustering with a *post-hoc* test was conducted to determine states using the function *findStates* with following parameters: *min_size=0.1, min_feat=5, max_pval=1e-4, min_fc=2*. Then we aligned individual cells to the trajectory using *fitTrajectory* function with default parameters. In summary, we identified 4 states which formed a Y-shape, indicating the bifurcation of HC differentiation. To further investigate the 4 different states, we projected the meta-data information, such as library ID and DAR-based cell rank order, onto the trajectory, and visualized the gradual changes of *z*-scores along the trajectory.

Additionally, we applied Slingshot (Street et al. 2018) to reconstruct and validate trajectory prediction using *z*-scores from scATAC-seq data. Briefly, Slingshot infers the global lineage structure by constructing a cluster-based minimum spanning tree and constructs smooth lineages by fitting simultaneous principle curves. We used the prepared TF-by-cell *z*-score

matrix as input for Slingshot and started by conducting dimensionality reduction using PCA and only the first two PCs were subject to further analysis. Next, we identified clusters using Gaussian mixture model from *Mclust* function in the mclust package and three clusters were determined automatically based on the Bayesian information criterion. To reconstruct the trajectory, we run *getLineages (start.clus= '1', end.clus=c('2','3'))* function to identify global lineage structure and *getCurves* function with default settings to construct smooth curves and order cells. To validate consistency between Slingshot and CellTrails algorithms, we projected the CellTrails states onto the Slingshot trajectory map. Also, we conducted trajectory analysis using Monocle (Trapnell et al. 2014). Monocle, an unsupervised algorithm, reconstructs the trajectory by constructing minimum spanning tree. Similar to CellTrails and Slingshot, HC TF-by-cell *z*-score matrix was used to run Monocle. We generated a newCellDataSet object with Gaussian distribution because the data were already transformed to be normally distributed. Then we conducted dimensionality reduction by running *reduceDimension* function with the following parameters: *max_components = 4,reduction_method = 'DDRTree',norm_method = "none",scaling = T*. Next, we ordered cells using *orderCells* function with default settings. To validate consistency between Monocle and CellTrails algorithms, we projected the CellTrails states onto the Monocle trajectory map.

3.5.19 Bulk RNA-seq analysis

To confirm differential expression for the seven TFs highlighted in the volcano plot (Fig. 6A), we leveraged two previously published bulk RNA-seq data sets. Averaged gene expression values for perinatal HCs (Wiwatpanit et al. 2018) were determined and *P*-values indicated accordingly. Same processing for adult HCs (Li et al. 2018) was performed. To identify differentially expressed genes, we conducted one-side Student *t*-test for each individual gene.

3.5.20 Data and code availability

All raw and processed sequencing data generated during this study have been deposited to NCBI Gene Expression Omnibus under the accession: GEO: GSE157398. We have created a GitHub repo containing the code analyzed in this work (https://github.com/shuzwang/P2_cochlea).

3.6 Acknowledgements

We thank the staff at University of Michigan Advanced Genomics Core for assistance with sequencing. We acknowledge members of Dr. Joerg Waldhaus Lab and Yujuan Fu for the discussion of the manuscript. This project was funded by NIDCD/NIH grant (R21DC015861) to J.W.

3.7 My contributions

This project is published in Genome Research (Wang et al. 2021); as indicated by the author list for that paper, this was a project I undertook with Dr. Mary P. Lee, Scott Jones, Dr. Jie Liu, and Dr. Joerg Waldhaus. The diverse set of analyses contained within this work was only possible thanks to the efforts of that diverse team. I performed the bioinformatics and computational analyses, including analysis of scRNA-seq and scATAC-seq data produced for the manuscript. Dr. Joerg Waldhaus and I wrote the manuscript; my writing contribution focused on the bioinformatics analyses, results, and methods sections.

Chapter 4 Identification of RARA Target Genes in the Postnatal Organ of Corti

4.1 Abstract

The mammalian cochlea is composed of a distinct cellular mosaic of sensory hair cells (HCs) and supporting cells (SCs), that develop from a shared progenitor in the prosensory domain of the organ of Corti. Patterning and differentiation of the organ of Corti is controlled by signaling pathways such as Hedgehog (HH) and retinoic acid (RA). RA mediates its biological effects via nuclear receptor superfamily of ligand-activated transcription factors, namely RARs and RXRs. RA signaling contributes to the differentiation of cochlear hair cells, and graded RA signaling activity was observed from the base to the apex. However, the mechanisms underlying RA-dependent control of HC differentiation in the cochlea are not yet fully understood. Therefore, we applied bioinformatics approaches to explore the role of RARA in HC differentiation in the developing cochlea, with an emphasis on RARA's repressive potential in postnatal day 2 (P2) HCs. Through analysis of the gene regulatory networks during HC and SC differentiation, we identified RARA to repress SC-specific genes in postnatal HCs in absence of RA. Among the RARA regulated genes, we found that *Lfng*, a known SC marker, was induced by ectopic RA. Considering that RA is present in the embryonic cochlea, these findings suggest that RA signaling has two functions during cochlea development. 1) Binding of RA to RARA in the embryonic cochlea is likely to induce SC specific genes in prosensory progenitors, whereas 2) absence of the ligand renders the receptor into a transcriptional repressor blocking the expression of SC specific genes in postnatal HCs.

4.2 Introduction

The mammalian cochlea's sensory epithelium, also known as the organ of Corti (OC), comprises a stereotypical pattern of sensory hair cells (HCs) and supporting cells (SCs). The organ forms a cellular mosaic consisting of one inner HC row, three outer HC rows, and several SC types along the longitudinal axis. During embryonic development, the organ of Corti's distinct cell types arise from progenitors in the prosensory domain (Wu and Kelley 2012). Cochlear duct proliferation from the otocyst's ventral side occurs first at around E11.5. A day later, prosensory progenitors in the organ's apex leave the cell cycle and become postmitotic, as demonstrated by the expression of *p27Kip1* (Chen and Segil 1999, Löwenheim et al. 1999). A wave of *p27Kip1* extends from the apex to the base, and progenitor proliferation ceases by E14.5 (Lee et al. 2006b). At this point, developmental directionality inverts, and HCs begin to develop at the mid-base, as shown by *Atoh1* expression (Anniko 1983, Lanford et al. 1999). SC differentiation from prosensory cells appears to follow a timeline similar to HC differentiation, as evidenced by the analysis of SC specific genes, such as *Lfng* (Basch et al. 2016b). As a result, cochlear base cells are more mature than their apical counterparts. The development of the organ of Corti is significantly impacted by HH signaling (Bok et al. 2013, Tateya et al. 2013). SHH is expressed in spiral ganglion cells at E12.5, and while the duct is extending between E12.5 and E14.5, SHH expression recedes towards the apex (Liu et al. 2010). Concurrently, differentiation occurs from the base towards the apex. Gain and loss-of-function experiments suggest that the HH pathway maintains the undifferentiated progenitor state at the cochlear apex and therefore regulates the timing and directionality of differentiation (Bok et al. 2013, Tateya et al. 2013). While these findings indicate a permissive role for HH signaling in the differentiation of the

organ of Corti, the identity of the inductive cues that initiate differentiation remains to be identified.

Retinoic acid (RA) is a known regulator of embryonic development (Duester 2008), and it has been identified as a candidate to induce cellular differentiation in the OC (Kelley et al. 1993, Raz and Kelley 1999, Wang 2022). The variety of RA mediated effects is likely due to the combinatorial action of six nuclear receptors (Mark, Ghyselinck and Chambon 2006). Retinoic acid receptors (RARs) and retinoid X receptors (RXRs) are members of the nuclear receptor superfamily of ligand-activated transcription factors that play a crucial role in mediating the biological effects of RA. There are three subtypes of RARs, namely RARα, RARβ, and RARγ, which are encoded by the RARA, RARB, and RARG genes, respectively. Similarly, three RXR subtypes include RXRα, RXRβ, and RXRγ, which are encoded by the RXRA, RXRB, and RXRG genes, respectively. One RAR (α, β, and γ) and one RXR (α, β, and γ) form heterodimers that function as transcription factors. The RAR-RXR heterodimer controls transcription via binding to RAR-RXR specific response elements (RAREs) that are located in regulatory elements of the RA target genes. RAREs consist of hexameric direct repeats (DRs) - (A/G)G(T/G) TCA - with variable interspacing (Umesono et al. 1991). In absence of RA, the unliganded RAR-RXR heterodimer binds to DNA and functions as transcriptional repressor (Janesick et al. 2014, Weston, Blumberg and Underhill 2003). However, upon binding of RA, the receptor complex undergoes a conformational change, leading to its activation as a transcriptional activator (Kashyap and Gudas 2010). This dynamic regulation by RA accounts for significant changes in gene regulatory networks (GRNs) and highlights the importance of ligand-receptor interactions in modulating gene expression.

During the time points between E12.5 and P3 in mice, RARA, RXRA, and RXRG are expressed in the cochlea, indicating that RARA contributes as a common factor to the RAR-RXR complex. To investigate the function of RA signaling in the cochlea, RARA was pharmacologically blocked, which resulted in a negative effect on the differentiation of cochlear HCs, consistent with previous findings that ectopic RA induces supernumerary HCs *in vitro*. This suggests that RARA plays a role in the differentiation of auditory HCs. Additionally, using the RARE-reporter mouse line, graded RA signaling activity was observed from the base to the apex, and a potential contribution to longitudinal patterning was suggested. However, the mechanisms underlying RA-dependent control of HC differentiation in the cochlea are not yet fully understood, and the identification of target genes that mediate RA signaling in the cochlea is necessary.

In this study, we employed bioinformatics approaches to investigate the role of RARA in the differentiation of HCs in the developing cochlea. Specifically, we focused on the potential repressive function of RARA in postnatal day 2 (P2) HCs. By analyzing the gene regulatory network active in differentiating HCs and SCs, we were able to identify SC-specific genes that were regulated by RARA. Notably, we found that the expression of *Lfng*, a known marker of SCs, was induced by RA treatment and was repressed by RARA in P2 HCs. These results suggest that RA signaling induces the differentiation of a pool of precursor cells that have the potential to differentiate into both HCs and SCs of the organ of Corti.

4.3 Results

4.3.1 Identification of RA target genes

Experiments using organotypic culture revealed that RARA plays a key role in RA signal transduction in the mouse cochlea (Raz and Kelley 1999). Hence, we hypothesized that

identification of RARA target genes would allow us to infer the function of RA signaling in the cochlea. We extracted RARA target genes from a gene regulatory network that was originally generated to investigate transcription factors that control HC and SC differentiation from mouse scRNA-seq and scATAC-seq data (Wang et al. 2021). At P2, Rara is differentially expressed in cochlear HCs (***Figure 4.1*A**). At the same time, the chromatin accessibility of the RARA motif (***Figure 4.1*B**) (Kulakovskiy et al. 2013) is significantly reduced in HCs compared to SCs (***Figure 4.1*C**). The negative correlation of RNA expression level and motif accessibility indicates that the transcription factor is likely to function as a transcriptional repressor (Wang et al. 2021). Thus, RARA was predicted to function as transcriptional repressor in P2 HCs. Next, RARA target genes, called RARA regulon, were extracted in a two-step process. First, due to the repressive function of RARA, we identified negatively correlated genes using the scRNA-seq data. Second, to identify direct target genes, we scanned the scATAC-seq data for accessible RARA motifs associated with the negatively correlated genes. The RARA regulon featured 75 genes, including *Lfng*, *Fgfr3*, *Aqp11*, and *S100b* (Basch et al. 2016b, Buckiová and Syka 2009, Miyoshi et al. 2017, Waldhaus et al. 2015), commonly SC specific markers (**Table *4.1***).

TF	Downstream Target Genes
RARA	*4930523C07Rik, Actn4, Aktip, Aldoc, Aqp11, Arrdc4, Atf3, Cask, Cd9, Cep41, Chadl, Ckap4, Cldn3, Cldn7, Clstn1, Clu, Col9a2, Cpq, D430041D05Rik, Dctd, Efhd1, Emid1, Eno1, Fam3c, Fgfr3, Fkbp1a, Fkbp4, Fzd9, Gapdh, Gas2, Gm10638, Gm266, Gm2a, Got2, Gpi1, Gstm1, Htra4, Krt8, Lfng, Lockd, Mad2l2, Masp1, Mctp1, Mfap2, Mgst1, Mta3, Otogl, Pantr1, Pdia6, Pgk1, Ppp2r2b, Prss23, Psma5, Ramp3, Rnd2, Rora, Rps9, Rxrg, S100b, Saraf, Sdc4,*

	Sh3glb2, Slc25a5, Smad1, Tmem189, Tmem59, Tmem86a, Trp53, Tuba1a, Tubb2b, Vav3, Wdr1, Wsb2, Zdhhc12, Rara

Table 4.1 List of downstream target genes of the RARA transcription factor identified through gene regulatory network analysis.

Next, gene set enrichment scores for the RARA regulon were calculated using AUCell (Aibar et al. 2017) and the regulon was determined to be differentially active in cochlear supporting cells at P2 (***Figure 4.1*D**). Together these findings suggest that RARA functions to repress SC specific genes in immature HCs of the postnatal organ of Corti.

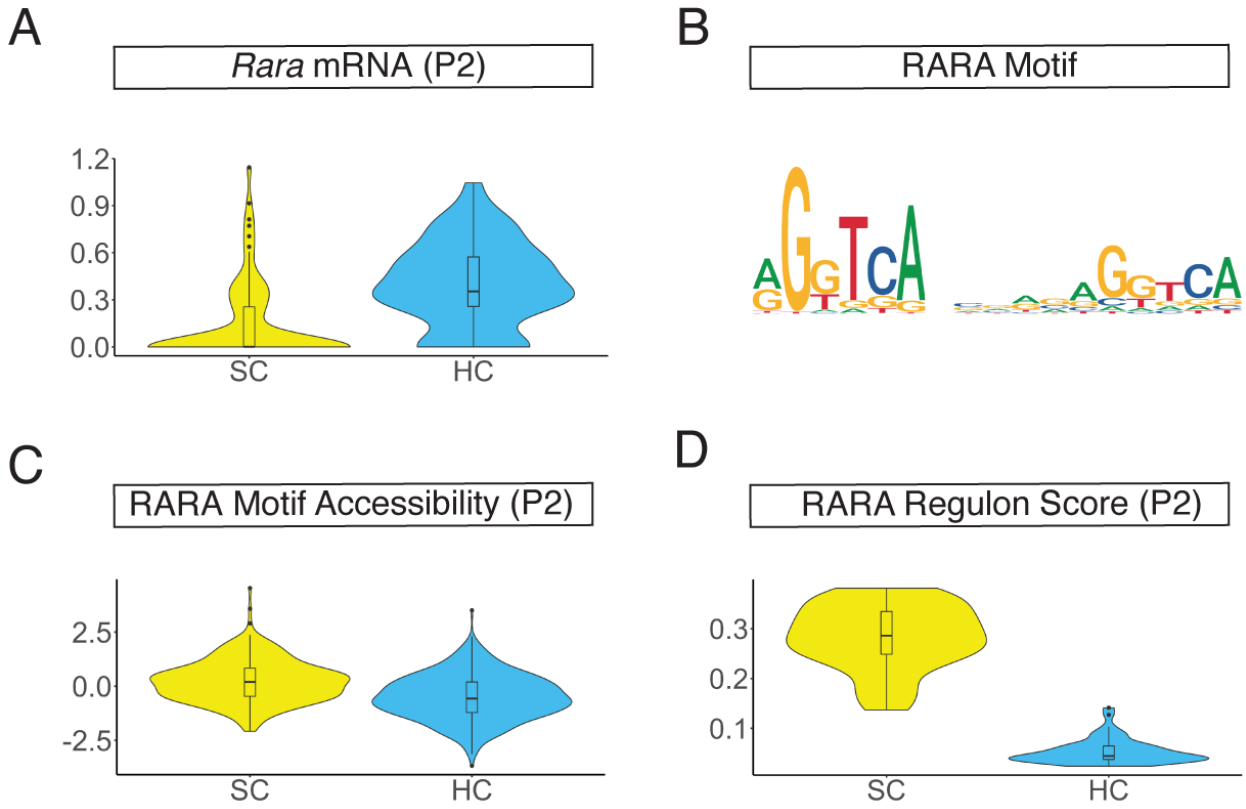

Figure 4.1 RARA TF activities from single-cell multi-omics data. (A-D) RARA activities in P2 HCs and SCs in terms of mRNA expression, motif accessibility, and regulon enrichment. (A) Violin plot of differential *Rara* mRNA expression between HCs and SCs. (B) RARA PWM motif logo from HOCOMOCO v10. (C) Violin plot of differentially accessible *z*-score of RARA motif accessibility in HCs and SCs. (D) Differential RARA regulon enrichment scores between HC and SC. The box plots show the interquartile range (box limits), median (centre line), minimum to maximum values (whiskers).

4.3.2 RARA motif in putative enhancer-promoter pairs at the Lfng locus

The prediction of the RARA regulon was based on differential *Rara* expression and differential RARA motif accessibility between HCs and SCs. Next, we aimed to test if RARA motifs localize to putative regulatory elements of the regulon genes and if RXR motifs are present in close proximity to allow for the binding of the RAR-RXR heterodimer. First, we focused on *Lfng* and predicted putative gene regulatory elements at the *Lfng* gene locus for HCs and SCs separately using Cicero (***Figure 4.2*A-B**) (Pliner et al. 2018). Based on previous reports about RA receptors present in the cochlea, motif scanning was restricted to RARA, RXRA, and RXRG (Raz and Kelley 1999, Wang 2022). In SCs, two of the predicted gene regulatory elements featured direct repeats of RAR and RXR motifs. The first predicted regulatory element, RE1, is located within 5 KB of the *Lfng* transcription start site (TSS) (*chr5:140611612-140611632*) and the FIMO (Grant et al. 2011) scanning revealed a RARA-RXRG motifs in tandem (***Figure 4.2*A**). The second regulatory element, RE2, is located within the 3' UTR of *Lfng* (*chr5:140621524-140621549*) and FIMO scanning identified potential binding sites for RARA, RXRA, and RXRG in direct repeats (***Figure 4.2*A**). In HCs, RE1 remains accessible, while the chromatin at RE2 appears in a closed state (***Figure 4.2*B**).

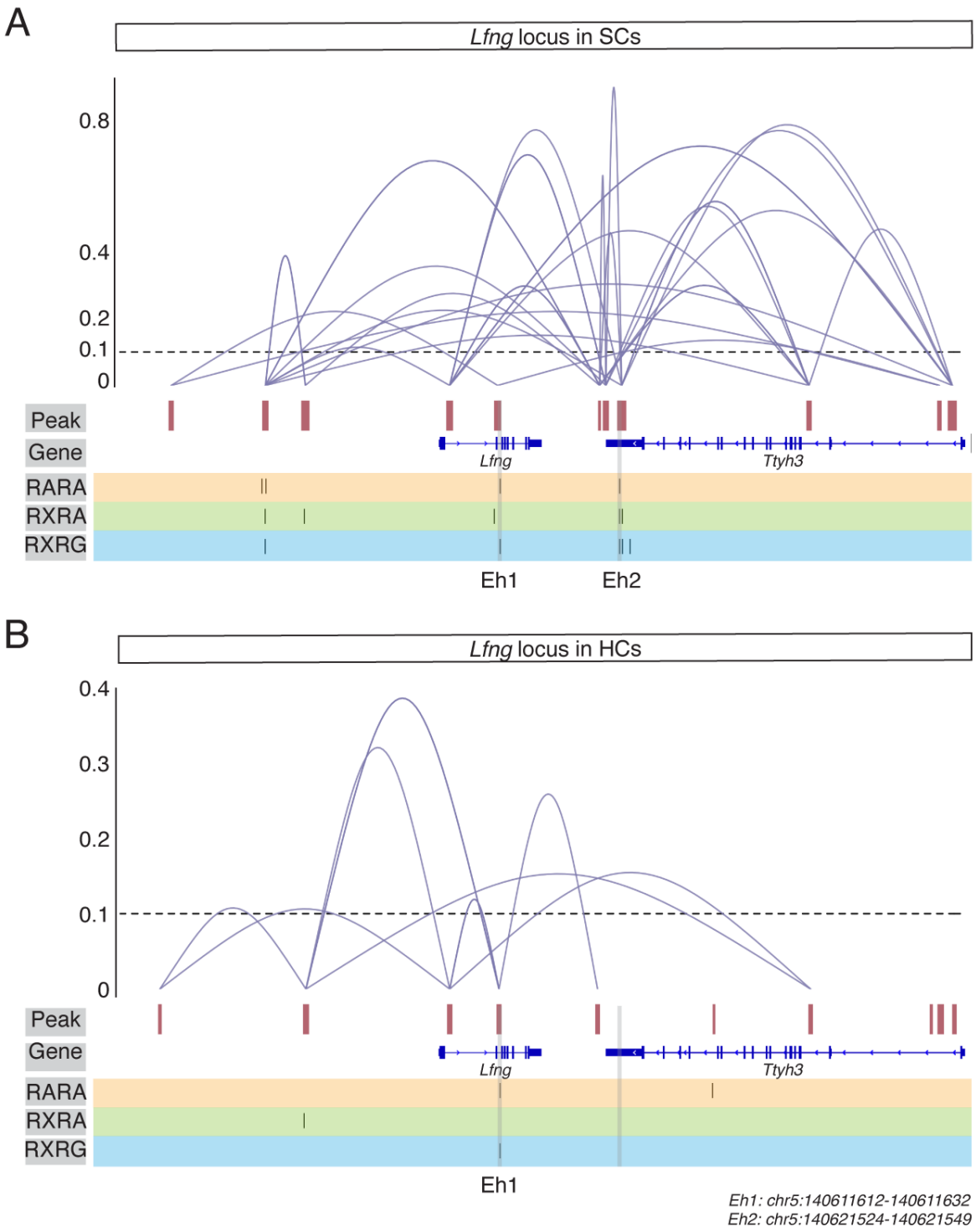

Figure 4.2 *cis*-regulatory landscape of *Lfng* gene locus. (A-B) Co-accessibility analysis of the *Lfng* gene locus was performed in HC and SC clusters at P2, respectively. (A) In SCs, the *Lfng* TSS is directly and indirectly connected to the accessible sites that correspond to putative regulatory elements. The putative regulatory elements were scanned for RARA, RXRA, and RXRG motifs. Top row: Co-accessibility plot connects predicted regulatory elements and the accessible regions align with the *Lfng* locus. Second row: Accessible regions aligned with the

Lfng locus. Third row: Genome annotation from UCSC Known Genes. Putative TF binding sites of RARA (forth row), RXRA (fifth row), and RXRG (sixth row) motifs relative to the accessible regions. Two regulatory elements (Ehs) were highlighted in the plots: Eh1 (*chr5:140611612-140611632*) indicates the co-localization of RARA and RXRG motifs, and Eh2 (*chr5:140621524-140621549*) reveals potential binding sites for RARA, RXRA, and RXRG in direct repeats. (B) An analogous data representation was provided for the *Lfng* locus in the HC cluster.

Since ectopic RA was found to induce the formation of supernumerary HCs in organotypic cultures (Kelley et al. 1993), we aimed to determine if RARA potentially regulates *Atoh1* expression directly. Three regulatory elements have previously been identified at the Atoh1 locus using ChIP-seq and ATAC-seq methodologies (Luo et al. 2022, Tao et al. 2021). All three elements were identified as potential regulatory elements using Cicero in P2 HCs and two out of the three were accessible in SCs as well. Motif scanning did not reveal RARA motifs in any of the three elements. However, a putative regulatory element was identified about 5KB upstream of the *Atoh1* TSS that exhibited a RARA-RXRG repeat, which was accessible in HCs and SCs of the P2 organ of Corti (Wang et al. 2021).

4.3.3 Function of RA during embryonic development of the cochlea

Based on our gene regulatory network analysis (Wang et al. 2021), RARA was classified to function as a transcriptional repressor in P2 HCs. Previous studies concluded that RA signaling is low or absent in the postnatal cochlea (Kelley et al. 1993, Wang 2022), which supports a repressive role for RARA considering the classic model of RA signaling (Weston et al. 2003). However, based on the same studies, RA signaling is active in the embryonic cochlea around E14.5, raising the question if RARA functions as transcriptional activator during the early period of cochlear development, accordingly.

To test this hypothesis, we analyzed the expression pattern and regulon activity of RARA in the E12.5 and E14.5 cochlea, a time course where HC and SC precursors are induced from

prosensory progenitors (Wu and Kelley 2012). Briefly, we used previously published (Wang 2022), annotated, and spatially reconstructed scRNA-seq data of cochlear HC and SC precursors and the surrounding cochlear floor to project *Rara* expression levels. As previously reported, *Rara* was detected with diffuse expression in all cells of the developing cochlea for both time points, and no statistical differences were found along the apex-to-base axis or between the different cell types (**Figure *4.3*A-B**). Next, we calculated an activity score for the RARA regulon at single cell resolution using AUCell for the E12.5 and E14.5 data sets. Due to the lack of a specific SC cluster at E12.5, a cell type specific enrichment was not observed. However, at E14.5, cells identified as SC precursors exhibited significantly higher RARA regulon scores compared to the surrounding floor and the neighboring HC precursors (**Figure *4.3*C-D**). Next, we visualized *Lfng* expression as direct target of RARA using the same spatial reconstruction (**Figure *4.3*E-F**). While sparse *Lfng* expression was found across the total length of the E12.5 cochlea, significantly higher *Lfng* expression was detected in E14.5 SC precursors compared to the cochlear floor (**Figure *4.3*F**). In comparison, HC precursor develop during the same time course, but the RARA regulon is not enriched and *Lfng* is not upregulated in HC precursors. Instead, genes such as *Atoh1* are highly expressed in HC precursors (**Figure *4.3*G-H**). Together, these findings identify the RARA regulon to be differentially active in embryonic SC precursors. Considering that RA is present at this point, induction of the RARA regulon in SC precursors appears likely.

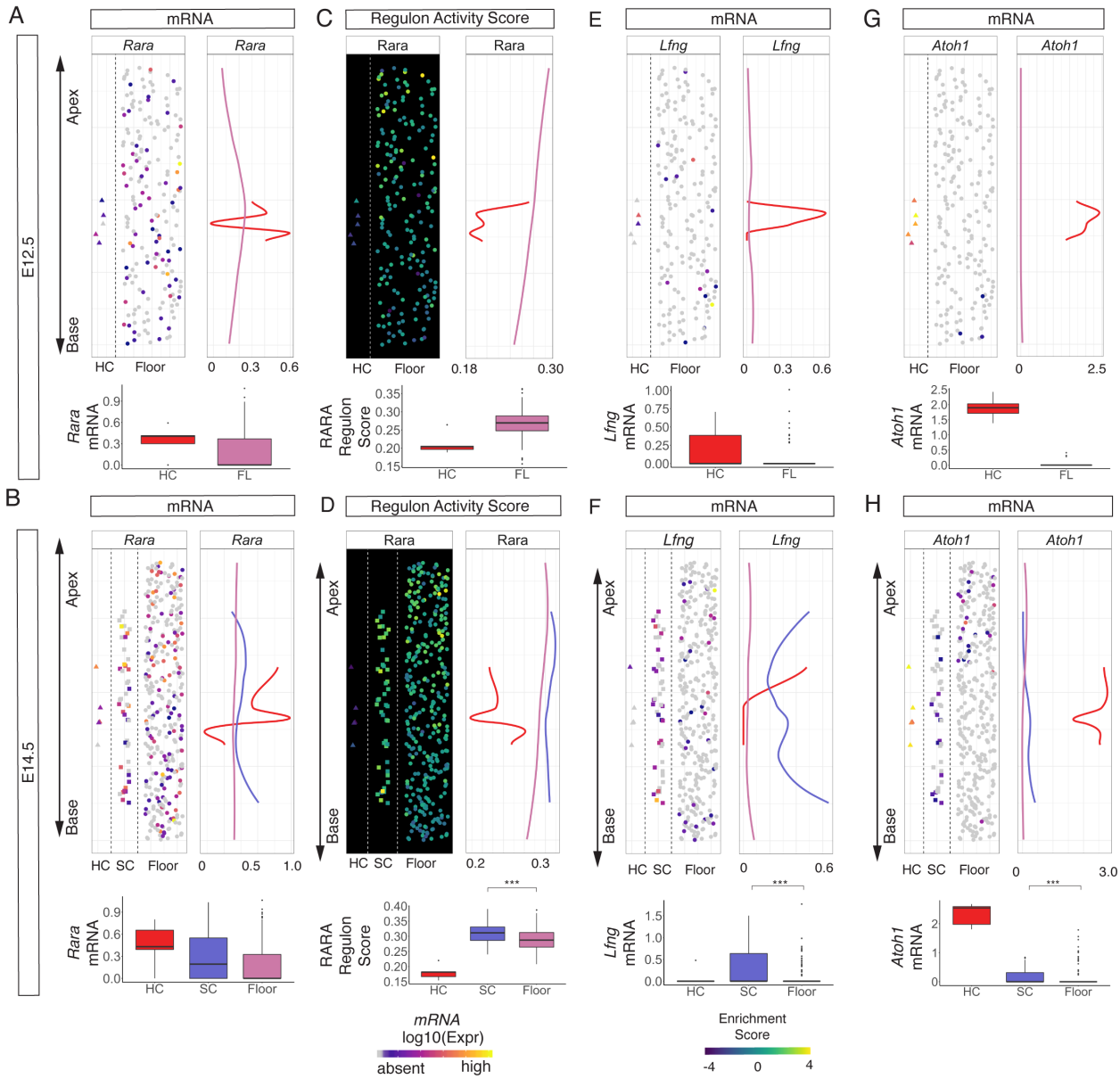

Figure 4.3 Spatial reconstruction of the embryonic cochlear floor including HCs and SCs. (A-H) Spatial reconstruction of E12.5 and E14.5 cochlear floor, HC precursors, and SC precursors through 1D PCA analysis along the apex-to-base axis, with the apex oriented towards the top of the figure. Data points are distributed randomly along the y-axis for better visualization. (A-B) 1D PCA projection of *Rara* gene expression for E12.5 (A) and E14.5 (B), respectively. The boxplots indicate the distribution of *Rara* mRNA expression levels across different cell types in the cochlea. (C-D) RARA regulon activity scores were projected onto the 1D PCA plots for E12.5 (C) and E14.5 (D). The E14.5 boxplot show significantly different regulon activity scores between the SC and cochlear floor cells. ***P=1.03E-5 (two-sided unpaired Wilcoxon rank-sum test). (E-F) *Lfng* delineates SCs for E12.5 (E) and E14.5 (F), respectively. The boxplot at E14.5 indicates a significant difference in *Lfng* expression between SC and floor cells, with higher expression levels observed in SCs. ***P=2.98E-13 (two-sided unpaired Wilcoxon rank-sum test). (G-H) *Atoh1* is shown as a marker for HC precursors for

E12.5 (G) and E14.5 (H). The boxplot at E14.5 indicates a significant difference in *Atoh1* expression between SC and floor cells, with higher expression levels observed in SCs. ***P=8.78E-6 (two-sided unpaired Wilcoxon rank-sum test).

4.3.4 RA induces Lfng expression in vitro

Ectopic RA has been shown to induce supernumerary HCs after 7 days *in vitro* (Kelley et al. 1993). To test if ectopic RA induces *Atoh1* or *Lfng* expression, we applied 500 nM ectopic RA to E14.5 organotypic cultures, collected the explants after 72 h, and stained for *Atoh1* and *Lfng* mRNA using fluorescent in situ hybridization (FISH) (**Figure *4.4*A-B**). While ectopic RA did not significantly change *Atoh1* expression levels at apex, mid, and base locations, a significant upregulation of *Lfng* was found in the apical compartment of the cochlear explant after 72 h. This result supports *Lfng* as a RA regulated gene in the embryonic cochlea and therefore concurs with our GRN analysis.

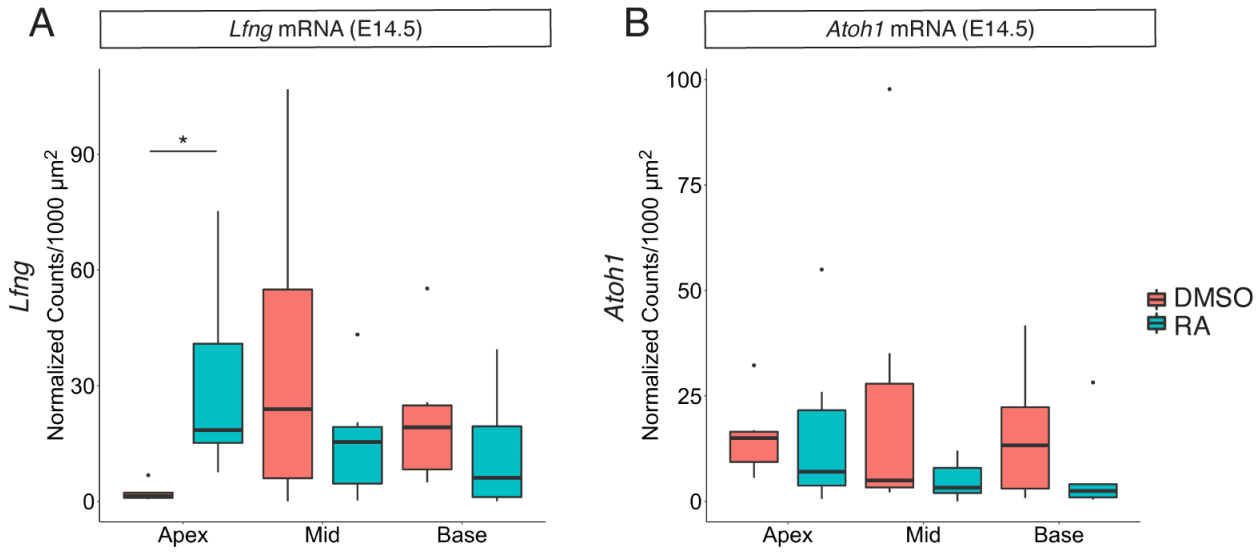

Figure 4.4 Ectopic RA induces *Lfng* expression *in vitro*. E14.5 cochlear explants were cultured for 72 h in control medium and medium supplemented with 500 nM ectopic RA. Specimens were stained for *Lfng* (A) and *Atoh1* (B) mRNA, counterstained with DAPI, imaged in whole mount format, and analyzed in Fiji software. (A) Quantification of *Lfng* puncta normalized to 1000 μm^2. Lfng expression significantly increased in the apical compartment after exposure to 500 nM RA for 72 h (n=6) compared with the control apical treatment (n=6). *P=0.045 (two-sided unpaired *t*-test). (B) Quantification of *Atoh1* puncta normalized to 1000 μm^2. The boxplots

show the interquartile range (box limits), median (centre line), minimum to maximum values (whiskers).

4.4 Discussion

Previous contributions demonstrated that ectopic RA has the potential to induce formation of supernumerary HCs in mouse organotypic cultures (Kelley et al. 1993). In this study, we identified RARA as transcriptional repressor of SC specific genes in P2 HCs. Analyzing the *Lfng* locus, which is one of the RARA regulon genes, RAR-RXR motifs were found to be arranged in direct repeats and localize to putative regulatory elements. The RARA regulon was found differentially active in E14.5 cochlear supporting cells, suggesting that presence of RA likely renders RARA into a transcriptional activator during early cochlear development. Finally, ectopic RA was shown to induce *Lfng* expression in E14.5 organotypic cultures, thereby confirming the bioinformatics predictions regarding the RARA target genes.

Phenotypic results suggest that RA induces differentiation of cochlear HCs (Kelley et al. 1993, Raz and Kelley 1999). This result is based on experiments using ectopic RA and the pharmacologic blocking of RARA in organotypic cultures of the embryonic cochlea. Nevertheless, molecular and cellular targets of RA signaling in the cochlea remain to be identified. While experiments using ectopic RA not only result in the formation of supernumerary HCs but also SCs, an effect of RA on the prosensory progenitor pool was concluded (Kelley et al. 1993). In comparison, experiments blocking RARA affected the expression of a subset of HC specific genes during HC differentiation (Raz and Kelley 1999). This finding does not support the prosensory progenitors as primary target but rather favors HCs instead. In this study, we used a bioinformatics approach to identify RA regulated genes and tested our predictions using organotypic cultures. Using an integrative approach analyzing previously published scRNA-seq and scATAC-seq data (Wang et al. 2021), RARA was

classified to function as transcriptional repressor in P2 HCs. The classic model of RA signaling assumes repressive function for the RAR-RXR heterodimer in absence of the ligand (Weston et al. 2003). Experiments using RARE to drive *lacZ* expression showed low or absent RARE-reporter activity in postnatal organ of Corti (Kelley et al. 1993, Wang 2022); therefore, supporting the classification of RARA as transcriptional repressor.

Integrated scRNA-seq and scATAC-seq data analysis allowed us further to identify RARA regulon genes that are negatively correlated with *Rara* expression and exhibit accessible RARA motifs in proximity to their TSS. Moreover, focusing on *Lfng* as a RARA regulon gene, we were able to identify two direct repeats of RAR-RXR motifs in two putative regulatory elements at the *Lfng* locus in P2 SCs. This finding suggests that both RAR-RXR repeats form active RAREs (Chatagnon et al. 2015, Mark et al. 2006). In comparison, previously published regulatory elements at the *Atoh1* locus (Chen et al. 2020, Tao et al. 2021) did not reveal RAREs. However, a RAR-RXR repeat in a putative regulatory element about 5 KB upstream of the *Atoh1* locus could potentially function to regulate the expression of the transcription factor.

Together, those findings suggest that RARA functions to suppress the expression of SC specific genes in postnatal HCs in absence of RA. Therefore, RA signaling, or the absence of the ligand could be important to support HC differentiation, which is a function that was proposed after blocking RARA pharmacologically (Raz and Kelley 1999).

The findings discussed above, cannot explain the formation of supernumerary HCs. Hence, we aimed to determine the effect of RA binding to RARA in the embryonic cochlea. Upon binding of the ligand, it has been shown that the RAR-RXR complex recruits a different set of co-factors and the function changes into a transcriptional activator (Cunningham and Duester 2015). Assuming that the group of genes that are regulated by RAREs is identical in

presence and absence of the ligand, we asked which cell type would activate the RARA regulon in response to RA being present in the embryonic cochlea. By analyzing RA activity scores at single cell resolution, we found differential scores in E14.5 SC precursors. Given that the *Rara* transcript is ubiquitously expressed in the cochlear floor at this developmental time point (Wang 2022), we speculate that RA induces the expression of SC specific genes in the cochlear floor, supposedly supporting the differentiation of SCs. Induction of supernumerary SC precursors as previously observed (Kelley et al. 1993) could represent the cellular source for the supernumerary HCs in response to ectopic RA. It has also been reported that the capacity of the organ of Corti to generate supernumerary HCs in response to RA decreases and disappears after birth (Kelley et al. 1993). This finding correlates with the proposed switch from transcriptional activator to repressor.

In an attempt to validate that *Lfng* is a RARA regulated gene, we exposed E14.5 organotypic cultures to 500 nM RA. A significant upregulation of *Lfng* was detected in the apical compartment of the cochlea only. Previously, it was reported that application of exogenous RA results in decreased *Lfng* expression in the mouse otocyst between E7.75 and E8.25 (Bok et al. 2011a). However, using E14.5 cochlear explants and ectopic RA, we found a significant upregulation of *Lfng* in prosensory progenitors at the apical end of the cochlea. The different effects of ectopic RA could be due to different combinations of RAR-RXR dimers, therefore leading to different outcomes at both developmental time points. Differentiation of HCs and SCs of the cochlea proceeds in a gradient from the base to the apex (Basch et al. 2016b, Cai et al. 2015); therefore, the capacity to induce *Lfng* expression was restricted to the undifferentiated compartment. Previous research has shown high RARE activity in the cochlear base, while no RA activity was reported apex (Wang 2022). Given that the RA gradient dynamically extends

from the base towards the apex, as indicated by the *RARE-lacZ* reporter between E12.5 and E14.5 (Wang 2022), RA signaling is a candidate to play a critical role in controlling the timing and directionality of differentiation in the mouse cochlea. Further characterization of the RARE-reporter mouse in combination with modulations of RA levels in vivo have the potential to test this hypothesis.

4.5 Methods

4.5.1 cis-regulatory prediction using Cicero

We applied Cicero (Pliner et al. 2018) to calculate peak-to-peak co-accessibility from P2 scATAC-seq data for HC and SC cluster, respectively. Briefly, Cicero aggregates accessibility profiles for individual cells from the same cluster and calculated a regularized correlation score for each pair of peaks within a 500kb window using a Graphical Lasso model. We started with projecting the cell-by-peak matrix, identified from SnapATAC, into a lower-dimensional space by using the function *reduceDimension* with *num_dim=6*. Next, we ran Cicero for accessible regions to compute co-accessibility scores using the default parameters. We then focused on a few genomic loci, related to genes *Lfng* and *Atoh1*, and visualized the *cis*-regulatory interactions within these loci in different clusters with a lenient cutoff (*coaccess_cutoff=0.1*). Additionally, putative TF binding sites of RARA, RXRA, and RXRG scanned from FIMO were added to the Cicero map to validate the predicted TF-target gene interactions.

4.5.2 E12.5 and E14.5 spatial reconstruction of the cochlear duct

To resolve the relative positions of the cochlear floor cells including HCs and SCs, we conducted PCA by leveraging the cochlear floor specific gradually expressed genes as features (Wang 2022). HCs, SCs, and remaining floor cells after otoscore QC were represented in

individual columns of the 1D PCA visualizations. Canonical gene markers and regulons were projected on the PCA plots. The *y*-axis of the PCA plot indicates the tonotopic axis, whereas cells were randomly distributed along the *x*-axis for better visualization.

4.5.3 Regulon enrichment score calculation using AUCell

AUCell (Aibar et al. 2017) was used to identify differentially enriched regulons at single-cell resolution. AUCell, a ranking-based method, uses the area under the recovery curve to determine the regulon enrichment in individual cells. The regulons were determined from the gene regulatory network analysis from P2 single-cell multi-omics data (Wang et al. 2021). First, we selected cells annotated as cochlear duct after otoscore QC, including the cochlear floor, HCs, and SCs; we then ranked all genes for each cell by using the function *AUCell_buildRanking* with default settings. Next, the area under the curve for each regulon for each cell was calculated with the *AUCell_calcAUC* function, and the top 10% of genes in the ranking were used.

4.5.4 Cochlear explant culture

Timed-pregnant FVB/NJ female mice were euthanized at E14.5, embryos of either sex were collected, and cochlea were dissected and cultured as explants between 3 and 72 h. Briefly, the cochlea was separated from vestibular compartments and the whole cochlea was cultured under floating conditions to maintain the 3D structure. Explants were maintained in Neurobasal-A medium supplemented with N2, L-glutamine, D-glucose, and ampicillin (Thermo Fisher) at 37 °C in 5% CO2. Explants were supplemented with 500 nM RA (Sigma-Aldrich) in 0.1% DMSO from the beginning of the culture. Controls were treated with 0.1% DMSO alone.

Explants were then fixed and subjected to in situ staining and immunolabeling to examine the expression of transcripts during cochlear development.

4.5.5 Quantitative FISH

Cochlear whole mounts were processed according to published protocols (van Dijk et al. 2018). To restrict data acquisition to the prosensory domain of the cochlea, we stained explants with anti-SOX2 antibody (Santa Cruz Biotechnology) and counterstained them with DAPI (Thermo Fisher). HCR probe sets were obtained (Molecular Instruments) to detect *Atoh1* (Molecular Instruments, NM_007500.5, lot: PRL500), and *Lfng* (Molecular Instruments, NM_008494.3, lot: PR1896) transcripts. Z-stacks were acquired with a laser scanning confocal microscope (Leica, SP8), and 145 × 145 μm images with 0.3 μm spacing were collected. Transcript puncta were counted through an automated semi-approach (Diaz and Heller 2021) in Fiji software. First, five optical *z*-slices with 0.7 μm thickness were used for analysis. Regions of interest (ROIs) covering the prosensory domain were applied on the basis of the *Sox2* signal. Background was removed from the images with a top hat filter, and images were smoothed with a Gaussian kernel to remove noise. Transcripts were detected as local maxima in this image and distinguished from background noise with an identical intensity threshold applied to all analyzed images. Transcripts were segmented through watershed segmentation, and the ROIs were automatically counted. The total number of puncta per ROI was normalized to 1000 μm^2.

Two-sided *t*-tests were used for comparisons between two groups. To compare the difference between apical and basal compartments under the same experimental condition, we used two-sided paired *t*-tests.

4.5.6 Statistics and reproducibility

Statistical analysis was performed using R on RStudio. A two-sided *P* value of < 0.05 was considered statistically significant.

4.5.7 Data and code availability

Single-cell multi-omics data from P2 including scRNA-seq and scATAC-seq data were obtained from the NCBI Gene Expression Omnibus (GEO) public database, using the accession number GSE157398. scRNA-seq datasets from E12.5 and E14.5 were obtained from the GEO public database under the accession number GSE202588. All of the packages used are available online.

4.6 Acknowledgements

We thank the staff at the University of Michigan Advanced Genomics Core for help and support, and members of the laboratory of J.W. and Linghua Jiang for discussion of the manuscript. We thank Nenad Sestan for support with the *RARE-lacZ* mouse model. This work was supported by NIDCD/NIH grant (R21DC015861) to J.W.

4.7 My contributions

This project is in preparation. This was a project I undertook with Saikat Chakraborty, Jack Ruhala, Dr. Jie Liu, and Dr. Joerg Waldhaus. The diverse set of analyses contained within this work was only possible thanks to the efforts of that diverse team. I performed the bioinformatics, computational, and statistical analyses, including the comprehensive single-cell multi-omics data analysis and multiple scRNA-seq data analysis produced for the manuscript. Dr. Joerg Waldhaus and I wrote the manuscript; my writing contribution focused on the bioinformatics analyses and methods sections.

Chapter 5 Conclusion

In this thesis, we used single-cell transcriptome data to understand the molecular mechanisms conferring spatial information during organ of Corti development in mice (Chapter 2) and we developed a pipeline to integrate epigenomic and transcriptomic single-cell data to investigate the gene regulatory landscape during organ of Corti differentiation (Chapter 3). We also used the pipeline to identify the retinoic acid regulated genes in cochlear development (Chapter 4). Each of these analyses generated new information or resources, but clearly none of them close the door on the problems they are attempting to tackle or the biological traits and systems they are investigating. Together these analyses display the value of epigenomic and transcriptomic data in understanding molecular mechanisms of cochlear development with the ultimate goal to identify molecules and mechanisms that can inform future strategies to regenerate hearing.

In Chapter 2, we investigated the molecular mechanisms underlying the development of the cochlear duct by analyzing scRNA-seq datasets obtained from two embryonic time points of mice (E12.5 and E14.5). Tonotopic patterning, a pivotal event in the development of the organ of Corti, occurs early during the extension of the cochlear duct in mouse embryos. It plays a critical role in providing the necessary spatial information for the differentiation of tonotopically arranged characteristics. Those characteristics are mirrored by tonotopic gene expression gradients. To decipher the molecular mechanisms conferring the tonotopic identity, we proposed two biological hypotheses: 1) a genetic timer with asymmetric cell division or 2) a morphogen

modulated timer might give rise to graded gene expression. By leveraging the gradually expressed genes as feature genes and calculating meta-cell similarity matrix between E12.5 and E14.5 data, our findings suggested that gene expression gradients dynamically adjust during the proliferative extension of the prosensory domain, thereby strongly supporting the morphogen modulated model rather than the cell division-associated mechanism. Our data analysis strategy integrated spatial and temporal information, thus setting it apart from previously applied trajectory-based analysis of the same tissue. While the hypothesis testing supported the morphogen modulated model, subsequent analysis strategy was specifically tailored to investigate spatiotemporal gene expression in 2D and 3D space. Using a PCA-based approach, I was able to successfully reconstruct the 2D and 3D structures of the developing cochlear duct at embryonic time points E12.5 and E14.5. These reconstructions provide a valuable computational platform for the identification of both known and novel marker genes and pathways. RA signaling was identified as a potential candidate pathway governing spatial identity. Our in vitro experiments confirmed functional RA signal transduction after the application of exogenous RA. By incorporating previous findings, we postulate that RA signaling may serve as a fundamental mechanism for determining positional identity during the developmental stages of the mouse cochlea. Further evidence regarding formation of the RA gradient was identified through 3D reconstruction of the cochlear duct for statistical comparison of RA related gene products in different compartments of the model. The RA source and signal receiving cells were found to be spatially separated in the roof and floor. However, the cochlear floor may contribute to final RA concentrations, as visualized by low level expression of RA synthesizing enzymes *Aldh1a3* and *Rdh10* in the circular reconstructions of the cochlea and previously reported for the chicken BP (Thiede et al. 2014). In addition, substantial amounts of RA may potentially emanate from areas

outside of the cochlear duct such as the periotic mesenchyme (Raz and Kelley 1999). Therefore, tissue-specific enzymatic networks negatively controlling RA availability are relevant. CYP26B1 (Romand et al. 2006) and DHRS3 (Ono et al. 2020b) are part of the catabolizing network to reduce RA bioavailability, and both are expressed in decreasing apex-to-base gradients in the cochlear floor at E14.5. This finding suggests that both enzymes contribute to shaping the RA gradient, as has been observed in the developing forebrain, spinal cord, and vestibular end organs in mice (Ohyama et al. 2010, Ono et al. 2020a, Szuts and Harosi 1991). And these findings further support the hypothesis that an RA gradient confers spatial information in the mouse cochlea. Furthermore, HH signaling is known to specify apical identity in the mouse and chicken cochlea. A potential interaction between RA and HH signaling pathways prompts the question of whether a carefully regulated equilibrium between both morphogens might be involved in patterning spatial identity in the mouse cochlea. Application of an RA-receptor blocker or an HH agonist induced expression of the apical reporter *Hmga2* in the basal compartment of the explant. In contrast, exogenous RA or blocking of HH signaling decreased the expression of the apex-to-base reporter in the apical compartment. Our predictions based on the spatial reconstruction of the cochlea supported by our pharmacological approach resulting in mirrored phenotypes provided initial evidence suggesting that opposing RA and SHH gradients function to pattern the apex-to-base identity of the mouse embryonic cochlear duct. Overall, our computational and experimental model provides a valuable tool for further investigation of the embryonic development of the organ of Corti. The results and resources generated by this project will assist future projects to deeply understand cochlear duct development and functionality.

Signaling pathways play a key role in regulating gene expression by activating or repressing transcription factors, which bind to specific DNA sequences and modulate

transcriptional output. In Chapter 3, we investigated the genome-wide heterogeneity of transcriptome and epigenome on single-cell resolution in the P2 mouse organ of Corti. The results are a demonstration of both the advantages of multi-omics data integration as well as the limits and challenges of integrating scATAC-seq and scRNA-seq. Specifically, I developed a comprehensive computational pipeline to compare cell types that develop from shared progenitors. By analyzing the differentially expressed transcription factors (TFs) that display differential motif accessibility, it is possible to discern the collaborative mechanisms more reliably by which multiple TFs coordinate to activate or repress cell type-specific target genes at the whole transcriptome level. Building on the principles of the SCENIC algorithm, we have effectively integrated scATAC-seq data to infer gene regulatory network which identify the direct downstream target genes of each TF. This approach was not conceived to replace classic knock out and over expression experiments, but to provide an alternative approach accessing the whole regulatory network in a single experiment. For example, ChIP-seq experiments require considerably larger amounts of input material compared to the single-cell technology, explaining limited numbers of inner ear specific ChIP-seq data in the literature (Cai et al. 2015, Kwan et al. 2015, Stojanova et al. 2016, Li et al. 2020, Menendez et al. 2020b). Together, this illustrates why the current approach is specifically useful for populations with limited cell numbers, like IHCs in mice, where only about 800 cells exist per mouse inner ear (Ehret and Frankenreiter 1977). In addition, the gene regulatory network prediction algorithm finding 20 TFs including regulons contributing to the differentiation of sensory HCs. Many of the TFs like ZBTB18 were known to cause sensorineural hearing loss (SNHL) (Aleksiūnienė et al. 2017) but their role in inner ear development remained elusive. This is of particular interest, as a limited set of only 4 TFs, namely SIX1, ATOH1, POU4F3 and GFI1, is sufficient to convert fibroblasts into induced HC

like cells (Menendez et al. 2020b). Therefore, these findings illustrate that a limited number of TFs play key roles in controlling the regulatory landscape of HC differentiation, nevertheless, a significantly larger array of TFs is necessary to allow for differentiation of functional HCs. While clustering of previously published marker transcripts allowed for IHC and OHC separation in scRNA-seq data, cellular identities were less prominent when analyzing scATAC-seq data. Based on the trajectory reconstruction, we were able to visualize differential motif accessibility for transcription factors INSM1, FOXO4, TCF4, GLIS3, and HIVEP2 between basal IHCs and OHCs. The trajectories were used to visualize differences between transcriptome- and chromatin-based identities of HCs during differentiation. Together, our findings support the observation that during development, dynamic changes of the chromatin accessibility landscape on average lag behind changes of the transcriptional landscape. In conclusion, this study provides a comprehensive analytical framework to analyze dynamic changes in the regulatory landscape of various cellular lineages that develop from a shared progenitor. This study will help to further the knowledge regarding sensory HC differentiation and maturation in the mammalian inner ear.

In Chapter 4, we employed the previously developed computational approach complemented with wet lab experiments to gain further biological insights into the role of RA in cochlear HC differentiation. To achieve this goal, single-cell multi-omics data from P2 and scRNA-seq datasets from two different time points, namely E12.5 and E14.5, were integrated. According to the previous publications, ectopic RA and pharmacologic blocking of RARA in organotypic cultures of the embryonic cochlea suggest that RA induces differentiation of cochlear HCs (Kelley et al. 1993, Raz and Kelley 1999). In order to investigate the specific molecular and cellular targets of RA signaling in the cochlea, we initially identified genes that

are regulated by RA and subsequently verified our findings through experimentation with organotypic cultures. Using an integrative approach, RARA was classified to function as transcriptional repressor in P2 HCs. Previous studies have considered the RAR-RXR heterodimer as repressive in the absence of the RA ligand (Weston et al. 2003). This notion is supported by experiments using *RARE-lacZ* reporters, which showed low or no RARE-reporter activity in postnatal organ of Corti (Kelley et al. 1993, Wang 2022), thus reinforcing the designation of RARA as a transcriptional repressor. Hence, these results indicate that the receptor functions as a transcriptional repressor and inhibits the expression of supporting cell specific genes in postnatal HCs when the ligand is absent. Conversely, binding of RA to RARA in the embryonic cochlea is likely to induce SC specific genes in prosensory progenitors. Specifically, we determined the downstream target genes of RARA by examining the gene regulatory network and observed that these genes possess potential RARA binding sites located near their transcription start sites, which were detected in accessible chromatin regions. With a focus on *Lfng* as a downstream target gene of RARA, we identified two direct repeats of RAR-RXR motifs in two putative regulatory elements at the *Lfng* locus in P2 supporting cells. These findings suggest that both RAR-RXR repeats can form active RAR response elements (Chatagnon et al. 2015, Mark et al. 2006). This study will provide insights into the mechanisms underlying sensory hair cell differentiation by elucidating the multifaceted functions of RARA and its associated cofactors in the mammalian inner ear. By identifying the downstream targets and cofactors associated with RA signaling, this study provides a foundation for future investigations into the potential to convert supporting cells into hair cells and ultimately regenerate hearing function in individuals with sensorineural hearing loss.

The studies conducted in this dissertation highlight both the potential and the challenges of using current single cell epigenomic and transcriptomic techniques to investigate the molecular mechanisms of mouse cochlear development. The ongoing refinement of experimental methods to examine molecular features will produce novel datasets that can be used to advance our understanding of various aspects of cochlear development in mice. By integrating these datasets with existing ones, we can gain insight into tonotopic organization during embryonic stages, elucidate the regulatory mechanisms governing the differentiation and maturation of auditory hair cells, and investigate the RA-mediated control of hair cell differentiation in the developing cochlea. Ultimately, these findings may inform the development of strategies to promote hearing regeneration.

Bibliography

Aibar, S., C. B. González-Blas, T. Moerman, V. A. Huynh-Thu, H. Imrichova, G. Hulselmans, F. Rambow, J. C. Marine, P. Geurts, J. Aerts, J. van den Oord, Z. K. Atak, J. Wouters & S. Aerts (2017) SCENIC: single-cell regulatory network inference and clustering. *Nat Methods,* 14**,** 1083-1086.

Aleksiūnienė, B., R. Matulevičiūtė, A. Matulevičienė, B. Burnytė, N. Krasovskaja, L. Ambrozaitytė, V. Mikštienė, V. Dirsė, A. Utkus & V. Kučinskas (2017) Opposite chromosome constitutions due to a familial translocation t(1;21)(q43;q22) in 2 cousins with development delay and congenital anomalies: A case report. *Medicine (Baltimore),* 96**,** e6521.

Alvarado, D. M., R. Veile, J. Speck, M. Warchol & M. Lovett (2009) Downstream targets of GATA3 in the vestibular sensory organs of the inner ear. *Dev Dyn,* 238**,** 3093-102.

Anniko, M. (1983) Cytodifferentiation of cochlear hair cells. *Am J Otolaryngol,* 4**,** 375-88.

Armand, E. J., J. Li, F. Xie, C. Luo & E. A. Mukamel (2021) Single-cell sequencing of brain cell transcriptomes and epigenomes. *Neuron,* 109**,** 11-26.

Arnold, K., A. Sarkar, M. A. Yram, J. M. Polo, R. Bronson, S. Sengupta, M. Seandel, N. Geijsen & K. Hochedlinger (2011) Sox2(+) adult stem and progenitor cells are important for tissue regeneration and survival of mice. *Cell Stem Cell,* 9**,** 317-29.

Ashburner, M., C. A. Ball, J. A. Blake, D. Botstein, H. Butler, J. M. Cherry, A. P. Davis, K. Dolinski, S. S. Dwight, J. T. Eppig, M. A. Harris, D. P. Hill, L. Issel-Tarver, A. Kasarskis, S. Lewis, J. C. Matese, J. E. Richardson, M. Ringwald, G. M. Rubin & G. Sherlock (2000) Gene ontology: tool for the unification of biology. The Gene Ontology Consortium. *Nat Genet,* 25**,** 25-9.

Basch, M. L., R. M. Brown, 2nd, H. I. Jen & A. K. Groves (2016a) Where hearing starts: the development of the mammalian cochlea. *J Anat,* 228**,** 233-54.

Basch, M. L., R. M. Brown, H. I. Jen, F. Semerci, F. Depreux, R. K. Edlund, H. Zhang, C. R. Norton, T. Gridley, S. E. Cole, A. Doetzlhofer, M. Maletic-Savatic, N. Segil & A. K. Groves (2016b) Fine-tuning of Notch signaling sets the boundary of the organ of Corti and establishes sensory cell fates. *Elife,* 5.

Basch, M. L., T. Ohyama, N. Segil & A. K. Groves (2011) Canonical Notch signaling is not necessary for prosensory induction in the mouse cochlea: insights from a conditional mutant of RBPjkappa. *J Neurosci,* 31**,** 8046-58.

Bendall, S. C., K. L. Davis, e.-A. Amir, M. D. Tadmor, E. F. Simonds, T. J. Chen, D. K. Shenfeld, G. P. Nolan & D. Pe'er (2014) Single-cell trajectory detection uncovers progression and regulatory coordination in human B cell development. *Cell,* 157**,** 714-25.

Berest, I., C. Arnold, A. Reyes-Palomares, G. Palla, K. D. Rasmussen, H. Giles, P. M. Bruch, W. Huber, S. Dietrich, K. Helin & J. B. Zaugg (2019) Quantification of Differential Transcription Factor Activity and Multiomics-Based Classification into Activators and Repressors: diffTF. *Cell Rep,* 29**,** 3147-3159.e12.

Bermingham-McDonogh, O., E. C. Oesterle, J. S. Stone, C. R. Hume, H. M. Huynh & T. Hayashi (2006) Expression of Prox1 during mouse cochlear development. *J Comp Neurol,* 496**,** 172-86.

Bok, J., S. Raft, K.-A. Kong, S. K. Koo, U. C. Dräger & D. K. Wu (2011a) Transient retinoic acid signaling confers anterior-posterior polarity to the inner ear. *Proceedings of the National Academy of Sciences,* 108**,** 161-166.

Bok, J., S. Raft, K. A. Kong, S. K. Koo, U. C. Dräger & D. K. Wu (2011b) Transient retinoic acid signaling confers anterior-posterior polarity to the inner ear. *Proc Natl Acad Sci U S A,* 108**,** 161-6.

Bok, J., C. Zenczak, C. H. Hwang & D. K. Wu (2013) Auditory ganglion source of Sonic hedgehog regulates timing of cell cycle exit and differentiation of mammalian cochlear hair cells. *Proc Natl Acad Sci U S A,* 110**,** 13869-74.

Buckiová, D. & J. Syka (2009) Calbindin and S100 protein expression in the developing inner ear in mice. *J Comp Neurol,* 513**,** 469-82.

Buenrostro, J. D., M. R. Corces, C. A. Lareau, B. Wu, A. N. Schep, M. J. Aryee, R. Majeti, H. Y. Chang & W. J. Greenleaf (2018) Integrated Single-Cell Analysis Maps the Continuous Regulatory Landscape of Human Hematopoietic Differentiation. *Cell,* 173**,** 1535-1548.e16.

Buenrostro, J. D., P. G. Giresi, L. C. Zaba, H. Y. Chang & W. J. Greenleaf (2013) Transposition of native chromatin for fast and sensitive epigenomic profiling of open chromatin, DNA-binding proteins and nucleosome position. *Nat Methods,* 10**,** 1213-8.

Buenrostro, J. D., B. Wu, H. Y. Chang & W. J. Greenleaf (2015) ATAC‐seq: a method for assaying chromatin accessibility genome‐wide. *Current protocols in molecular biology,* 109**,** 21.29. 1-21.29. 9.

Burns, J. C., M. C. Kelly, M. Hoa, R. J. Morell & M. W. Kelley (2015) Single-cell RNA-Seq resolves cellular complexity in sensory organs from the neonatal inner ear. *Nat Commun,* 6**,** 8557.

Cai, Q., R. R. Vethanayagam, S. Yang, J. Bard, J. Jamison, D. Cartwright, Y. Dong & B. H. Hu (2014) Molecular profile of cochlear immunity in the resident cells of the organ of Corti. *J Neuroinflammation,* 11**,** 173.

Cai, T., H. I. Jen, H. Kang, T. J. Klisch, H. Y. Zoghbi & A. K. Groves (2015) Characterization of the transcriptome of nascent hair cells and identification of direct targets of the Atoh1 transcription factor. *J Neurosci,* 35**,** 5870-83.

Cai, T., M. L. Seymour, H. Zhang, F. A. Pereira & A. K. Groves (2013) Conditional deletion of Atoh1 reveals distinct critical periods for survival and function of hair cells in the organ of Corti. *J Neurosci,* 33**,** 10110-22.

Chadha, S., A. Cieza & K. Reyes (2018) Public health approach to hearing across the life course: a call-for-papers. *Bulletin of the World Health Organization,* 96**,** 592.

Chadha, S., K. Kamenov & A. Cieza (2021) The world report on hearing, 2021. *Bulletin of the World Health Organization,* 99**,** 242.

Chatagnon, A., P. Veber, V. Morin, J. Bedo, G. Triqueneaux, M. Sémon, V. Laudet, F. d'Alché-Buc & G. Benoit (2015) RAR/RXR binding dynamics distinguish pluripotency from differentiation associated cis-regulatory elements. *Nucleic Acids Res,* 43**,** 4833-54.

Chen, P., J. E. Johnson, H. Y. Zoghbi & N. Segil (2002) The role of Math1 in inner ear development: Uncoupling the establishment of the sensory primordium from hair cell fate determination. *Development,* 129**,** 2495-505.

Chen, P. & N. Segil (1999) p27(Kip1) links cell proliferation to morphogenesis in the developing organ of Corti. *Development,* 126**,** 1581-90.

Chen, X., Y. Yang, L. Luo, L. Xu, B. Liu, G. Jiang, X. Hu, Y. Zeng & Z. Wang (2020) An iPSC line (TYWHSTi002-A) derived from a patient with Pendred syndrome caused by compound heterozygous mutations in the SLC26A4 gene. *Stem Cell Res,* 47**,** 101919.

Cheng, C., Y. Wang, L. Guo, X. Lu, W. Zhu, W. Muhammad, L. Zhang, L. Lu, J. Gao, M. Tang, F. Chen, X. Gao, H. Li & R. Chai (2019) Age-related transcriptome changes in Sox2+ supporting cells in the mouse cochlea. *Stem Cell Res Ther,* 10**,** 365.

Chessum, L., M. S. Matern, M. C. Kelly, S. L. Johnson, Y. Ogawa, B. Milon, M. McMurray, E. C. Driver, A. Parker, Y. Song, G. Codner, C. T. Esapa, J. Prescott, G. Trent, S. Wells, A. K. Dragich, G. I. Frolenkov, M. W. Kelley, W. Marcotti, S. D. M. Brown, R. Elkon, M. R. Bowl & R. Hertzano (2018) Helios is a key transcriptional regulator of outer hair cell maturation. *Nature,* 563**,** 696-700.

Chung, J. W., H. H. Kang, J. E. Shin & J. U. Kim (2004) Accumulation of hypoxia-inducible factor-1alpha in mouse inner ear by noise stimulation. *Neuroreport,* 15**,** 2353-6.

Cochain, C., E. Vafadarnejad, P. Arampatzi, J. Pelisek, H. Winkels, K. Ley, D. Wolf, A. E. Saliba & A. Zernecke (2018) Single-Cell RNA-Seq Reveals the Transcriptional Landscape and Heterogeneity of Aortic Macrophages in Murine Atherosclerosis. *Circ Res,* 122**,** 1661-1674.

Consortium, G. O. (2021) The Gene Ontology resource: enriching a GOld mine. *Nucleic Acids Res,* 49**,** D325-D334.

Corti, A. 1851. Recherches sur l'organe de l'ouïe des mammiferes.

Cunningham, L. L. & D. L. Tucci (2017) Hearing loss in adults. *New England Journal of Medicine,* 377**,** 2465-2473.

Cunningham, T. J. & G. Duester (2015) Mechanisms of retinoic acid signalling and its roles in organ and limb development. *Nat Rev Mol Cell Biol,* 16**,** 110-23.

Davis, R. L. (2003) Gradients of neurotrophins, ion channels, and tuning in the cochlea. *Neuroscientist,* 9**,** 311-6.

de Winter, C. F., M. Baas, E. K. Bijlsma, J. van Heukelingen, S. Routledge & R. C. Hennekam (2016) Phenotype and natural history in 101 individuals with Pitt-Hopkins syndrome through an internet questionnaire system. *Orphanet J Rare Dis,* 11**,** 37.

Di Minin, G., M. Holzner, A. Grison, C. E. Dumeau, W. Chan, A. Monfort, L. A. Jerome-Majewska, H. Roelink & A. Wutz (2022) TMED2 binding restricts SMO to the ER and Golgi compartments. *PLoS Biol,* 20**,** e3001596.

Diaz, G. H. & S. Heller (2021) Fluorescent. *STAR Protoc,* 2**,** 100711.

Dimitri, P., J. T. Warner, J. A. Minton, A. M. Patch, S. Ellard, A. T. Hattersley, S. Barr, D. Hawkes, J. K. Wales & J. W. Gregory (2011) Novel GLIS3 mutations demonstrate an extended multisystem phenotype. *Eur J Endocrinol,* 164**,** 437-43.

Doetzlhofer, A., M. L. Basch, T. Ohyama, M. Gessler, A. K. Groves & N. Segil (2009) Hey2 regulation by FGF provides a Notch-independent mechanism for maintaining pillar cell fate in the organ of Corti. *Dev Cell,* 16**,** 58-69.

Driver, E. C., L. Sillers, T. M. Coate, M. F. Rose & M. W. Kelley (2013) The Atoh1-lineage gives rise to hair cells and supporting cells within the mammalian cochlea. *Developmental biology,* 376**,** 86-98.

Duester, G. (2008) Retinoic acid synthesis and signaling during early organogenesis. *Cell,* 134**,** 921-31.

Durruthy-Durruthy, R., A. Gottlieb, B. H. Hartman, J. Waldhaus, R. D. Laske, R. Altman & S. Heller (2014) Reconstruction of the mouse otocyst and early neuroblast lineage at single-cell resolution. *Cell,* 157**,** 964-78.

Ebeid, M. & S. H. Huh (2020) Mesenchymal ETV transcription factors regulate cochlear length. *Hear Res,* 396**,** 108039.

Ehret, G. & M. Frankenreiter (1977) Quantitative analysis of cochlear structures in the house mouse in relation to mechanisms of acoustical information processing. 122**,** 65–85.

El Shahawy, M., C. G. Reibring, K. Hallberg, C. L. Neben, P. Marangoni, B. D. Harfe, O. D. Klein, A. Linde & A. Gritli-Linde (2019) Sonic Hedgehog Signaling Is Required for Cyp26 Expression during Embryonic Development. *Int J Mol Sci,* 20.

Elkon, R., B. Milon, L. Morrison, M. Shah, S. Vijayakumar, M. Racherla, C. C. Leitch, L. Silipino, S. Hadi, M. Weiss-Gayet, E. Barras, C. D. Schmid, A. Ait-Lounis, A. Barnes, Y. Song, D. J. Eisenman, E. Eliyahu, G. I. Frolenkov, S. E. Strome, B. Durand, N. A. Zaghloul, S. M. Jones, W. Reith & R. Hertzano (2015) RFX transcription factors are essential for hearing in mice. *Nat Commun,* 6**,** 8549.

Ellwanger, D. C., M. Scheibinger, R. A. Dumont, P. G. Barr-Gillespie & S. Heller (2018) Transcriptional Dynamics of Hair-Bundle Morphogenesis Revealed with CellTrails. *Cell Rep,* 23**,** 2901-2914.e13.

Fang, R., S. Preissl, X. Hou, J. Lucero, X. Wang, A. Motamedi, A. Shiau, E. Mukamel, Y. Zhang, M. Behrens, J. Ecker & B. Ren (2019) Fast and Accurate Clustering of Single Cell Epigenomes Reveals *Cis*-Regulatory Elements in Rare Cell Types. *Biorxiv doi: 10.1101/615179*.

Feng, L., R. E. Hernandez, J. S. Waxman, D. Yelon & C. B. Moens (2010) Dhrs3a regulates retinoic acid biosynthesis through a feedback inhibition mechanism. *Dev Biol,* 338**,** 1-14.

Ferguson, M. A., P. T. Kitterick, L. Y. Chong, M. Edmondson‐Jones, F. Barker & D. J. Hoare (2017) Hearing aids for mild to moderate hearing loss in adults. *Cochrane Database of Systematic Reviews*.

Fettiplace, R. (2017) Hair Cell Transduction, Tuning, and Synaptic Transmission in the Mammalian Cochlea. *Compr Physiol,* 7**,** 1197-1227.

Fornes, O., J. A. Castro-Mondragon, A. Khan, R. van der Lee, X. Zhang, P. A. Richmond, B. P. Modi, S. Correard, M. Gheorghe, D. Baranašić, W. Santana-Garcia, G. Tan, J. Chèneby, B. Ballester, F. Parcy, A. Sandelin, B. Lenhard, W. W. Wasserman & A. Mathelier (2020) JASPAR 2020: update of the open-access database of transcription factor binding profiles. *Nucleic Acids Res,* 48**,** D87-D92.

Frucht, C. S., M. Uduman, S. H. Kleinstein, J. Santos-Sacchi & D. S. Navaratnam (2011) Gene expression gradients along the tonotopic axis of the chicken auditory epithelium. *J Assoc Res Otolaryngol,* 12**,** 423-35.

Fuhrmann, D., M. Mernberger, A. Nist, T. Stiewe & H. P. Elsässer (2018) Miz1 Controls Schwann Cell Proliferation via H3K36. *J Neurosci,* 38**,** 858-877.

Gnedeva, K. & A. J. Hudspeth (2015) SoxC transcription factors are essential for the development of the inner ear. *Proc Natl Acad Sci U S A,* 112**,** 14066-71.

Golden, E. J., A. Benito-Gonzalez & A. Doetzlhofer (2015) The RNA-binding protein LIN28B regulates developmental timing in the mammalian cochlea. *Proc Natl Acad Sci U S A,* 112**,** E3864-73.

Gory-Fauré, S., M. H. Prandini, H. Pointu, V. Roullot, I. Pignot-Paintrand, M. Vernet & P. Huber (1999) Role of vascular endothelial-cadherin in vascular morphogenesis. *Development,* 126**,** 2093-102.

Grant, C. E., T. L. Bailey & W. S. Noble (2011) FIMO: scanning for occurrences of a given motif. *Bioinformatics,* 27**,** 1017-8.

Groves, A. K. (2010) The challenge of hair cell regeneration. *Experimental Biology and Medicine,* 235**,** 434-446.

Guo, M., E. L. Bao, M. Wagner, J. A. Whitsett & Y. Xu (2017) SLICE: determining cell differentiation and lineage based on single cell entropy. *Nucleic Acids Res,* 45**,** e54.

Hao, Y., S. Hao, E. Andersen-Nissen, W. M. Mauck, S. Zheng, A. Butler, M. J. Lee, A. J. Wilk, C. Darby, M. Zager, P. Hoffman, M. Stoeckius, E. Papalexi, E. P. Mimitou, J. Jain, A. Srivastava, T. Stuart, L. M. Fleming, B. Yeung, A. J. Rogers, J. M. McElrath, C. A. Blish, R. Gottardo, P. Smibert & R. Satija (2021) Integrated analysis of multimodal single-cell data. *Cell,* 184**,** 3573-3587.e29.

Hartman, B. H., O. Basak, B. R. Nelson, V. Taylor, O. Bermingham-McDonogh & T. A. Reh (2009) Hes5 expression in the postnatal and adult mouse inner ear and the drug-damaged cochlea. *J Assoc Res Otolaryngol,* 10**,** 321-40.

Hartman, B. H., R. Durruthy-Durruthy, R. D. Laske, S. Losorelli & S. Heller (2015) Identification and characterization of mouse otic sensory lineage genes. *Front Cell Neurosci,* 9**,** 79.

Hayashi, T., C. A. Ray, C. Younkins & O. Bermingham-McDonogh (2010) Expression patterns of FGF receptors in the developing mammalian cochlea. *Dev Dyn,* 239**,** 1019-26.

Hellström, A. R., B. Watt, S. S. Fard, D. Tenza, P. Mannström, K. Narfström, B. Ekesten, S. Ito, K. Wakamatsu, J. Larsson, M. Ulfendahl, K. Kullander, G. Raposo, S. Kerje, F.

Hallböök, M. S. Marks & L. Andersson (2011) Inactivation of Pmel alters melanosome shape but has only a subtle effect on visible pigmentation. *PLoS Genet,* 7**,** e1002285.

Hertzano, R., A. A. Dror, M. Montcouquiol, Z. M. Ahmed, B. Ellsworth, S. Camper, T. B. Friedman, M. W. Kelley & K. B. Avraham (2007) Lhx3, a LIM domain transcription factor, is regulated by Pou4f3 in the auditory but not in the vestibular system. *Eur J Neurosci,* 25**,** 999-1005.

Hishiya, A., S. Iemura, T. Natsume, S. Takayama, K. Ikeda & K. Watanabe (2006) A novel ubiquitin-binding protein ZNF216 functioning in muscle atrophy. *EMBO J,* 25**,** 554-64.

Homem, C. C. & J. A. Knoblich (2012) Drosophila neuroblasts: a model for stem cell biology. *Development,* 139**,** 4297-310.

Hrdlickova, R., M. Toloue & B. Tian (2017) RNA-Seq methods for transcriptome analysis. *Wiley Interdisciplinary Reviews: RNA,* 8**,** e1364.

Hu, G., K. Cui, D. Fang, S. Hirose, X. Wang, D. Wangsa, W. Jin, T. Ried, P. Liu, J. Zhu, E. V. Rothenberg & K. Zhao (2018) Transformation of Accessible Chromatin and 3D Nucleome Underlies Lineage Commitment of Early T Cells. *Immunity,* 48**,** 227-242.e8.

Huang, M., C. Sage, Y. Tang, S. G. Lee, M. Petrillo, P. W. Hinds & Z. Y. Chen (2011) Overlapping and distinct pRb pathways in the mammalian auditory and vestibular organs. *Cell Cycle,* 10**,** 337-51.

Huynh-Thu, V. A., A. Irrthum, L. Wehenkel & P. Geurts (2010) Inferring regulatory networks from expression data using tree-based methods. *PLoS One,* 5.

Islam, S., U. Kjällquist, A. Moliner, P. Zajac, J.-B. Fan, P. Lönnerberg & S. Linnarsson (2011) Characterization of the single-cell transcriptional landscape by highly multiplex RNA-seq. *Genome research,* 21**,** 1160-1167.

Janesick, A., T. T. Nguyen, K. Aisaki, K. Igarashi, S. Kitajima, R. A. Chandraratna, J. Kanno & B. Blumberg (2014) Active repression by RARγ signaling is required for vertebrate axial elongation. *Development,* 141**,** 2260-70.

Jessen, K. R. & R. Mirsky (2019) Schwann Cell Precursors; Multipotent Glial Cells in Embryonic Nerves. *Front Mol Neurosci,* 12**,** 69.

Jovic, D., X. Liang, H. Zeng, L. Lin, F. Xu & Y. Luo (2022) Single-cell RNA sequencing technologies and applications: A brief overview. *Clinical and Translational Medicine,* 12**,** e694.

Kashyap, V. & L. J. Gudas (2010) Epigenetic regulatory mechanisms distinguish retinoic acid-mediated transcriptional responses in stem cells and fibroblasts. *J Biol Chem,* 285**,** 14534-48.

Kelley, M. W., X. M. Xu, M. A. Wagner, M. E. Warchol & J. T. Corwin (1993) The developing organ of Corti contains retinoic acid and forms supernumerary hair cells in response to exogenous retinoic acid in culture. *Development,* 119**,** 1041-53.

Kiernan, A. E., A. L. Pelling, K. K. Leung, A. S. Tang, D. M. Bell, C. Tease, R. Lovell-Badge, K. P. Steel & K. S. Cheah (2005) Sox2 is required for sensory organ development in the mammalian inner ear. *Nature,* 434**,** 1031-5.

Kitajiri, S. I., M. Furuse, K. Morita, Y. Saishin-Kiuchi, H. Kido, J. Ito & S. Tsukita (2004) Expression patterns of claudins, tight junction adhesion molecules, in the inner ear. *Hear Res,* 187**,** 25-34.

Klemm, S. L., Z. Shipony & W. J. Greenleaf (2019a) Chromatin accessibility and the regulatory epigenome. *Nat Rev Genet,* 20**,** 207-220.

Klemm, S. L., Z. Shipony & W. J. Greenleaf (2019b) Chromatin accessibility and the regulatory epigenome. *Nature Reviews Genetics,* 20**,** 207-220.

Kolla, L., M. C. Kelly, Z. F. Mann, A. Anaya-Rocha, K. Ellis, A. Lemons, A. T. Palermo, K. S. So, J. C. Mays, J. Orvis, J. C. Burns, R. Hertzano, E. C. Driver & M. W. Kelley (2020) Characterization of the development of the mouse cochlear epithelium at the single cell level. *Nat Commun,* 11**,** 2389.

Koo, H. Y., M. A. Kim, H. Min, J. Y. Hwang, M. Prajapati-DiNubila, K. S. Kim, M. M. Matzuk, J. W. Park, A. Doetzlhofer, U. K. Kim & J. Bok (2023) Follistatin regulates the specification of the apical cochlea responsible for low-frequency hearing in mammals. *Proc Natl Acad Sci U S A,* 120**,** e2213099120.

Kulakovskiy, I. V., Y. A. Medvedeva, U. Schaefer, A. S. Kasianov, I. E. Vorontsov, V. B. Bajic & V. J. Makeev (2013) HOCOMOCO: a comprehensive collection of human transcription factor binding sites models. *Nucleic Acids Res,* 41**,** D195-202.

Kullback, S. & R. A. Leibler On Information and Sufficiency.

Kwan, K. Y., J. Shen & D. P. Corey (2015) C-MYC transcriptionally amplifies SOX2 target genes to regulate self-renewal in multipotent otic progenitor cells. *Stem Cell Reports,* 4**,** 47-60.

Kwan, T., P. M. White & N. Segil (2009) Development and regeneration of the inner ear: Cell cycle control and differentiation of sensory progenitors. *Annals of the New York Academy of Sciences,* 1170**,** 28-33.

Lanford, P. J., Y. Lan, R. Jiang, C. Lindsell, G. Weinmaster, T. Gridley & M. W. Kelley (1999) Notch signalling pathway mediates hair cell development in mammalian cochlea. *Nat Genet,* 21**,** 289-92.

Latchman, D. S. (1997) Transcription factors: an overview. *The international journal of biochemistry & cell biology,* 29**,** 1305-1312.

Lee, T. I. & R. A. Young (2000) Transcription of eukaryotic protein-coding genes. *Annual review of genetics,* 34**,** 77-137.

Lee, Y.-S., F. Liu & N. Segil (2006a) A morphogenetic wave of p27Kip1 transcription directs cell cycle exit during organ of Corti development.

Lee, Y. S., F. Liu & N. Segil (2006b) A morphogenetic wave of p27Kip1 transcription directs cell cycle exit during organ of Corti development. *Development,* 133**,** 2817-26.

Lelli, A., Y. Asai, A. Forge, J. R. Holt & G. S. Géléoc (2009) Tonotopic gradient in the developmental acquisition of sensory transduction in outer hair cells of the mouse cochlea. *J Neurophysiol,* 101**,** 2961-73.

Li, Y., H. Liu, C. L. Barta, P. D. Judge, L. Zhao, W. J. Zhang, S. Gong, K. W. Beisel & D. Z. He (2016) Transcription Factors Expressed in Mouse Cochlear Inner and Outer Hair Cells. *PLoS One,* 11**,** e0151291.

Li, Y., H. Liu, K. P. Giffen, L. Chen, K. W. Beisel & D. Z. Z. He (2018) Transcriptomes of cochlear inner and outer hair cells from adult mice. *Sci Data,* 5**,** 180199.

Li, Y., Y. Liu, H. Yang, T. Zhang, K. Naruse & Q. Tu (2020) Dynamic transcriptional and chromatin accessibility landscape of medaka embryogenesis. *Genome Res,* 30**,** 924-937.

Li, Z., M. H. Schulz, T. Look, M. Begemann, M. Zenke & I. G. Costa (2019a) Identification of transcription factor binding sites using ATAC-seq. *Genome Biol,* 20**,** 45.

Li, Z., M. H. Schulz, T. Look, M. Begemann, M. Zenke & I. G. Costa (2019b) Identification of transcription factor binding sites using ATAC-seq. *Genome biology,* 20**,** 1-21.

Lilleväli, K., T. Matilainen, A. Karis & M. Salminen (2004) Partially overlapping expression of Gata2 and Gata3 during inner ear development. *Dev Dyn,* 231**,** 775-81.

Liu, X. & D. Yan (2007) Ageing and hearing loss. *The Journal of Pathology: A Journal of the Pathological Society of Great Britain and Ireland,* 211**,** 188-197.

Liu, Z., T. Owen, L. Zhang & J. Zuo (2010) Dynamic expression pattern of Sonic hedgehog in developing cochlear spiral ganglion neurons. *Dev Dyn,* 239**,** 1674-83.

Lopez-Juarez, A., H. Lahlou, C. Ripoll, Y. Cazals, J. M. Brezun, Q. Wang, A. Edge & A. Zine (2019) Engraftment of Human Stem Cell-Derived Otic Progenitors in the Damaged Cochlea. *Mol Ther,* 27**,** 1101-1113.

Löwenheim, H., D. N. Furness, J. Kil, C. Zinn, K. Gültig, M. L. Fero, D. Frost, A. W. Gummer, J. M. Roberts, E. W. Rubel, C. M. Hackney & H. P. Zenner (1999) Gene disruption of p27(Kip1) allows cell proliferation in the postnatal and adult organ of corti. *Proc Natl Acad Sci U S A,* 96**,** 4084-8.

Luo, X. J., M. Deng, X. Xie, L. Huang, H. Wang, L. Jiang, G. Liang, F. Hu, R. Tieu, R. Chen & L. Gan (2013) GATA3 controls the specification of prosensory domain and neuronal survival in the mouse cochlea. *Hum Mol Genet,* 22**,** 3609-23.

Luo, Z., Y. Du, S. Li, H. Zhang, M. Shu, D. Zhang, S. He, G. Wang, F. Lu & Z. Liu (2022) Three distinct. *Proc Natl Acad Sci U S A,* 119**,** e2119850119.

Maass, J. C., R. Gu, T. Cai, Y. W. Wan, S. C. Cantellano, J. S. Asprer, H. Zhang, H. I. Jen, R. K. Edlund, Z. Liu & A. K. Groves (2016) Transcriptomic Analysis of Mouse Cochlear Supporting Cell Maturation Reveals Large-Scale Changes in Notch Responsiveness Prior to the Onset of Hearing. *PLoS One,* 11**,** e0167286.

Maden, M. (2007) Retinoic acid in the development, regeneration and maintenance of the nervous system. *Nat Rev Neurosci,* 8**,** 755-65.

Madisen, L., T. A. Zwingman, S. M. Sunkin, S. W. Oh, H. A. Zariwala, H. Gu, L. L. Ng, R. D. Palmiter, M. J. Hawrylycz, A. R. Jones, E. S. Lein & H. Zeng (2010) A robust and high-throughput Cre reporting and characterization system for the whole mouse brain. *Nat Neurosci,* 13**,** 133-40.

Maeda, Y., S. Kariya, K. Uraguchi, J. Takahara, S. Fujimoto, A. Sugaya & K. Nishizaki (2020) Immediate changes in transcription factors and synaptic transmission in the cochlea following acoustic trauma: A gene transcriptome study. *Neurosci Res*.

Mann, Z. F. & M. W. Kelley (2011a) Development of tonotopy in the auditory periphery. *Hearing research,* 276**,** 2-15.

Mann, Z. F. & M. W. Kelley (2011b) Development of tonotopy in the auditory periphery. *Hear Res,* 276**,** 2-15.

Mann, Z. F. & M. W. J. H. r. Kelley (2011c) Development of tonotopy in the auditory periphery. 276**,** 2-15.

Mann, Z. F., B. R. Thiede, W. Chang, J. B. Shin, H. L. May-Simera, M. Lovett, J. T. Corwin & M. W. Kelley (2014) A gradient of Bmp7 specifies the tonotopic axis in the developing inner ear. *Nat Commun,* 5**,** 3839.

Marinov, G. K., B. A. Williams, K. McCue, G. P. Schroth, J. Gertz, R. M. Myers & B. J. Wold (2014) From single-cell to cell-pool transcriptomes: stochasticity in gene expression and RNA splicing. *Genome research,* 24**,** 496-510.

Mark, M., N. B. Ghyselinck & P. Chambon (2006) Function of retinoid nuclear receptors: lessons from genetic and pharmacological dissections of the retinoic acid signaling pathway during mouse embryogenesis. *Annu Rev Pharmacol Toxicol,* 46**,** 451-80.

Menendez, L., T. Trecek, S. Gopalakrishnan, L. Tao, A. L. Markowitz, H. V. Yu, X. Wang, J. Llamas, C. Huang & J. Lee (2020a) Generation of inner ear hair cells by direct lineage conversion of primary somatic cells. *elife,* 9**,** e55249.

Menendez, L., T. Trecek, S. Gopalakrishnan, L. Tao, A. L. Markowitz, H. V. Yu, X. Wang, J. Llamas, C. Huang, J. Lee, R. Kalluri, J. Ichida & N. Segil (2020b) Generation of inner ear hair cells by direct lineage conversion of primary somatic cells. *Elife,* 9.

Mezger, A., S. Klemm, I. Mann, K. Brower, A. Mir, M. Bostick, A. Farmer, P. Fordyce, S. Linnarsson & W. Greenleaf (2018) High-throughput chromatin accessibility profiling at single-cell resolution. *Nat Commun,* 9**,** 3647.

Miyoshi, T., T. Yamaguchi, K. Ogita, Y. Tanaka, K. I. Ishibashi, H. Ito, T. Kobayashi, T. Nakagawa, J. Ito, K. Omori & N. Yamamoto (2017) Quantitative Analysis of Aquaporin Expression Levels during the Development and Maturation of the Inner Ear. *J Assoc Res Otolaryngol,* 18**,** 247-261.

Moore, B. C. 2012. *An introduction to the psychology of hearing*. Brill.

Morita, K., H. Sasaki, M. Furuse & S. Tsukita (1999) Endothelial claudin: claudin-5/TMVCF constitutes tight junction strands in endothelial cells. *J Cell Biol,* 147**,** 185-94.

Morsli, H., D. Choo, A. Ryan, R. Johnson & D. K. Wu (1998) Development of the mouse inner ear and origin of its sensory organs. *J Neurosci,* 18**,** 3327-35.

Mukherjea, D., L. P. Rybak, K. E. Sheehan, T. Kaur, V. Ramkumar, S. Jajoo & S. Sheth (2011) The design and screening of drugs to prevent acquired sensorineural hearing loss. *Expert opinion on drug discovery,* 6**,** 491-505.

Mutai, H., K. Wasano, Y. Momozawa, Y. Kamatani, F. Miya, S. Masuda, N. Morimoto, K. Nara, S. Takahashi, T. Tsunoda, K. Homma, M. Kubo & T. Matsunaga (2020) Variants encoding a restricted carboxy-terminal domain of SLC12A2 cause hereditary hearing loss in humans. *PLoS Genet,* 16**,** e1008643.

Nagalakshmi, U., K. Waern & M. Snyder (2010) RNA‐Seq: a method for comprehensive transcriptome analysis. *Current protocols in molecular biology,* 89**,** 4.11. 1-4.11. 13.

Nawy, T. (2014) Single-cell sequencing. *Nature methods,* 11**,** 18-18.

Negrete, J. & A. C. Oates (2021) Towards a physical understanding of developmental patterning. *Nat Rev Genet,* 22**,** 518-531.

Niederreither, K., J. Vermot, V. Fraulob, P. Chambon & P. Dolle (2002) Retinaldehyde dehydrogenase 2 (RALDH2)- independent patterns of retinoic acid synthesis in the mouse embryo. *Proc Natl Acad Sci U S A,* 99**,** 16111-6.

Novitch, B. G., H. Wichterle, T. M. Jessell & S. Sockanathan (2003) A requirement for retinoic acid-mediated transcriptional activation in ventral neural patterning and motor neuron specification. *Neuron,* 40**,** 81-95.

Ohyama, T., M. L. Basch, Y. Mishina, K. M. Lyons, N. Segil & A. K. Groves (2010) BMP signaling is necessary for patterning the sensory and nonsensory regions of the developing mammalian cochlea. *J Neurosci,* 30**,** 15044-51.

Ono, K., J. Keller, O. López Ramírez, A. González Garrido, O. A. Zobeiri, H. H. V. Chang, S. Vijayakumar, A. Ayiotis, G. Duester, C. C. Della Santina, S. M. Jones, K. E. Cullen, R. A. Eatock & D. K. Wu (2020a) Retinoic acid degradation shapes zonal development of vestibular organs and sensitivity to transient linear accelerations. *Nat Commun,* 11**,** 63.

Ono, K., L. L. Sandell, P. A. Trainor & D. K. Wu (2020b) Retinoic acid synthesis and autoregulation mediate zonal patterning of vestibular organs and inner ear morphogenesis. *Development,* 147.

Orchard, P., Y. Kyono, J. Hensley, J. O. Kitzman & S. C. J. Parker (2020) Quantification, Dynamic Visualization, and Validation of Bias in ATAC-Seq Data with ataqv. *Cell Syst,* 10**,** 298-306.e4.

Organization, W. H. 2021. *World report on hearing*. World Health Organization.

Packer, J. & C. Trapnell (2018) Single-cell multi-omics: an engine for new quantitative models of gene regulation. *Trends in Genetics,* 34**,** 653-665.

Packer, J. S., Q. Zhu, C. Huynh, P. Sivaramakrishnan, E. Preston, H. Dueck, D. Stefanik, K. Tan, C. Trapnell, J. Kim, R. H. Waterston & J. I. Murray (2019) A lineage-resolved molecular atlas of. *Science,* 365.

Pauley, S., T. J. Wright, U. Pirvola, D. Ornitz, K. Beisel & B. Fritzsch (2003) Expression and function of FGF10 in mammalian inner ear development. *Dev Dyn,* 227**,** 203-15.

Perl, K., R. Shamir & K. B. Avraham (2018) Computational analysis of mRNA expression profiling in the inner ear reveals candidate transcription factors associated with proliferation, differentiation, and deafness. *Hum Genomics,* 12**,** 30.

Phippard, D., A. Heydemann, M. Lechner, L. Lu, D. Lee, T. Kyin & E. B. Crenshaw (1998) Changes in the subcellular localization of the Brn4 gene product precede mesenchymal remodeling of the otic capsule. *Hear Res,* 120**,** 77-85.

Plack, C. J. 2018. *The sense of hearing*. Routledge.

Pliner, H. A., J. S. Packer, J. L. McFaline-Figueroa, D. A. Cusanovich, R. M. Daza, D. Aghamirzaie, S. Srivatsan, X. Qiu, D. Jackson, A. Minkina, A. C. Adey, F. J. Steemers, J. Shendure & C. Trapnell (2018) Cicero Predicts cis-Regulatory DNA Interactions from Single-Cell Chromatin Accessibility Data. *Mol Cell,* 71**,** 858-871.e8.

Prajapati-DiNubila, M., A. Benito-Gonzalez, E. J. Golden, S. Zhang & A. Doetzlhofer (2019) A counter gradient of Activin A and follistatin instructs the timing of hair cell differentiation in the murine cochlea. *Elife,* 8.

Probst, S., C. Kraemer, P. Demougin, R. Sheth, G. R. Martin, H. Shiratori, H. Hamada, D. Iber, R. Zeller & A. Zuniga (2011) SHH propagates distal limb bud development by enhancing CYP26B1-mediated retinoic acid clearance via AER-FGF signalling. *Development,* 138**,** 1913-23.

Qiu, X., A. Hill, J. Packer, D. Lin, Y. A. Ma & C. Trapnell (2017a) Single-cell mRNA quantification and differential analysis with Census. *Nat Methods,* 14**,** 309-315.

Qiu, X., Q. Mao, Y. Tang, L. Wang, R. Chawla, H. A. Pliner & C. Trapnell (2017b) Reversed graph embedding resolves complex single-cell trajectories. *Nat Methods,* 14**,** 979-982.

Radde-Gallwitz, K., L. Pan, L. Gan, X. Lin, N. Segil & P. Chen (2004) Expression of Islet1 marks the sensory and neuronal lineages in the mammalian inner ear. *J Comp Neurol,* 477**,** 412-21.

Raz, Y. & M. W. Kelley (1999) Retinoic acid signaling is necessary for the development of the organ of Corti. *Dev Biol,* 213**,** 180-93.

Ribes, V., Z. Wang, P. Dollé & K. Niederreither (2006) Retinaldehyde dehydrogenase 2 (RALDH2)-mediated retinoic acid synthesis regulates early mouse embryonic forebrain development by controlling FGF and sonic hedgehog signaling. *Development,* 133**,** 351-61.

Roeder, R. G. (1996) The role of general initiation factors in transcription by RNA polymerase II. *Trends in biochemical sciences,* 21**,** 327-335.

Romand, R., T. Kondo, V. Fraulob, M. Petkovich, P. Dollé & E. Hashino (2006) Dynamic expression of retinoic acid-synthesizing and -metabolizing enzymes in the developing mouse inner ear. *J Comp Neurol,* 496**,** 643-54.

Rose, M. F., J. Ren, K. A. Ahmad, H. T. Chao, T. J. Klisch, A. Flora, J. J. Greer & H. Y. Zoghbi (2009) Math1 is essential for the development of hindbrain neurons critical for perinatal breathing. *Neuron,* 64**,** 341-54.

Rossini, B. A. A., N. d. O. Penido, M. S. L. Munhoz, E. A. Bogaz & R. S. Curi (2017) Sudden sensorioneural hearing loss and autoimmune systemic diseases. *International Archives of Otorhinolaryngology,* 21**,** 213-223.

Saliba, A.-E., A. J. Westermann, S. A. Gorski & J. Vogel (2014) Single-cell RNA-seq: advances and future challenges. *Nucleic acids research,* 42**,** 8845-8860.

Sanz, C., Y. León, S. Cañón, L. Alvarez, F. Giraldez & I. Varela-Nieto (1999) Pattern of expression of the jun family of transcription factors during the early development of the inner ear: implications in apoptosis. *J Cell Sci,* 112 (Pt 22)**,** 3967-74.

Schacht, J., A. E. Talaska & L. P. Rybak (2012) Cisplatin and aminoglycoside antibiotics: hearing loss and its prevention. *The Anatomical Record: Advances in Integrative Anatomy and Evolutionary Biology,* 295**,** 1837-1850.

Scheffer, D. I., J. Shen, D. P. Corey & Z. Y. Chen (2015) Gene Expression by Mouse Inner Ear Hair Cells during Development. *J Neurosci,* 35**,** 6366-80.

Schep, A. N., B. Wu, J. D. Buenrostro & W. J. Greenleaf (2017) chromVAR: inferring transcription-factor-associated accessibility from single-cell epigenomic data. *Nat Methods,* 14**,** 975-978.

Schilling, T. F., Q. Nie & A. D. Lander (2012) Dynamics and precision in retinoic acid morphogen gradients. *Curr Opin Genet Dev,* 22**,** 562-9.

Schindelin, J., I. Arganda-Carreras, E. Frise, V. Kaynig, M. Longair, T. Pietzsch, S. Preibisch, C. Rueden, S. Saalfeld, B. Schmid, J. Y. Tinevez, D. J. White, V. Hartenstein, K. Eliceiri, P. Tomancak & A. Cardona (2012) Fiji: an open-source platform for biological-image analysis. *Nat Methods,* 9**,** 676-82.

Schneider, R. A., D. Hu, J. L. Rubenstein, M. Maden & J. A. Helms (2001) Local retinoid signaling coordinates forebrain and facial morphogenesis by maintaining FGF8 and SHH. *Development,* 128**,** 2755-67.

Shabalina, S. A. & N. A. Spiridonov (2004) The mammalian transcriptome and the function of non-coding DNA sequences. *Genome Biol,* 5**,** 105.

Shen, J. & C. A. Walsh (2005) Targeted disruption of Tgif, the mouse ortholog of a human holoprosencephaly gene, does not result in holoprosencephaly in mice. *Mol Cell Biol,* 25**,** 3639-47.

Shibata, M., K. Pattabiraman, B. Lorente-Galdos, D. Andrijevic, S. K. Kim, N. Kaur, S. K. Muchnik, X. Xing, G. Santpere, A. M. M. Sousa & N. Sestan (2021) Regulation of prefrontal patterning and connectivity by retinoic acid. *Nature,* 598**,** 483-488.

Simonoska, R., A. E. Stenberg, M. Duan, K. Yakimchuk, A. Fridberger, L. Sahlin, J. A. Gustafsson & M. Hultcrantz (2009) Inner ear pathology and loss of hearing in estrogen receptor-beta deficient mice. *J Endocrinol,* 201**,** 397-406.

Sockanathan, S. & T. M. Jessell (1998) Motor neuron-derived retinoid signaling specifies the subtype identity of spinal motor neurons. *Cell,* 94**,** 503-14.

Son, E. J., J.-H. Ma, H. Ankamreddy, J.-O. Shin, J. Y. Choi, D. K. Wu & J. Bok (2015a) Conserved role of Sonic Hedgehog in tonotopic organization of the avian basilar papilla and mammalian cochlea. *Proceedings of the National Academy of Sciences,* 112**,** 3746-3751.

Son, E. J., J.-H. Ma, H. Ankamreddy, J.-O. Shin, J. Y. Choi, D. K. Wu & J. Bok (2015b) Conserved role of Sonic Hedgehog in tonotopic organization of the avian basilar papilla and mammalian cochlea. 112**,** 3746-3751.

Son, E. J., J. H. Ma, H. Ankamreddy, J. O. Shin, J. Y. Choi, D. K. Wu & J. Bok (2015c) Conserved role of Sonic Hedgehog in tonotopic organization of the avian basilar papilla and mammalian cochlea. *Proc Natl Acad Sci U S A,* 112**,** 3746-51.

Son, E. J., L. Wu, H. Yoon, S. Kim, J. Y. Choi & J. Bok (2012) Developmental gene expression profiling along the tonotopic axis of the mouse cochlea. *PLoS One,* 7**,** e40735.

Stojanova, Z. P., T. Kwan & N. Segil (2016) Epigenetic regulation of Atoh1 guides hair cell development in the mammalian cochlea. *Development,* 143**,** 1632.

Stone, J. S. & E. W. Rubel (2000) Cellular studies of auditory hair cell regeneration in birds. *Proceedings of the National Academy of Sciences,* 97**,** 11714-11721.

Street, K., D. Risso, R. B. Fletcher, D. Das, J. Ngai, N. Yosef, E. Purdom & S. Dudoit (2018) Slingshot: cell lineage and pseudotime inference for single-cell transcriptomics. *BMC Genomics,* 19**,** 477.

Stuart, T., A. Butler, P. Hoffman, C. Hafemeister, E. Papalexi, W. M. Mauck, Y. Hao, M. Stoeckius, P. Smibert & R. Satija (2019) Comprehensive Integration of Single-Cell Data. *Cell,* 177**,** 1888-1902.e21.

Suzuki, J., H. Inada, C. Han, M. J. Kim, R. Kimura, Y. Takata, Y. Honkura, Y. Owada, T. Kawase, Y. Katori, S. Someya & N. Osumi (2019) "Passenger gene" problem in transgenic C57BL/6 mice used in hearing research. *Neurosci Res*.

Szuts, E. Z. & F. I. Harosi (1991) Solubility of retinoids in water. *Arch Biochem Biophys,* 287**,** 297-304.

Takeda, K., S. Yokoyama, H. Aburatani, T. Masuda, F. Han, M. Yoshizawa, N. Yamaki, H. Yamamoto, N. Eguchi, Y. Urade & S. Shibahara (2006) Lipocalin-type prostaglandin D synthase as a melanocyte marker regulated by MITF. *Biochem Biophys Res Commun,* 339**,** 1098-106.

Talavage, T. M., M. I. Sereno, J. R. Melcher, P. J. Ledden, B. R. Rosen & A. M. Dale (2004) Tonotopic organization in human auditory cortex revealed by progressions of frequency sensitivity. *Journal of neurophysiology,* 91**,** 1282-1296.

Tao, L., H. V. Yu, J. Llamas, T. Trecek, X. Wang, Z. Stojanova, A. K. Groves & N. Segil (2021) Enhancer decommissioning imposes an epigenetic barrier to sensory hair cell regeneration. *Dev Cell,* 56**,** 2471-2485.e5.

Tateya, T., I. Imayoshi, I. Tateya, K. Hamaguchi, H. Torii, J. Ito & R. Kageyama (2013) Hedgehog signaling regulates prosensory cell properties during the basal-to-apical wave of hair cell differentiation in the mammalian cochlea. *Development,* 140**,** 3848-57.

Thiede, B. R., Z. F. Mann, W. Chang, Y. C. Ku, Y. K. Son, M. Lovett, M. W. Kelley & J. T. Corwin (2014) Retinoic acid signalling regulates the development of tonotopically patterned hair cells in the chicken cochlea. *Nat Commun,* 5**,** 3840.

Trapnell, C., D. Cacchiarelli, J. Grimsby, P. Pokharel, S. Li, M. Morse, N. J. Lennon, K. J. Livak, T. S. Mikkelsen & J. L. Rinn (2014) The dynamics and regulators of cell fate decisions are revealed by pseudotemporal ordering of single cells. *Nat Biotechnol,* 32**,** 381-386.

Trowe, M. O., H. Maier, M. Schweizer & A. Kispert (2008) Deafness in mice lacking the T-box transcription factor Tbx18 in otic fibrocytes. *Development,* 135**,** 1725-34.

Tufcea, D. E. & P. François (2015) Critical Timing without a Timer for Embryonic Development. *Biophys J,* 109**,** 1724-34.

Uehara, S., Y. Izumi, Y. Kubo, C. C. Wang, K. Mineta, K. Ikeo, T. Gojobori, M. Tachibana, T. Kikuchi, T. Kobayashi, S. Shibahara, C. Taya, H. Yonekawa, T. Shiroishi & H. Yamamoto (2009) Specific expression of Gsta4 in mouse cochlear melanocytes: a novel role for hearing and melanocyte differentiation. *Pigment Cell Melanoma Res,* 22**,** 111-9.

Umesono, K., K. K. Murakami, C. C. Thompson & R. M. Evans (1991) Direct repeats as selective response elements for the thyroid hormone, retinoic acid, and vitamin D3 receptors. *Cell,* 65**,** 1255-66.

van Dijk, D., R. Sharma, J. Nainys, K. Yim, P. Kathail, A. J. Carr, C. Burdziak, K. R. Moon, C. L. Chaffer, D. Pattabiraman, B. Bierie, L. Mazutis, G. Wolf, S. Krishnaswamy & D. Pe'er (2018) Recovering Gene Interactions from Single-Cell Data Using Data Diffusion. *Cell,* 174**,** 716-729.e27.

van Schaarenburg, R. A., J. Suurmond, K. L. Habets, M. C. Brouwer, D. Wouters, F. A. Kurreeman, T. W. Huizinga, R. E. Toes & L. A. Trouw (2016) The production and secretion of complement component C1q by human mast cells. *Mol Immunol,* 78**,** 164-170.

Vendrell, V., I. López-Hernández, M. B. Durán Alonso, A. Feijoo-Redondo, G. Abello, H. Gálvez, F. Giráldez, T. Lamonerie & T. Schimmang (2015) Otx2 is a target of N-myc and acts as a suppressor of sensory development in the mammalian cochlea. *Development,* 142**,** 2792-800.

Visel, A., C. Thaller & G. Eichele (2004) GenePaint.org: an atlas of gene expression patterns in the mouse embryo. *Nucleic Acids Res,* 32**,** D552-6.

Wagner, D. E., C. Weinreb, Z. M. Collins, J. A. Briggs, S. G. Megason & A. M. Klein (2018) Single-cell mapping of gene expression landscapes and lineage in the zebrafish embryo. *Science,* 360**,** 981-987.

Waldhaus, J., R. Durruthy-Durruthy & S. Heller (2015) Quantitative High-Resolution Cellular Map of the Organ of Corti. *Cell Rep,* 11**,** 1385-99.

Wallis, D., M. Hamblen, Y. Zhou, K. J. Venken, A. Schumacher, H. L. Grimes, H. Y. Zoghbi, S. H. Orkin & H. J. Bellen (2003) The zinc finger transcription factor Gfi1, implicated in lymphomagenesis, is required for inner ear hair cell differentiation and survival. *Development,* 130**,** 221-32.

Wang, J., B. Zhang, H. Jiang, L. Zhang, D. Liu, X. Xiao, H. Ma, X. Luo, D. Bojrab & Z. Hu (2013) Myelination of the postnatal mouse cochlear nerve at the peripheral-central nervous system transitional zone. *Front Pediatr,* 1**,** 43.

Wang, S., M. P. Lee, S. Jones, J. Liu & J. Waldhaus (2021) Mapping the regulatory landscape of auditory hair cells from single-cell multi-omics data. *Genome Res*.

Wang, S. C., S. Fu , Y. , Lee , MP. Liu , J. Waldhaus , J. 2022. Spatial transcriptomic reconstruction of the mouse cochlea suggests morphogen-based principles of tonotopic specification. [**Preprint**]: Posted: 7 Oct 2022. Available at SSRN: abstract=4240416. DOI: 10.2139/ssrn.4240416.

Weiss, T., S. Taschner-Mandl, A. Bileck, A. Slany, F. Kromp, F. Rifatbegovic, C. Frech, R. Windhager, H. Kitzinger, C. H. Tzou, P. F. Ambros, C. Gerner & I. M. Ambros (2016) Proteomics and transcriptomics of peripheral nerve tissue and cells unravel new aspects of the human Schwann cell repair phenotype. *Glia,* 64**,** 2133-2153.

Welch, J. D., V. Kozareva, A. Ferreira, C. Vanderburg, C. Martin & E. Z. Macosko (2019) Single-Cell Multi-omic Integration Compares and Contrasts Features of Brain Cell Identity. *Cell,* 177**,** 1873-1887.e17.

Weston, A. D., B. Blumberg & T. M. Underhill (2003) Active repression by unliganded retinoid receptors in development: less is sometimes more. *J Cell Biol,* 161**,** 223-8.

White, R. J., Q. Nie, A. D. Lander & T. F. Schilling (2007) Complex regulation of cyp26a1 creates a robust retinoic acid gradient in the zebrafish embryo. *PLoS Biol,* 5**,** e304.

Wilkerson, B. A., A. D. Chitsazan, L. S. VandenBosch, M. S. Wilken, T. A. Reh & O. Bermingham-McDonogh (2019a) Open chromatin dynamics in prosensory cells of the embryonic mouse cochlea. *Sci Rep,* 9**,** 9060.

Wilkerson, B. A., A. D. Chitsazan, L. S. VandenBosch, M. S. Wilken, T. A. Reh & O. J. S. r. Bermingham-McDonogh (2019b) Open chromatin dynamics in prosensory cells of the embryonic mouse cochlea. 9**,** 9060.

Wilkerson, B. A., H. L. Zebroski, C. R. Finkbeiner, A. D. Chitsazan, K. E. Beach, N. Sen, R. C. Zhang & O. Bermingham-McDonogh (2021) Novel cell types and developmental lineages revealed by single-cell RNA-seq analysis of the mouse crista ampullaris. *Elife,* 10.

William, S. C. Robust Locally Weighted Regression and Smoothing Scatterplots. *Journal of the American Statistical Association,* 74**,** 829-836 , year = 1979.

Wiwatpanit, T., S. M. Lorenzen, J. A. Cantú, C. Z. Foo, A. K. Hogan, F. Márquez, J. C. Clancy, M. J. Schipma, M. A. Cheatham, A. Duggan & J. García-Añoveros (2018) Trans-differentiation of outer hair cells into inner hair cells in the absence of INSM1. *Nature,* 563**,** 691-695.

Wobus, A. M. & K. R. Boheler (2005) Embryonic stem cells: prospects for developmental biology and cell therapy. *Physiological reviews,* 85**,** 635-678.

Woods, C., M. Montcouquiol & M. W. Kelley (2004) Math1 regulates development of the sensory epithelium in the mammalian cochlea. *Nat Neurosci,* 7**,** 1310-8.

World Health Organization. 2021. World report on hearing. World Health Organization.

Wu, D. K. & M. W. Kelley (2012) Molecular mechanisms of inner ear development. *Cold Spring Harb Perspect Biol,* 4**,** a008409.

Wu, X., M. V. Ivanchenko, H. Al Jandal, M. Cicconet, A. A. Indzhykulian & D. P. Corey (2019) PKHD1L1 is a coat protein of hair-cell stereocilia and is required for normal hearing. *Nat Commun,* 10**,** 3801.

Xiang, M., L. Gan, D. Li, Z. Y. Chen, L. Zhou, B. W. O'Malley, W. Klein & J. Nathans (1997) Essential role of POU-domain factor Brn-3c in auditory and vestibular hair cell development. *Proc Natl Acad Sci U S A,* 94**,** 9445-50.

Xu, J., H. Ueno, C. Y. Xu, B. Chen, I. L. Weissman & P. X. Xu (2017) Identification of mouse cochlear progenitors that develop hair and supporting cells in the organ of Corti. *Nat Commun,* 8**,** 15046.

Yang, L. M., K. S. E. Cheah, S. H. Huh & D. M. Ornitz (2019) Sox2 and FGF20 interact to regulate organ of Corti hair cell and supporting cell development in a spatially-graded manner. *PLoS Genet,* 15**,** e1008254.

Yang, S., Q. Cai, J. Bard, J. Jamison, J. Wang, W. Yang & B. H. Hu (2015) Variation analysis of transcriptome changes reveals cochlear genes and their associated functions in cochlear susceptibility to acoustic overstimulation. *Hear Res,* 330**,** 78-89.

Yorgason, J. G., J. N. Fayad & F. Kalinec (2006) Understanding drug ototoxicity: molecular insights for prevention and clinical management. *Expert opinion on drug safety,* 5**,** 383-399.

Young, K. M., T. Mitsumori, N. Pringle, M. Grist, N. Kessaris & W. D. Richardson (2010) An Fgfr3-iCreER(T2) transgenic mouse line for studies of neural stem cells and astrocytes. *Glia,* 58**,** 943-53.

Zhang, Y., D. Chen, L. Zhao, W. Li, Y. Ni, Y. Chen & H. Li (2019) Nfatc4 Deficiency Attenuates Ototoxicity by Suppressing Tnf-Mediated Hair Cell Apoptosis in the Mouse Cochlea. *Front Immunol,* 10**,** 1660.

Zhang, Y., Z. Zhang, P. Chen, C. Y. Ma, C. Li, T. Y. K. Au, V. Tam, Y. Peng, R. Wu, K. M. C. Cheung, P. C. Sham, H. F. Tse, D. Chan, V. Y. Leung, K. S. E. Cheah & Q. Lian (2020) Directed Differentiation of Notochord-like and Nucleus Pulposus-like Cells Using Human Pluripotent Stem Cells. *Cell Rep,* 30**,** 2791-2806.e5.

Zhou, Y., J. Williams, P. M. Smallwood & J. Nathans (2015) Sox7, Sox17, and Sox18 Cooperatively Regulate Vascular Development in the Mouse Retina. *PLoS One,* 10**,** e0143650.